SAPIENZA
UNIVERSITÀ DI ROMA

Light controlled motility of *Escherichia coli*

characterization and applications

Scuola di dottorato Vito Volterra

Dottorato di Ricerca in Fisica – XXX Ciclo

Candidate

Giacomo Frangipane
ID number 1264196

Thesis Advisor

Prof. Roberto Di Leonardo

A thesis submitted in partial fulfillment of the requirements
for the degree of Doctor of Philosophy in Physics

31 October 2017

Thesis not yet defended

Light controlled motility of *Escherichia coli* characterization and applications
Ph.D. thesis. Sapienza – University of Rome

This thesis has been typeset by LaTeX and the Sapthesis class.

Version: December 20, 2017

Author's email: giacomo.frangipane@gmail.com

to Prof. Anna Tramontano

Introduction

Physicists have been placing an increasing effort to study living systems. The most natural way for a physicist to approach the complexity of these systems is to start from unicellular organisms such as bacteria. Bacteria are among the simplest form of life on Earth. Nonetheless these microorganisms contain all the molecular machinery to grow, sense the environment and convert energy into movement.

Since the molecular biology revolution in 1950, *E. coli* has been the bacterial model organism to work with, thanks to its versatility and ease of handling [1]. Indeed it grows easily and quickly, reproducing by binary fission with a doubling time shorter than one hour, and the *E. coli* derived by the K-12 strain have a biosafety level 1, which makes them manageable in all the laboratories. Quoting the words of Adam Arkin - a pioneer in Synthetic Biology, at the University of California, Berkeley - about *E. coli*: "Over the course of a hundred years of intense study, we have a huge amount of information about the organism, more than any other on Earth"[1]. Therefore, not surprisingly, it became the tool of choice in synthetic biology, an emerging field combining engineering principles and techniques of biotechnology to design and construct biological systems for useful purposes [2]. Living cells are like DNA software-driven biological machines, that can be hacked and reprogrammed implementing new features and functions (J.C. Venter 2012). The insertion of rationally designed, complex synthetic gene circuits [3], and the creation of entirely synthetic genomes [4] have been already demonstrated.

Furthermore, from the physics point of view, *E. coli* is a marvelous example of a self-propelled micro-machine. Bacteria, together with synthetic self-propelled colloids [5], represent the constituent units of most of active matter systems and are classified as 'active colloids'[6]. These particles have sizes ranging from 5 nm to 5 µm and they can move against viscous forces of the surrounding low-Reynolds number environment by continuosly consuming 'fuel' [7]. This constant flow of energy sets them in a framework of non-equilibrium physics [8] where many unusual phenomena, not attainable by passive matter, may appear, such as rectification [9, 10], reduced viscosity [11] and collective behaviors [12]. Self-organization, typical behavior in

[1] https://www.wired.com/2016/06/new-model-organism-double-pace-biology/

bacterial colonies and flocks of birds, can rise-up in colloidal active systems, providing the route to new forms of micromachines [13] and new active materials reconfigurable at the microscale using external fields [14, 15].

In the last 30 years, we witnessed an enormous development of light technologies for spatio-temporal shaping of light at microscale [16, 17]. Light intensity patterns can now be almost arbitrarily designed with spatial resolution of micrometers and temporal resolution of microseconds. Combination of the synthetic biology toolkit and these light technologies, paves the way to a light controllable *E. coli* as active matter with reconfigurable and interactively tunable properties.

This PhD Thesis is divided into two parts. In Part I, after a general introduction to *E. coli* motility and propulsion mechanism (Chapter 1), we present the results we obtained combining tools from synthetic biology, advanced optical techniques for light shaping and 3D lithography along with digital video microscopy. Furthermore we present the research path we followed to create a novel light controllable mutant *E. coli*, using the expression of a heterologous photoreceptor (Chapter 2). We exploited these genetically engineered strains as units in bacterial samples whose density can be arbitrarily shaped with light (Chapter 3) and as propellers for light controlled 3D micromotors (Chapter 4).

In Part II we discuss the details of the main methods used in this PhD project. Some of these methods have been also crucial for projects which are not strictly related to the subject of the present Thesis (Section 5.4) and to which I have contributed during the last three years: (i) *E. coli* swimming in 1D confinement 5.4.2 (ii) Experimental evidence of a general property of random walks 5.4.3

Contents

Part I

Light controlled motility in *Escherichia coli*

Chapter 1

Escherichia coli motility

Escherichia coli, the microswimmer model used in this Thesis, is a rod-shaped bacterium commonly living immersed in a fluid. It has a length $\sim$ 2.5 µm, a diameter of 0.8 µm and a mass of 1-2 pg (Fig. 1.1). At this microscale, the locomotion strategies of the macroscopic world are ineffective. The world of microswimmers is the world of 'low Reynolds number', a world dominated by viscous forces where inertia plays little role [18]. The Reynolds number Re is an adimensional quantity representing the ratio between inertial and viscous forces in a fluid. It is defined as: $Re = \rho LU/\eta$, where ρ is the fluid density, η is the viscosity of the fluid, L and U the characteristic length and velocity scales in the fluid dynamics, respectively. In water $\rho \sim 10^3$ Kg/m^3 and $\eta \sim 10^{-3}$ Pa$\cdot$s, a bacterium moves with speed $\sim$ 10 µm/s thus $Re \sim 10^{-4} - 10^{-5}$, while a small fish lives at $Re \sim 10^2$ and a swimming man at $Re \sim 10^4 - 10^5$. In the microscopic world of *E. coli*, such small Re allows to neglect the inertia terms in the Navier-Stokes equations that simplifies to the Stokes equations [19]:

$$\begin{cases} -\nabla p + \eta \nabla^2 \mathbf{u} = 0 \\ \nabla \cdot \mathbf{u} = 0 \end{cases}$$

where in an incompressible viscous fluid $\mathbf{u}$ is the velocity field of the fluid and p the pressure. The linearity and time-independence of this equation lead to two important properties of low Reynolds number locomotion [18]. The first is **rate independence**: the distance travelled by a swimmer undergoing a surface deformation does not depend on the configuration change rate. The second property is the **scallop theorem**: the net displacement of a swimmer, deformining its shape in a sequence that appear identical if looked back in time, is zero. This theorem cuts out 'reciprocal deformation' as possible locomotion mechanisms. However, microorganisms evolved to find different locomotion solutions to overcome these physical constraints, such as the flagellar corkscrew-like motion developed in *E. coli* [20].

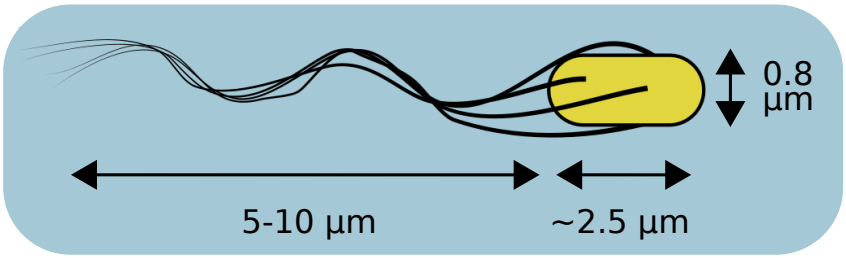

Figure 1.1. *Escherichia coli* size and shape. The cell body is approximately a spherocylinder of length ~ 2.5 µm and diameter of ~ 0.8 µm. The bacterium propel himself rotating a bundle of flagella, elongated filaments of variable length 5-10 µm attached to the body.

Indeed *E. coli* can propel itself at the speed of ~ 10 bodylengths/s by rotating a bundle of multiple flagella [21]. Flagella are polymers of single proteins flagellin (FliC), forming helical filaments of variable length, tipically 5 to 10 µm, but with a constant diameter ~ 20 nm [22]. Each of these filaments is connected through the hook to the rotor, the rotating component of the motor inserted in a protein complex forming the stator. The flagellar motor is embedded in the cell envelope, composed by a cell wall inserted between two plasma membranes, the cytoplasmic membrane and the outer membrane (Fig. 1.2). While the inner membrane is slightly permeable to protons, porins (ion channels) inserted the outer membrane make the membrane permeable to protons, setting the periplasm pH to that of the external environment [23]. Thus, as protons translocate to the periplasmic space, an electric potential develops across the inner membrane that acts as the dielectric in a condenser. This electrochemical potential, known as proton motive force (PMF), guides a flow of protons across the membrane powering the flagellar motor. The PMF is the combination of the transmembrane voltage potential $\Delta\psi$, generated by the different concentration of ions species across the membrane, and the contribution of the H^+ concentration gradient:

$$\mathrm{PMF} = \Delta p = \Delta\psi + \ln 10 \frac{k_B T}{e} \Delta\mathrm{pH}$$

where ΔpH denotes the difference of pH across the membrane, k_B is Boltzmann costant, T the absolute temperature and e the elementary charge. Adenosin triphosphate (ATP), the "molecular currency" of intracellular energy transfer [24], does not play any direct role in powering the flagellar motor, differently from other molecular motors. However protons are accumulated against the electrochemical forces by the electron transport chain (the bacterial "respiration") and by other metabolic

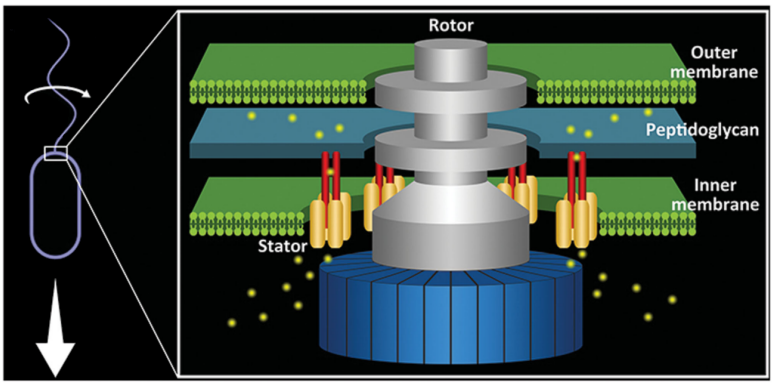

Figure 1.2. Bacterial flagellar motor. This nanoscale motor is embedded in the cell envelope and powered by flux of proton crossing the inner membrane, rapidly rotate the flagellum ($\sim$ 100 Hz). Modified from [25]

processes involving ATPase, which are enzymes able to release the energy conserved in the ATP phosphate bonds.

Thus, thanks to the motor, flagella spin clockwise (CW) or counterclockwise (CCW), and the direction of rotation influences the swimming behavior of the cell, defining the characteristic run-and-tumble dynamics. When all flagella spin CCW (looking along a filament from its end toward the motor), they work in unison to propel the cell forming the flagellar bundle. In this "run" state, a cell swims steadily along the direction of its long axis. When one of the motor starts to spin CW the bundle disassembles and the independent motion of flagella induces an erratic dynamics and the reorientation of the cell, that is said to "tumble". In homogeneous chemical environments, the transition times between these two swimming behaviors are well described by an exponential distribution with characteristic times of $\tau_{\text{run}} \sim 1$ s for runs and $\tau_{\text{tumble}} \sim 0.1$ s for tumbles [26].

This swimming pattern is coupled to an internal regulatory system that estimates chemical gradients in the local environment (input) and modulates the probability of the following tumbling event (output), resulting in a net movement towards favorite environments. The small size of *E. coli* bacterium hinders the possibility to sense chemical gradients using spatial measurements. Nonetheless, it developed a mechanism to make temporal comparisons of chemical concentrations [27]. *E. coli* takes its time to understand if the chosen direction is advantageous [28] and different ways of connecting the input and the output lead to a wide range of chemotactic behaviors including climbing gradients of nutrients (Fig. 1.3) or ending up in stationary distributions that maximize the overlap between bacteria and chemoattractants [29, 30]. The chemotactic signal trasduction network relies on the Che proteins and interacts with the motor via the response regulator protein CheY [31]. This protein is phospho-

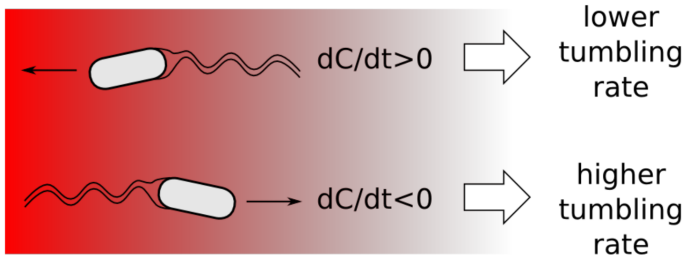

Figure 1.3. Chemotaxis. *E. coli* makes temporal comparisons of chemical concentration. A bacterium that swims up-gradient sense an increasing concentration of nutrients C, the chemotaxis machinery lowers its tumble rate thus increasing directional persistence in the motion. On the other hand when it moves away from nutrients its tumble rate is increased.

rylated (one phosphate group is added) by the kinase CheA and dephosphorylated by the phosphatase CheZ. The phosphorylated form of CheY (CheY-P) binds to the flagellar motor inducing a tumbling response. CheA is controlled by five chemoreceptors (*i.e.* Tar, Tsr, Trg, Tap and Aer) reacting to different external input. Kinase activity is reduced when attractants are added inducing a decrease in the tumbling rate (for repellents results the opposite behavior) [32]. The deletion of CheY permits the creation of a mutant strain in which tumbles are suppressed. These bacteria are commonly named smooth-swimmers (*e.g.* HCB437 [32]). Recent experiments have shown that an unknown cellular pathway regulates *E. coli* swimming speed, improving the efficiency of chemotaxis, in presence of attractants [33, 34] as well as of repellents [35]. This changes in swimming speed can be attributed to chemotactic receptors that directly control the 'fuel' available for the motor by regulating the intracellular pH of the cell [36].

Since this bacterium is the most studied organism on Earth, many mutations have been tested on it. The Coli Genetic Stock Center (CGSC) houses an entire database of *E. coli* mutant strains and, since 1971, has provided lab strains to the *E. coli* community. The database contains thousands of strain included a set of *E. coli* with single-gene knockout of all non-essential genes (the Keio collection [37]). Among all these mutants, many *E. coli* with modified motility characteristics are present. Moreover the possibility to implement new genes from heterologous host in its the genome expands the possibility to control its swimming behavior for statistical and practical purposes.

Chapter 2

Light controlled motility

In the previous Chapter we talked about chemotaxis as a mechanism developed by bacteria through which they can sense and move along chemical gradients by modulating their tumbling rate (for instance, nutrients or repellents, like glucose or an antibiotic, respectively). Although temporal pulses or steps of chemical stimuli can be delivered with sufficient precision, the spatial structure of the attractant/repellent concentration is hard to control. On the other hand, light patterns can be shaped in time and space with a high degree of control by using spatial light modulators (SLM). The use of light to control microswimmers is a field in rapid growth [38, 15, 39] and is appealing for applications [40, 41, 42].

Light is a source of energy and information for bacteria. Phototrophic bacteria, like all other organisms, need to find the best environmental conditions to grow and replicate. In the course of evolution they have developed many different photosensory proteins to respond to the main stimulus that characterizes their environment: light. These proteins were for a long time considered to be present only in phototrophic bacteria, but light-regulated responses have been demonstrated to be ubiquitous also in chemotrophic bacteria [43]. Photoreceptors are signal-transduction proteins characterized by a region responsible for light absorption, known as chromophore. Light in the visible spectrum can excite the photoreceptor, inducing its conformational change and activating a cascade of downstream events resulting in the signal transduction. Most of these photoreceptors can be classified in six families: rhodopsins, phytochromes, xanthopsins, cryptochromes, phototropins, and BLUF proteins. Each of these families is characterized by a different chromophore or a different photochemistry [44] (Table 2.1).

Evolutionary pressure has generated a huge variety of mechanisms to react to changes of ambient light characteristics (*i.e.* , intensity, color, direction, and degree of polarization) [45]. Since the DNA sequencing was developed, biologists have placed much effort to discover the relevant genes underlying these mechanisms. So

CHROMOPHORES			PHOTOSENSOR FAMILY	PHOTOCHEMISTRY
classes	example	key structural element		
tetrapyrroles	phytochromobilin	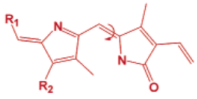	Phytochromes	*trans* ↔ *cis*
polyenes	retinal	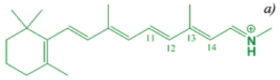	Rhodopsins	*trans* ↔ *cis*
	coumaric acid	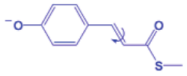	Xanthopsins	*trans* ↔ *cis*
'aromatics'		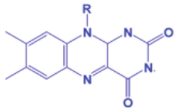	Cryptochromes	electron transfer?
	flavin		Phototropin	cysteinyl adduct formation
			BLUF proteins	proton transfer?

Table 2.1. Classification of known photoreceptor families. Photoreceptors families are classified on the basis of their chromophore, defining the light absorption spectrum, and of the chemistry underlying its photocycle. From [44].

far we know many molecular and functional characteristics of these receptors that allow microorganisms to exploit ambient light to control internal processes, such as the reorientation of their motion or protein production [45]. The response to light is not a prominent feature of wild-type *E. coli*. Nonetheless, *E. coli* expresses the photoreceptor protein YcgF, a BLUF type photoreceptor that, binding to flavin, activates a response mechanism to blue-light.

In recent years, synthetic biology has emerged as a cutting-edge field at the intersection of biology and engineering. Synthetic biology aims at designing and building novel biomolecular components, networks and pathways which are reliable, optimized and interchangeable[1]. The development of new technologies in DNA synthesis and editing offers the possibility to "program" bacteria, introducing synthetic genetic circuits, likewise new "softwares", thus implementing novel bacterial features and functions. Using these modern tools, it is possible to extend the light response of *E. coli* by introducing genes coding for photoreceptors that natively belong to other organisms. Such genetically engineered *E. coli* has the ability to "see light" [46]. Furthermore the possibility of expressing in the same bacterium three photoreceptors whose excitation spectra just minimally overlap has been recently demonstrated. This lead to three different responses depending on the wavelength of the light perceived by the bacterium [47]. In this Chapter we discuss the application of the

[1] http://parts.igem.org

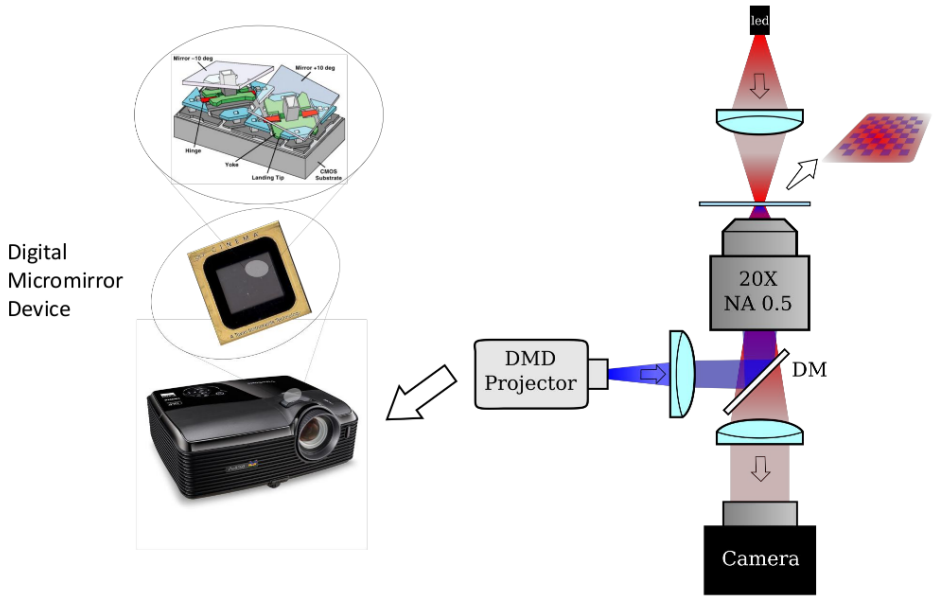

Figure 2.1. Experimental set-up. Combinination of bright/dark field microscopy and a digital light projector (DLP). The DLP has is core in a digital micromirror device, a chip covered of several thousand of microscopic mirrors corresponding to pixels in the image to be displayed. The DLP has the share the same focal plane of the camera such that we can project arbitrary pattern on the observed region. The sample is confined between two glass slide.

key idea of synthetic biology to set up new methodologies to manipulate a strain of *E. coli* thus to obtain light-contrallable motility. Herein we report the description of the different approaches we used to obtain and characterize the different response to light of both phototactic and photokinetic engineered *E. coli* strains.

Figure 2.1 shows the set-up we used to characterize the response of these strains. Bright field and dark field illumination have been used to collect digital video on a custom-built inverted optical microscope equipped with a 20x (NA 0.50), 10x (NA 0.30) or 4X(NA 0.13) objective. The light reflected off the chip of a Digital Light Processor (DLP- Texas Instruments DLP Lightcrafter 4500) has been focused on the same focal plane of the camera to excite bacterial photoreceptors. The DLP has its core in a digital micromirror device (DMD), a chip covered of several hundreds of thousands of microscopic mirrors corresponding to pixels in the image to be displayed that can be flipped at high frequency to control light intensity. We wrote a C-library using the application programming interface (API) released by the producer of the DLP to control it through a Python shell. We exploit this library to switch between light patterns arbitrarily shaped in time and space. Moreover we could control the wavelength turning on the desired one of the three led present in the DLP and/or applying bandpass filters.

2.1 Phototaxis - light modulates tumble rate

Wild type (WT) *E. coli* has only a single photoreceptor protein that causes a modest response to blue light that, in turn, induces a tumbling event [48]. This effect may be due to exopolysaccharide synthesis [49] producing an instability in the flagellar bundle. In 1995 it was observed that *E. coli* strain with mutations in heme biosynthesis pathway (AW804) exhibits an enhanced photo-repulsive response [50]. The oxygen has to be present to obtain this effect. This was explained by the blue light-mediated sensitization of porphyrin which stimulates the generation of an oxygen species producing a signal for the tumbling response [50, 51]. Moreover the fact that blue light has a reduced effect on *E. coli* mutants lacking the Tsr and/or Tar chemotactic receptors directly relates this effect to the chemotaxis-related function [52]. Since this strain is present in the CGSC we decided to characterize it and explore the possibility to use it to study the connection between the single cell response to external stimuli and the spatial stationary distribution of a population of bacteria.

The preliminary experiments were promising. By creating a blue light spot on the samples we could see an accumulation of bacteria inside the spot, after few minutes of light exposure. However, results were opposite to our expectation, since usually chemotaxis induces bacteria to deplete higher tumble rate regions [26]. Studying the literature on chemotaxis we found a possible explanation for these unexpected experimental results. Tactic behaviors are related to the response of bacteria to an external stimulus. Assuming that the tumble rate $\lambda(t)$ has a linear relation with the concentration of the stimulus $c(t)$ (the intensity in the case of light), we can write:

$$\lambda(t) = \lambda_0[1 - \int_{-\infty}^{t} R(t-t')c(t')dt']$$

where $R(t-t')$ is the response function and λ_0 is the tumble rate value neglecting the environment. From this equation results that, if the shape of $R(t)$ is such that the integral of $\int_{-\infty}^{+\infty} R(t-t')dt' \approx 0$, waiting enough time, the value λ_0 is recovered. The real behavior of bacteria is captured by an $R(t)$ presents a bilobe shape (a positive and a negative lobe) such that bacteria can adapt to the environment. Experiments on mutant strains where the proteins responsible for this adaptation were deleted (ΔCheB, ΔCheR) displayed an inverted chemotactic response with respect to the wild type strain [53, 54]. Theoretical works also demonstrated that accumulation in high attractant (or low repellent) regions occurs since the response function of bacteria presents this characteristic bilobe response function [28, 29, 55].

Our results on AW804 could be explained with a blue-induced phototactic behavior lacking adaptation. Therefore we investigated the effect of a blue light

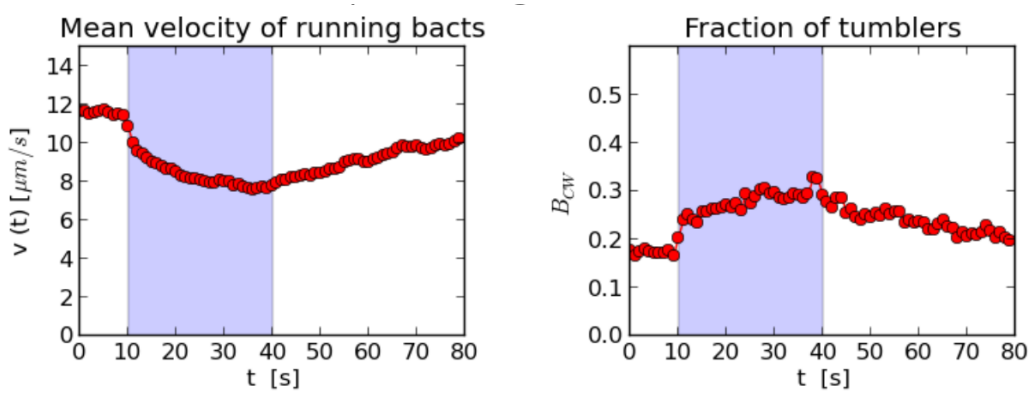

Figure 2.2. Behavioral response of AW804 to blue light. Speed **(left)** and fraction of tumblers **(right)** in response to a step stimulus (at intensity of 2.7 mW/mm^2) was given for a period of 30 s (shaded area). Each point represent the average over 1 s of ≈ 80 bacterial trajectories

step stimulus to measure the response function in this strain. We illuminated homogeneously the samples of AW804 with blue light and recorded through digital-video microscopy their motility behavior. Thanks to the tracking software we developed (described in Section 5.2), we analyzed videos and reconstructed the trajectories revealing tumbling events. To avoid oxygen depletion and to more easily track single bacteria, we worked with low dilution samples (≈ 10^7 cell/mL). The samples were prepared using a glass slide and a cover glass slide glued together with a UV photoresist using as spacer a nylon fishing wire of 70 µm diameter. To reduce impurities, the slides were immersed for at least 24h in a solution of sulfuric acid and a glass-cleaning compound (NOCHROMIX) and then washed with ddH_2O.

Figure 2.2 shows the change in speed during the run phases v(t) and the fraction of tumblers B_{CW} in response to a blue light step stimulus of the duration of 30 s at blue light intensity of 2.7 mW/mm^2. We observed a population average speed decrease of 30% and an 80% increase of the fraction of bacteria in tumbling phase. Our data indicate an extremely slow recovery process from this external perturbation.

Then we studied the role of different light intensities (I) on this effect. We show in Fig. 2.3 the relative jump in v(t) and B_{CW} between the average values before light stimulus and in the last 1 s before the illumination is turned off. As first approximation, data are connected by a linear relation in the range of intensities explored.

We hypothesized that bacteria could not recover completely their motile behavior after light exposure, because of an irreversible photodamage. The restoration we measured is due just in minor part by the recovery of bacteria exposed to light, while the main explanation is that motile bacteria entered the field of view from not illuminated area. Therefore we concluded that if these bacteria are

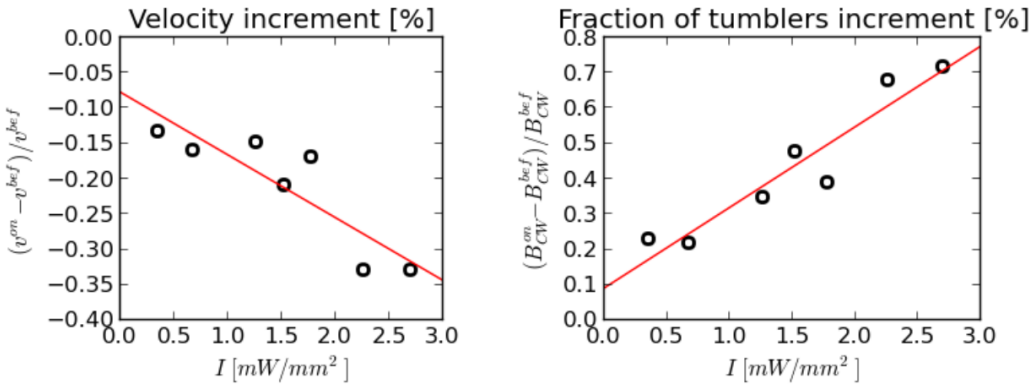

Figure 2.3. Behavioral response of AW804 as a function of light Relative increment of speed **(left)** and fraction of tumblers **(right)** when a sample of AW804 is exposed to a blue light step stimulus, respect to their values before that light is turned on. Data are reported as function of the light intensities. The light is kept on for 30 s and the last second in the blue response is used to evaluate the relative increment.

illuminated for more than few minutes, they become irreversibly non-motile. Using this method we can just temporarily accumulate bacteria in a region, irreversibly damaging their flagellar motors with light. But waiting longer, all the bacteria in the field of view would be non-motile and would behave as passive particles covering homogeneously the entire area. We concluded that this strain is not good for our purpose. Nevertheless, the study of this system was a challenge for me, since it was my first approach to bacterial motility, and we learned much on the light response of bacteria. First conclusion of this experiments is: when you work with *E. coli* avoid blue light!

Then we moved to another possible mechanism of light-control. We successfully trasformed *E. coli* RP437 [56] (WT for chemotaxis studies) with two different plasmids codifying chimeric receptor proteins that link light to the chemotaxis machinery. These proteins are a fusion of the sensory rhodopsin belonging to *N. pharaonis* with the cytoplasmic domain of Tar or Tsr, both methyl-accepting chemotaxis protein receptors (MCP) from enteric eubacteria such as *E. coli* [57]. As previously reported, we expected that the correct folding of these proteins in the membrane should induce a phototactic behavior, reducing the tumbling rate in the Tar-fusion case (NpSRII-NpHtrII-StTar) and increasing it for the Tsr-fusion one (NpSRII-NpHtrII-EcTsr) [57].
From preliminary experiments we established that light could just slightly influence the motility behavior of these strains. The strain expressing the Tar-fusion protein was already smooth-swimming in absence of the light stimulus, while the one expressing Tsr-fusion was tumbling continuously (data not shown). One hypothesis to explain this phenomenon is that this effect is induced by the overproduction of

MCP. It was demonstrated that MCP clustering induce cooperative effects that can enhance the kinase or phosphorylase activity of these proteins [58] [59]. Further experiments with this strain are required to understand the mechanisms occurring in this system. But in parallel to this experiments we were working with the photokinetic *E. coli*, described in details in the next Section.

2.2 Photokinesis - light modulates speed (HCB437 PR$^+$ and HLK)

Photokinesis is the regulation of speed in response to light stimuli, inducing a modification in the energy supply to the flagellar motor [60]. In the past, the only known way bacteria could harvest energy from light was through photosynthetic centers, complex structures executing the first step of photosynthesis. In 2000 the seminal discovery of proteorhodpsin (PR), a light-powered proton pump, changed the way to look at phototrophy in bacteria [61]. This discovery represented an early success story of community metagenomics, the study of genes recovered from environmental samples. It paved the way for further studies demonstrating that this phototrophy alternative mechanism, requiring much fewer genes as compared to the photosynthetic machinery, is extremely common in marine bacteria [62]. The world's oceans contain an estimated 10^{28} PR-expressing bacteria, placing them among the most prevalent organisms on Earth [63]. Furthermore, differently to bacteriorhodopsin, another light-powered proton pump, PR may be correctly folded in *E. coli* membranes [64]. Moreover PR provenient from different bacteria can have various absorption spectrum [65], opening the possibility to tune the excitation wavelengths depending on the need. These characteristics make PR an ideal tool for a wide range of applications in synthetic biology, such as production of chemicals through microbial cell factories powered by light [66].

In 2007 Walter *et al.* [67] were able to use PR expressing (PR+) *E. coli* cells to power its flagellar motor absorbing light. The speed of the flagellar motor is proportional to the PMF [68, 69], therefore, the outer proton flux created by PR, in presence of light, can power the rotation of the flagellum when H^+ re-enter the cell through the motor. However cells can benefit of light-driven proton pumping just under certain environmental conditions [70, 71]. The authors [67] demonstrated that the flagellar motor speed can be controlled with green light (532 nm) in single smooth-swimmer cells PR+, tethered on a glass slide in an environment where the PMF could not be maintained by oxidative phosphorylation.
To clarify the relationships among PMF, respiration and light, they constructed a simplified model of *E. coli* H^+ membrane fluxes. Multiple proton pumps can

contribute to the PMF buildup, such as the respiratory chain, the ATPase and the PR (Fig. 2.4a). This PMF is consumed by the flagellar motor and numerous transporters (*e.g.* Na^+/H^+ antiporter). In addition, the bacterial membrane has a basal permeability to protons [72]. In a simpler system, liposomes with only one kind of ion pump, the magnitude of the steady-state PMF is well approximated by a simple RC circuit [73]. Thus Walter *et al.* proposed the analogous circuit in Figure 2.4b to capture the functional relationship between PMF, respiration and PR inserted in a membrane with sinks. A voltage generator with a variable resistor in series is used to model both the variable PMF yield of respiration and PR. Those two components are posed in parallel with a resistance (R_{sink}) and a capacitor (C) representing proton sinks and the membrane, respectively. In absence of oxygen, respiration does not contribute to PMF, and this is equivalent to send $R_{\text{res}} \to \infty$ cutting out that branch from the circuit. This model set the maximum speed proportional to PMF to just the one generated by the PR:

$$\text{PMF}_{\text{PR}} = \frac{V_{\text{PR}} R_{\text{sink}}}{R_{\text{sink}} + R_{\text{PR}}(I)} \tag{2.1}$$

where the dependence of $R_{\text{PR}}(I)$ from light intensity I is captured by Michaelis-Menten kinetics model:

$$R_{\text{PR}}(I) = \left(\frac{V_{max} I}{K_m + I}\right)^{-1} \tag{2.2}$$

where V_{max} set the maximum value at which the effect of PR is saturated. The dynamics of this system, when the light is reduced is described by:

$$\text{PMF}_{\text{PR}}(I, t) = V_0 \exp\left(-\frac{t}{\tau_{\text{off}}}\right) \tag{2.3}$$

where V_0 is set by the initial condition $t = 0$, PMF_{PR} is defined above (Eq. 2.1) and $\tau_{\text{off}} = R_{\text{eff}} C$. The effective decay resistance R_{eff} is the parallel of $R_{\text{PR}}(I)$ and R_{sink}. The PMF thus decays exponentially to a steady state with a time constant determined by the new level of light I.

In the original work [67] oxidative phosporylation was blocked using azide, a poison inhibiting the cytochrome c oxidase, the last step of the oxydative phosphorylation that transfer electrons from cytochrome c to oxygen. We reasoned that, rather than employing this poison it would be easier to let the cells deplete the oxygen directly from inside the sample, thus removing the last acceptor for the electron transport chain (respiration). This is supported also by data showing that in absence of anaerobically metabolizable nutrients (*e.g.* glucose, serine), when the oxygen ends, the PMF falls abruptly inducing a motility transition in the sample [74]. The inverse of the time necessary to obtain this transition and the concentration of cells

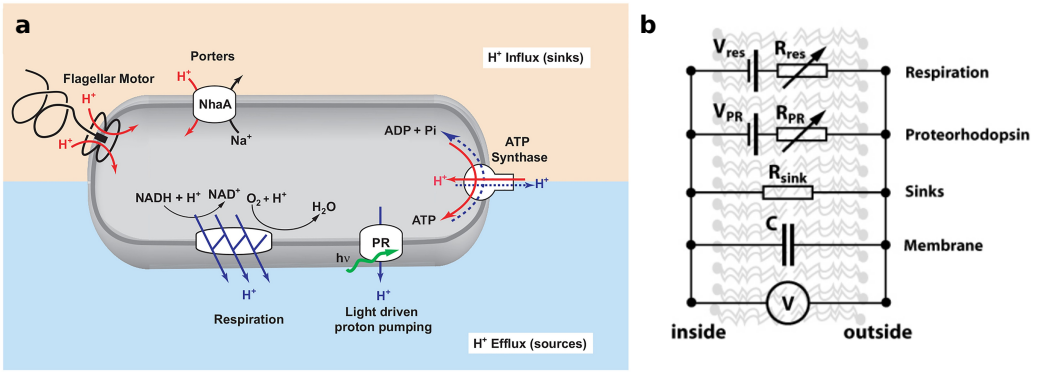

Figure 2.4. Proton fluxes. **(a)** Overview of transmembrane fluxes and proton pumping in *E. coli* with proteorhodopsin (PR). Respiration and PR are responsible of proton gradient buildup, while rotation of the flagellar motor and ATP synthesis can consume this proton motive force. **(b)** Model including sources of PMF (respiration and proteorhodopsin), sinks (such as the flagellar motor and ATP synthase), and the membrane capacitance. The variable resistors R_{res} and R_{PR} model the effect of azide and light on proton extrusion by respiration and PR, respectively. The voltmeter (top-most circuit element) measures the potential difference across the membrane (equivalent to the PMF). Modified from [67].

in the sample are linearly related [7]. Thus we work with high cell density samples ($> 5 \cdot 10^8$ cells/mL), since the higher the cell density, the shorter the time to wait before the experiments can get started. Moreover, at low concentration bacteria would consume their reserves of energy before oxygen is depleted. This leads to a different linear decay of the speed for each bacterium, given the broad metabolic state in the sample. Consequently, the response to light will be broader in the population, since cells would be kept at ~ 0 PMF at different times. It is known that when the flux of protons through the motor stops, the stator proteins MotB dissociate from the motor at an increased rate [75]. Motors disassemble and MotB molecules float around the cell. When the PMF is restored, MotB can be again recruited by the motor and the rotational speed recovers in stepwise increments, resulting in a process called motor 'resurrection' [76]. But if the cells are kept to zero PMF for more than few minutes, the disassembling of the motor becomes not completely reversible and some of the cells cannot recover their motility.

Keeping in mind all these mechanisms, in our laboratory we constructed a system inspired by the one described above. We introduced inside the smooth-swimmer HCB437 [32](RP437 gutted for all the chemotaxis genes) a plasmid codifying the proteorhodopsin by using plasmid transformation described in details in Section 6.2. The plasmid is composed of the backbone pSB1C3 (the standard cloning vector for iGEM parts), and the part BBa_K1604010 codifying the proteorhodopsin under an arabinose inducible promoter. Genes operably linked to this kind of promoters can

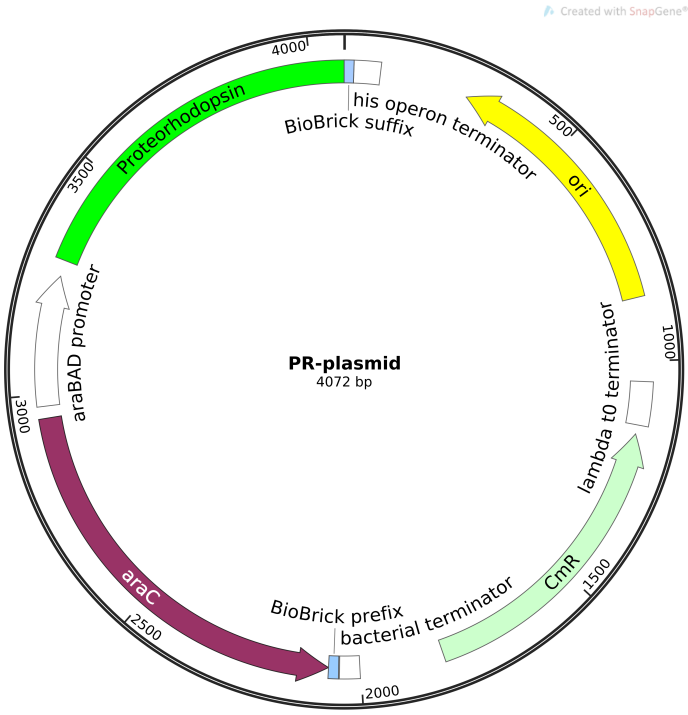

Figure 2.5. Map of the plasmid codifying the proteorhodopsin (PR). The expression system araC-pBAD increase protein production of PR in presence of L-arabinose. The chloramphenicol resistance (CmR) is used as selectable marker

be turned on adding L-arabinose from the external, while in its absence the gene is not expressed. The inducible regulation of gene expression is a key point for the correct operation of our system, since overexpression of the heterologous PR is toxic for the cell.

We then moved to characterize this strain, hereto referred to as HCB437 PR^+. Preliminary experiments show that we were able to visibly see the speed increase induced by light exposure. We then combined the tracking software we developed (Section 5.2) with the "swimming pool" microstructure (Section 5.4.1), a device which let us to select only motile bacteria and to confine them in a pseudo-2D geometry. This allowed to obtain informations on the response dynamics to light of our HCB437 PR^+ strain.

We activated the PR, exposing bacteria to a light square wave with a 20 s period. In these experiments the green light illumination has been achieved using the green led of the DLP, screened using a bandpass filter to obtain the excitation in the desired spectrum region (Thorlabs FBH520-40). We recorded the response using dark-field video microscopy at 50 fps. We analyzed these videos and tracked moving cells inside the "swimming pool" for different light intensities I (Fig. 2.6a). To filter out non-motile bacteria from the analysis, the trajectories that were slower

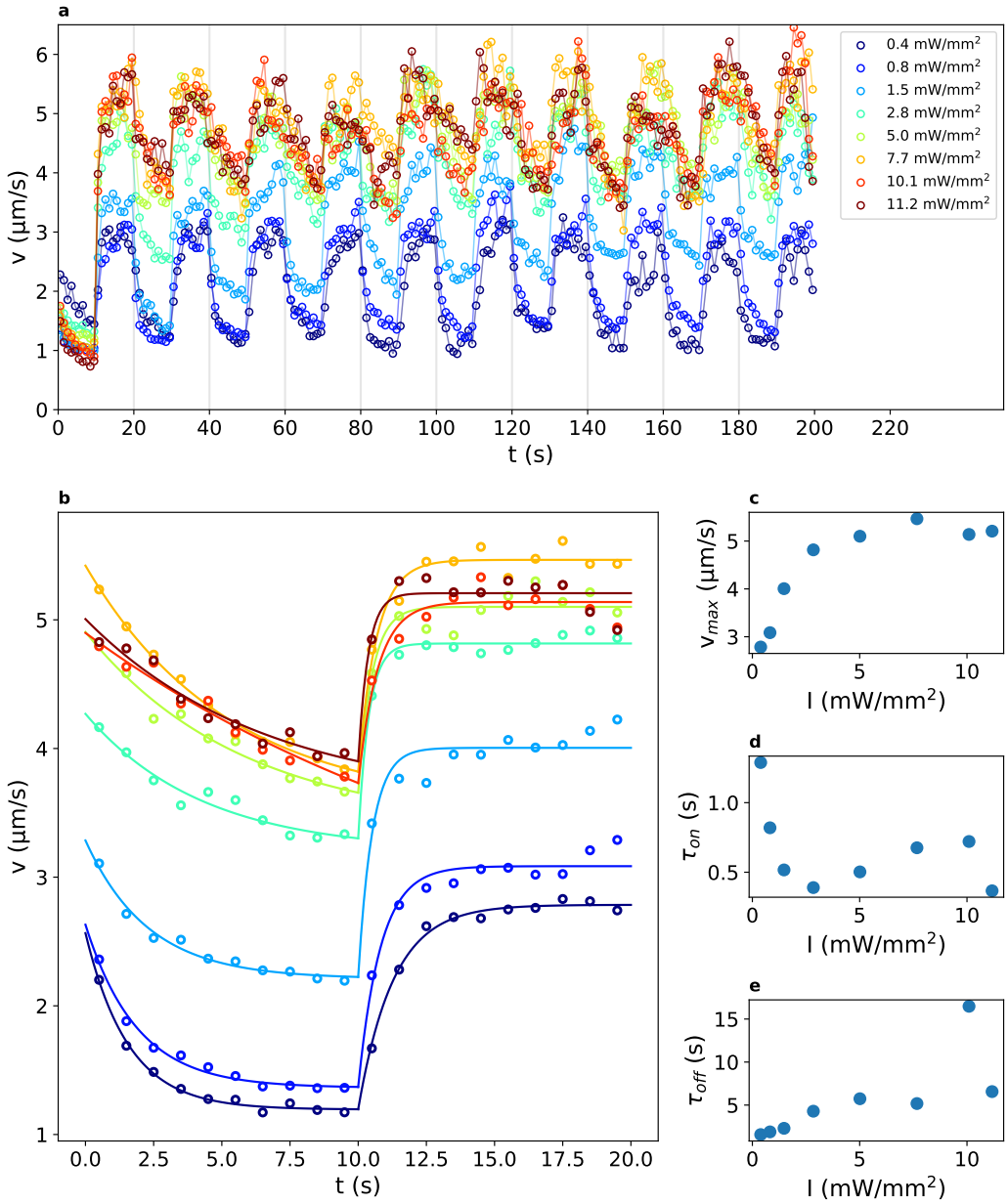

Figure 2.6. HCB437 PR$^+$ temporal response to light. **(a)** Speeds in response to a green light square waves of period 20 s (light is turned on at 10 s), each color represents a different levels of light intensity. The curves are averaged on the bacterial tracks whose speed is higher than 2 µm/s during light exposure. Cells are kept at 0.4 mW/mm^2 for $t < 0$. **(b)** Speeds averaged over 9 periods, the line represent a fit with two exponentials. **(c)** maximum speeds, **(d)** raise and **(e)** decay characteristic times in function of intensity obtained from the fits.

than 2 µm/s during the light were not taken into account. Thus, we considered bacterial tracks that could be reconstructed for at least 2 s during illumination intervals. To avoid the possibility to include the motor "resurrection" dynamics in the measurements, the sample was kept at low light (0.4 mW/mm^2) before measurement started. To quantify maximum speeds, raise and decay times, we compute the average over 9 periods, skipping the first, considering that in this period the cells have different starting states. The maximum speeds we obtained (Fig. 2.6c) show that PR pumping is saturated at high I as previously reported [67]. Furthermore, observing many HCB437 PR$^+$ samples, we realized that the electrical circuit model is not capturing the entire process. When the light is turned off after a prolonged exposure the speed decay present two time scales (data not shown). However the model (Fig. 2.4b) predicts a speed decay with a single characteristic time τ_{off} that does not depend on the intensity level. By contrast, the measured τ_{off} actually increases with the duration of the illumination (data not shown), as well as with the intensity, while τ_{on} decreases (Fig. 2.6d,e). In the circuit model (Fig. 2.4) the ATP-synthase is considered a sink without any difference with the flagellar motors. However, protons that translocate across membranes by proteorhodopsin, generate a PMF that can drive ATP synthesis as protons re-enter the cell through the ATP-synthase complex [77]. The ATP accumulated in the cell can later be used, thanks to ATPase, to fuel cell motility at low speed for prolonged time ($\sim$ minutes). Both these effects are related to the ATPase and increase the response time, hampering the prediction of the light response dynamics.
To avoid this effect and to obtain a faster response swimmer, we explored the possibility to delete the ATPase gene from our strain. In a one-step transformation, we replaced the *unc* operon (encoding ATPase) with the PR gene. The switch between these two genes, both codifying transmembrane proteins, is obtained through the protocol described in Section 6.4.

To statistically characterize the dynamics of the new strain we engineered, hereto referred to as HLK, we use dynamic image correlation spectroscopy (DICS). DICS allows to analyze digital microscopy videos of high concentrated samples and to extract information about the dynamics from the intermediate scattering function (ISF) [78] (Section 5.3). Thanks to this technique we can easily monitor the cells during the oxygen depletion inside the sample and measure the speed during the motility transititon (Fig. 2.7).

We project onto a high concentrated sample ($\approx 5 \times 10^8$ cells/mL) a green light pattern composed of 4×3 squares with side length of 360 µm. Each square has a different level of green light intensity (Fig. 2.8a). Image acquisition is performed after 1 min since pattern projection, to ensure that the stationary speed at that intensity

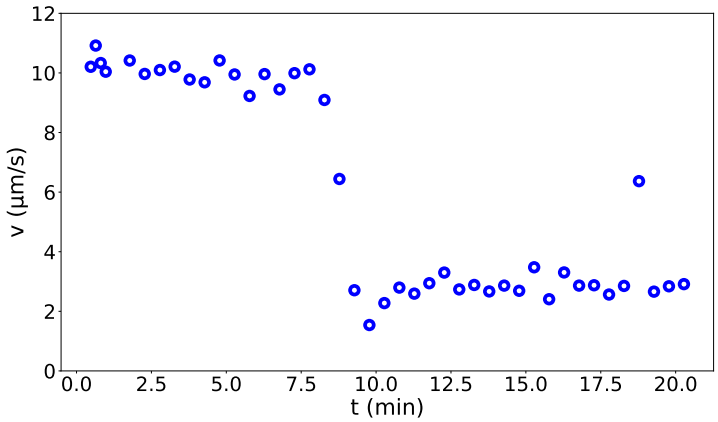

Figure 2.7. Oxygen and the motility transition Average speed of Hulk monitored after the sample is sealed. At high density cells ($\sim 10^9$cells/mL) the oxygen is depleted in a short time and we can observe an abruptly fall in the speed caused by anaerobic condition.

is reached. Analysis is carried out by applying DICS separately to each different region. To avoid out-of-stationarity effects at the border, we crop inside each region another squared region of side length 232 µm, containing information about the dynamics of ≈ 2000 cells. The experiments have been repeated 15 times, between each measurement a homogeneous green pattern (≈ 6 mW/mm^2) is projected to avoid density modulation induced by spatially modulated speed [79]. In Figure 2.8b we show the intermediate scattering function $F_q(t)$ at three different level of light. Increasing the speed of bacteria with light we measure a faster decay in the $F_q(t)$ as we expect. By fitting the $F_q(t)$ obtained from DICS, we extract informations about the fraction of motile bacteria, the average and the standard deviation of their speed distribution, and the thermal diffusion coefficient, respectively α, $\langle v \rangle$, σ, and D in function of the intensity I (Fig. 2.9). The $\langle v \rangle$ in function of I shows the typical hyperbolic behavior described in Eq. 2.1 and Eq. 2.2. We added a baseline to the hyperbola since we could not reach complete zero motility in absence of light. Catabolism let bacteria propel themselves in absence of external nutrient. Fitted data result in a maximum speed jump of 6.13 ± 0.17 µm/s with a baseline of 2.31 ± 0.23 µm/s (Fig. 2.9a). The measured D is compatible with previous work [80](Fig. 2.9b). Furthermore, we observe a slight enhanced diffusion induced by increased activity of the bacterial bath despite the reduced number of motile bacteria in the higher speed regions (Fig. 2.9c) [81, 79]. We also note that the ratio $\frac{\langle v \rangle}{\sigma}$ remains constant at all values of I explored (Fig. 2.9).

To explain this linear relation between $\langle v \rangle$ and σ we introduce a simple model that describes the variability in the response to light in the bacterial population. We represent each bacterium in the population by an analog circuit 2.4b with

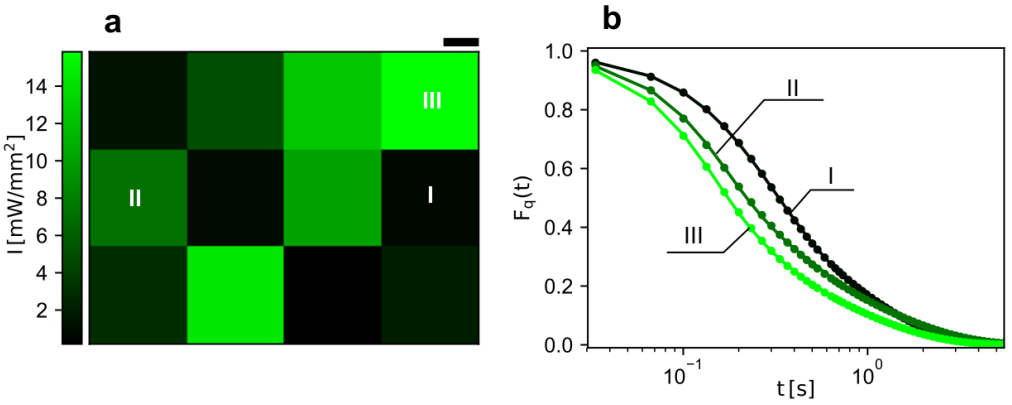

Figure 2.8. **(a)** Pattern projected on the sample to study bacterial response at different light intensities **(b)** Circle represents the recostructed ISFs of an HLK sample at three different light intensities. The line is the ISF fitted using the model described in Section 5.3 information at $q = 1.61\ \mu m^{-1}$. Increasing the light level the ISF decorrelate faster in agreement with the cell speed-up.

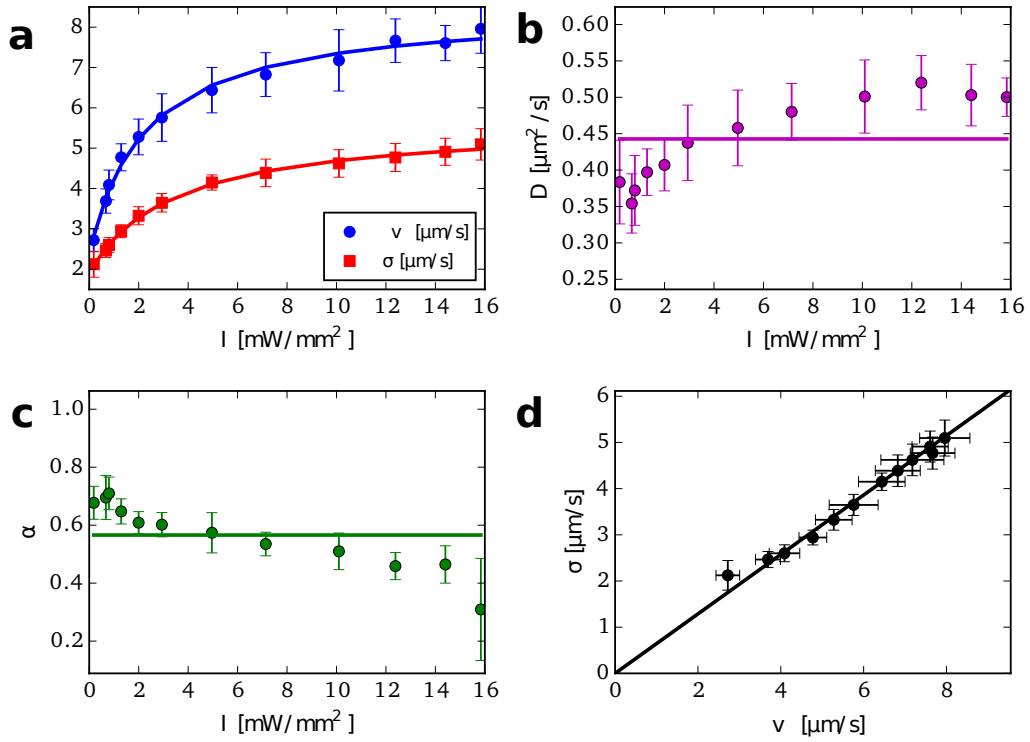

Figure 2.9. Strain characterization in function of light intensity The plots represent bacterial **(a)** speed distribution average of $\langle v \rangle$ and standard deviation σ, **(b)** "passive" diffusion coefficient D and **(c)** fraction of motile α measured with DICS. **(a)** The line represents the hyperbola fitting the power density dependence of the speed. **(d)** We report the relationship between σ and $\langle v \rangle$.

different parameters. We assume: (i) K_m is constant among each PR in the bacterial population since it depends only on the transition rates of the PR photocycle, (ii) the variability in the PMF production induced by light is generated by a different level of PR expression. Then we can define $R_{\mathrm{PR}}(n_{\mathrm{PR}})$ as the equivalent resistance for a bacterium expressing n_{PR} PR. Follows that $R_{\mathrm{PR}}(n_{\mathrm{PR}}) = R_{\mathrm{PR}}(1)/n_{\mathrm{PR}}$, resulted from the parallel of n_{PR} identical PR branches composed by a generator V_{PR} and a a resistance $R_{\mathrm{PR}}(1)$ (corresponding to that of a single PR). Assuming, as measured by [67], that $R_{sink} << R_{\mathrm{PR}}(n_{\mathrm{PR}})$ independently by the light intensities, combining this simple model to describe the variability in proteorhodopsin expression with equations Eq. 2.1 and Eq. 2.2, the speed at the stationary state is:

$$v(I) \propto PMF(I) \propto \frac{f(I)}{R_{\mathrm{PR}}(n_{\mathrm{PR}})} \propto n_{\mathrm{PR}} f(I)$$

where $f(I)$ contains all the dependence of the speed by the light intensity and it is equivalent for each bacterium. This means that each speed in a bacterial population scale with the same factor depending only on the light intensity thus the speed distribution $P(v, I) = P(f(I)v)$. This relation set a constant shape profile of the speed distribution as function of light, thus explaining the linear relation between $\langle v(I) \rangle$ and $\sigma(I)$. This simple explanation does not depend on any assumption describing the variability in the bacterial population given by the system that transduce the PMF in swimming speed (*e.g.* number of flagella, length of the flagella).

When we illuminate a region, the more responsive bacteria exit from the border reaching a dark area that the light emitted by the DLP cannot reach. This effect induce depletion of bacteria from the field of view affecting the measurement. For this reason we decided to measure simultaneously the speeds for twelve different intensities using the pattern shown in Figure 2.8. As raw estimation, we can consider the system as a squared 2d space where the dark area is like a sink and the density inside the light area immediately re-equilibrate to be homogeneous. In this simple model the number of bacteria goes down following $\frac{dN}{dt} = \frac{\rho L^2}{dt} = -\rho v L$. Assuming as ρ_0 the initial density we can write the time dependence of the density as $\rho(t) = \rho_0 e^{-vLt}$. Using the reasonable values of $L \sim 1$ mm, $v \sim 10$ µm/s, we find that the density inside the circle is halved in ≈ 70 s. This estimation does not capture the whole process, since we do not take into account the counterbalance action of diffusion of non-motile bacteria from outside and the time required for cells in the illuminated area to travel to the borders. However, it gives us an idea of the order of magnitude of this temporal decay. Most importantly, we observed that the density modulation in our samples occurs on the minute scale. This effect will be

described in details in Chapter 3. We will also report how the HLK strain let us improve our results thanks to its quicker response compared to HCB437 PR^+ strain.

To obtain the correct expression of PR in HCB437 PR^+ and HLK bacteria the presence of its chromophore, the *all-trans*-retinal, is required. Since these strains do not produce the chromophore autonomously, we supplement the growth medium with 20 µM *all-trans*-retinal when the culture reaches an $OD_{590} \approx 0.2$ (Section 6.1 for details). For applications in self-sustaining sample it would be possible to let the bacteria produce this cofactor by itself, implementing the synthetic pathway "programmed" for this purpose [82, 77]. In the last year two studies revealed the mechanism of two different xenorhodopsins, a new class of microbial rhodopsins, as light activated inward H^+ pump. One is relative to the deep ocean marine bacterium *Parvularcula oceani* (PoXeR), while the other to the nanohalosarchaeon *Nanosalina* (NsXeR) [83]. We believe that this kind of pump could reveal an alternative optogenetic approach substituting the PR in light controlled *E. coli*. We consider that, since these proteins do not require anaerobic environment to work properly, they could improve the speed control and the maximum working speed.

Chapter 3

Light controlled bacterial density

Density modulation with light is a typical behavior of phototactic organisms [84, 85]. Previous experiments show that density modulation of *E. coli* could only be obtained through temperature and chemical gradients [36]. However the control of these gradients is limited by spatial and temporal resolution. By contrast, complex light patterns with details at the single-cell scale ($\sim$ 1 µm) can now be dynamically modified by projecting the DMD chip directly onto the sample. In this Chapter we (i) present a classical model describing the density evolution of run-and-tumble particles whose swimming speed is modulated in space; (ii) demonstrate that light controlled density modulations can be obtained using the HCB437 PR^+ photokinetic strain in 2D confinement; (iii) show that arbitrarily shaped density patterns can be built in the bulk, by the use of the HLK strain, furthermore improving their spatial definition by the implementation of a real-time feedback loop; (iv) discuss how our results can be exploited for novel applications in active matter.

3.1 Theory

In 1993, Schnitzer proposed a model to describe bacterial chemotaxis that established a relation between the velocity profile and the stationary density for run-and-tumble particles in 1D [79]. Particles move in a direction with speed module $v(x)$ and change speed direction with a constant rate λ (tumble rate). The equations, derived from the continuity in the flow and the conservation of particle number, can be written

as:

$$\begin{aligned}\frac{\partial R}{\partial t} &= -\frac{\partial (vR)}{\partial x} - \frac{\lambda R}{2} + \frac{\lambda L}{2} \\ \frac{\partial L}{\partial t} &= \frac{\partial (vL)}{\partial x} + \frac{\lambda R}{2} - \frac{\lambda L}{2}\end{aligned} \tag{3.1}$$

where R and L both depend on (x, t) and represent the densities of the particles moving to the right and to the left, respectively. Defining the total density of particles $\rho = R + L$ and the unbalance between right moving and left moving particles $\sigma = R - L$, Equations 3.1 can be re-written as:

$$\begin{aligned}\frac{\partial \rho}{\partial t} &= -\frac{\partial (v\sigma)}{\partial x} \\ \frac{\partial \sigma}{\partial t} &= -\frac{\partial (v\rho)}{\partial x} - \lambda\sigma\end{aligned} \tag{3.2}$$

Defining the net flux of particles as $J(x) = v(x)\sigma(x)$ and imposing it to vanish at the boundaries, the solution for the stationary state is $\sigma = 0$, which corresponds to a situation of a balanced density of right- and left-moving particles. Furthermore, it holds that:

$$\rho(x) = \rho_0 \frac{v_0}{v(x)} \tag{3.3}$$

resulting in the possibility to tune the bacterial density, solely modulating their speed. These same results can be recovered by modeling bacterial dynamics as that of particles subjected to gaussian coloured noise in 1D [86].

The key idea to bear in mind for the experiments is that turning off the propulsion in a region of the system leads to an accumulation of particles, while increasing the propulsion leads to a depletion.

3.2 HCB437 PR$^+$ in 2D geometry

Compared with the theory, the experiments are complicated by the biological nature of our microswimmer model, and are strongly affected by the delayed response to light. We started by projecting a green light pattern with a circular dark hole in the middle on samples of HCB437 PR$^+$ bacteria sealed in glass capillaries or between two glass slides, since at that time the HLK strain was not available yet. We tested the samples in different conditions, changing the distance between top and down surfaces in a range from 20 µm to 400 µm. In these geometries, the combination of 3D-swimming and the history-dependent light response dynamics (due to ATP production) flattens the observed velocity profile, despite the steep gradients in the projected light pattern. Indeed, we did not observe any relevant density modulation

in the field of view.

A key-point to take into account is that our microswimmer is not a mere single entity, but it lives immersed in a liquid with other particles. There are many studies demonstrating that interacting systems at high density in homogeneous media give rise to a broad spectrum of interesting phenomena (*e.g.* motility-induced phase separation (MIPS) [87], collective behaviors [88]). We thought that combining steric interactions with our light-driven bacteria, we could obtain a relevant modulation of the density, in a similar fashion to that previous proposed in numerical works of 'light-driven' active particles [89, 90]. However we could obtain a maximum density that of 10^{10}cells/mL, corresponding to a cell-body volume fraction $\phi \approx 0.02$ (considering a bacterial volume of 2 µm^3), too low to obtain relevant interaction effects. To taking advantage of these further interactions, we designed and fabricated a microstructure with quasi-2D geometry. This device (described in details in Section 5.4.1) allows to increase the density of motile bacteria in our field of view and make the most of steric interactions [91]. We believe that bacterial collisions, and consequently alignments and reorientations, change the shape distribution of path length of *E. coli* going through a dark area. The more bacteria follow longer path to find the exit from a given low motility region, the greater the probability that they finish their fuel (pmf) and get "trapped" inside the dark, low motility region. Moreover, as for MIPS, when the density of cells starts to increase in this region, then the probability to get "trapped" there becomes higher as well, establishing a positive feedback.

Figure 3.1 shows the results we obtained by projecting in the field of view a green light pattern (1.5 mW/mm^2) with a circular dark region in the middle. We varied the radius of the dark area to see how the radial density profile could be affected by this change. We see that increasing the radius of the circle, the accumulation peak moves out from the center of the structure.

This phenomenon can be captured also by the simple RC circuit model described in Section 2.2. According to this model, a bacterium is trapped in the dark if the path length of its trajectory in the dark reaches $v_0\tau_{\text{off}}$, where v_0 is its speed when it enters the dark region (otherwise it would escape) and τ_{off} is the characteristic time of the speed exponential decay (Eq. 2.3). We simulated this system in the case of non-diffusing and non-interacting straight swimmers, and we observed the accumulation of all particles in the circle only for $R > v_0\tau_{\text{off}}$, otherwise we could get just a slight density modulation. The next step was to put our effort in figuring out some model to fit the experimental data strongly chatacterized by the ATP production dynamics that increase τ_{off} in an unknown way.

In the experiment just described the green light intensity corresponds to low speeds. Looking at the experimental data on the time response of this strain (Fig. 2.6)

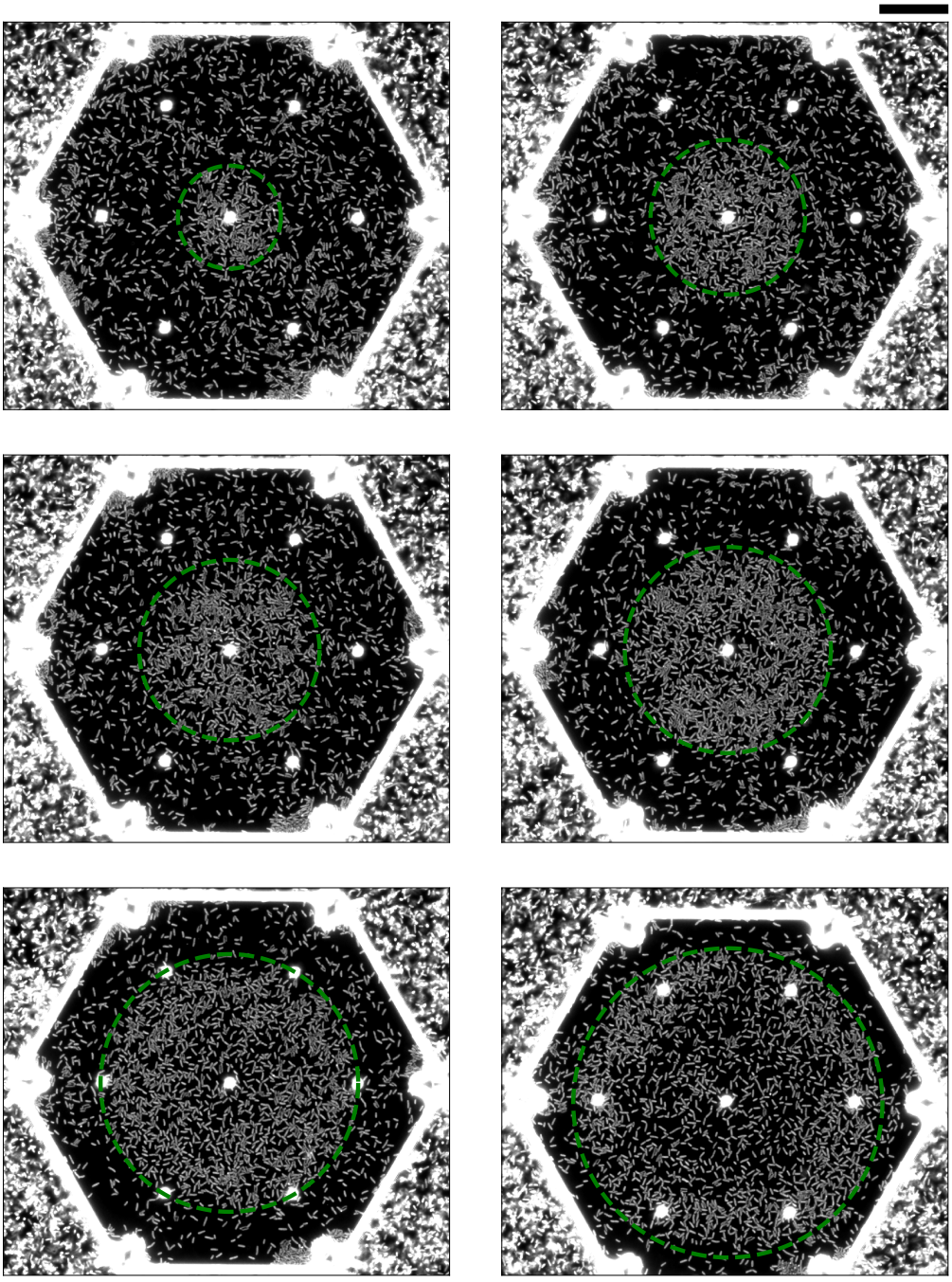

Figure 3.1. Projecting circles We show the accumulation of HCB437 PR^+ bacteria inside the dashed circle induced by the green illumination pattern outside the (1.5 mW/mm^2). We show the results for 6 different radii between 31 µm and 92 µm. For larger radii the accumulation of the cells at the boundary of the circle can be observed. Cells produce less ATP given the smaller illuminated area inside the structure and cells need less time to stop in the dark region. Bacteria are confined between a coverglass and a microfabricated roof in a pseudo-2D geometry. The white spots in the images represent columns holding up the roof and fixing the height of the chamber at $\approx$ 1.4 µm. The scale bar is 10 µm.

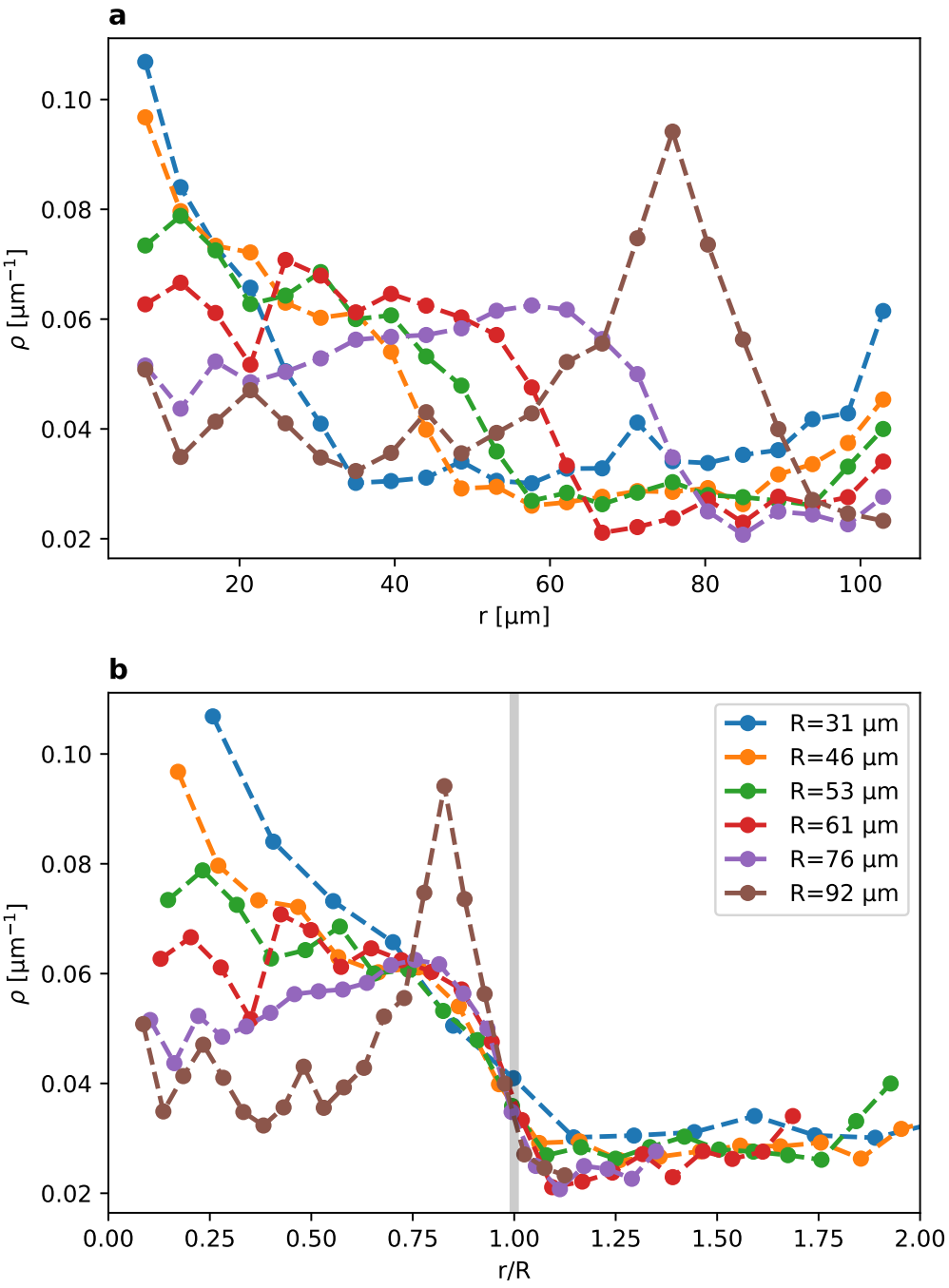

Figure 3.2. Radial density profiles. **(a)** Radial density profile obtained from the analysis of the data shown in Fig. 3.1. **(b)** Profiles plotted rescaling the x-axis with respect to the radius of the dark circular region R. It can be observed that the accumulation peak moves towards a value of 1.0 as the circle radius increases. This effect is due by the finite stopping time of bacteria in dark regions.

we realized that higher intensities would give a boost to the ATP production, thus increasing memory effects ($\tau_{\text{off}}, \tau_{\text{on}}$). We started to study how the radial stationary distribution would be affected by light intensity, and how the memory effects would influence the final distribution. We observed that the accumulation did not have place when the light outside was increased. Unfortunately, during these measurements, we experienced some problem. First of all it was hard to define a stationary state since the chamber was continuosly depleted of motile bacteria. Since the DLP cannot power bacteria in all the sample but, just in a limited area, bacteria tend to escape from this area and accumulate at the boundary. To reduce this effect we projected just a green annulus with internal radius of 60 µm and the external of 120 µm ($\approx$ the size of the structure), rather than projecting a full green pattern outside the circle. In this way we can increase the time for completely deplete the bacteria inside the chamber. After more than one year of experiments with the microstructure device and without any change to the fabrication protocol, we could not get anymore chambers perfectly adhering to the coverglass. This experimental complication, coupled to the idea of canceling out the ATP production (as described in Section 2.2) halted our work in this direction for the moment. We hope to solve this problem in the future, hopefully leading us to fully understand the connection between the PR and the ATP production.

Sample preparation and observation To prepare the samples for this experiment we fabricated the microstructure on a microscope cover glass. Then we dried on this same glass a solution of 10 µm-diameter silica beads ($\sim$ the height of the structure). A drop of motility buffer ($\approx$ 1 µL) is placed on the microstructure to prefill it, otherwise bacteria would be quickly sucked inside the structure for capillarity and the entrances would get clogged. The cover glass is placed on the glass slide and filled thanks to surface tension forces with a suspension of HCB437 PR$^+$ ($\sim 5 \cdot 10^9$cells/mL). The right amount of liquid is used to avoid lifting of the glass from the microstructure roof. This accuracy allowed us to get rid of a relevant background from out-of-focus swimmers. We sealed the sample using vacuum grease. Dark field images are collected on an self-built inverted microscope equipped with a 20x (NA = 0.5) objective and a high-sensitivity CMOS camera (Hamamatsu Orca flash 2.8)

3.3 HLK in 3D geometry

The HCB437 PR$^+$ strain is not the best strain to be used for obtaining density modulations and a model to predict the spatial speed field in presence of a light pattern is not available. This is due to the ATP dynamics, which introduces big

non-local effects, in turn decreasing our ability to shape the velocity field, also in the case of simple patterns.

To reduce non-locality in cell dynamics we created the HLK strain by excluding the ATP dynamics from the process (Section 2.2). A shorter τ_{off} leads to an increased resolution of colony shaping. Actually, the first time we projected the green pattern with a dark circle on a hypoxic sample of HLK cells, we were surprised by the precision in the definition of the bacterial accumulation we could obtain.

We then immediately started to project more complex patterns in the sample. We applied this system to reproduce the bacterial portraits of people special for us, such as: Albert Einstein, Charles Darwin and the legendary captain of football club A.S. Roma, Francesco Totti. Figure 3.3 shows the average of one minute of dark-field microscopy images aquired (at 1 fps) after the sample is exposed for 3 min to the light pattern presented in the right panel. Similar to that observed for the 2D system, cells moving from illuminated area stop swimming and start accumulating at the boundary of the dark region, increasing the density in a $20 - 30$ µm width band. Assuming the exponential decay predicted by the RC circuit analog and knowing the measured stationary speed (Figure 2.9), we could estimate a maximum $\tau_{\text{off}} \sim 3$ s. We did not measure it directly since tracking is not available at the required density, and DICS is not optimal to obtain time dependent measures. However, looking at the samples with our own eyes, this estimated upper limit appeared not too far from the reality, although the larger part of the population responds with a shorter characteristic time <1 s.

Interestingly, we demonstrated that the assembled patterns are reconfigurable in real time. Tens of thousands of bacteria reproducing the image of Albert Einstein, an icon for physicists, are guided in few minutes to resemble Charles Darwin, an icon for biologists, (Fig. 3.4a) just changing the pattern illuminating the sample. To estimate the time necessary to obtain the reconfiguration, we have to define a quantity representing the distance between the obtained density $\rho(\mathbf{x})$ and the desired one $\rho_{target}(\mathbf{x})$. We chose the squared target distance:

$$\chi^2 = \langle \Delta\rho^2 \rangle$$

where $\langle \cdot \rangle$ stands for the average value over every pixel in the field of view and $\Delta\rho(\mathbf{x}) = \rho(\mathbf{x}) - \rho_{target}(\mathbf{x})$. To evaluate χ^2 we first need to estimate the density $\rho(\mathbf{x})$. In dark-field microscopy, neglecting multi-scattering, all particles in the focal plane are visualized on the camera, and trasformed through the point spread function. Since each frame represents a configuration of particles, the average density of the particles (ρ) is related to the frame average over a time window (F) by a linear

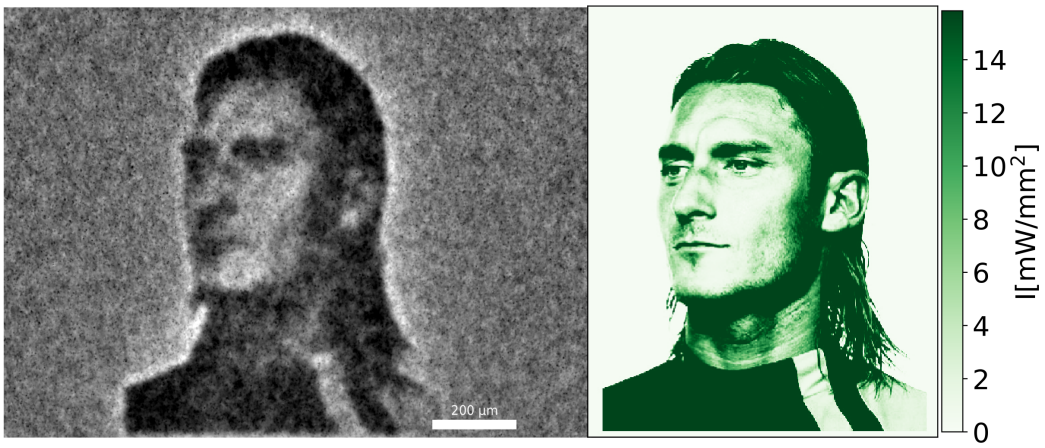

Figure 3.3. Density control with light. On the left we show the average density of Hulk cells after the sample is exposed for ≈ 3 minutes to the light pattern (on the right). Cells moves away illuminated region, depleting them. When they swim into the dark, their motility goes down and they become trapped, creating an accumulation region of $20 - 30$ µm width.

relation:

$$\rho(\mathbf{x}) = aF(\mathbf{x}) + b$$

where a is a scaling factor that makes ρ independent by the illumination level, and b takes into account for a baseline level given by bacteria out of the focal plane as well as impurities that may be present in the sample. To evaluate these two parameters we tested two different methods. The first one is based on the calculation of the two parameters minimizing the $\chi^2(a, b)$ obtained by resolving the equations:

$$\begin{cases} a\langle F\rangle + b - \langle \rho_{target}\rangle = 0 \\ a\langle F^2\rangle + b\langle F\rangle - \langle F\rho_{target}\rangle = 0 \end{cases}$$

However, this method improves the χ^2 giving big weight to the pixels found at the extreme of the intensity distribution, thus neglecting the grey scale dynamic range. Then, to avoid this problem, we decided to apply to our data the second method, more phenomenological and based on histogram stretching. We rescaled the histogram of pixel intensities such that the 10th and the 90th percentiles of $\rho(\mathbf{x})$ are the same of $\rho_{target}(\mathbf{x})$.

Figure 3.4b shows the normalized χ^2 measured relatively to the "Einstein" and "Darwin" pattern (Fig. 3.4c1,c2). The time evolution of χ^2, after the pattern switch at $t = 0$, is well fitted by an exponential with a baseline. The dynamics of disassembly and assembly of a pattern are on the same time scale, the characteristic times fitted

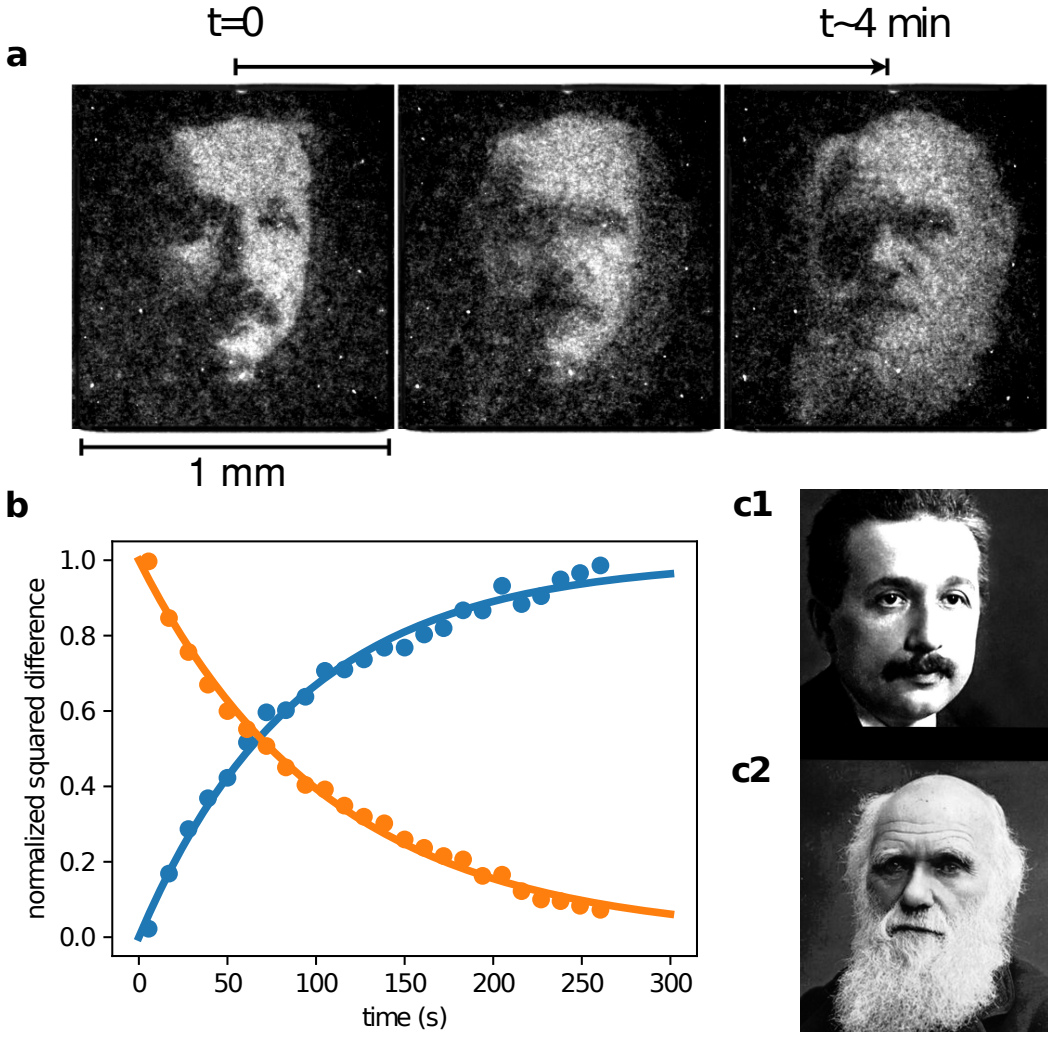

Figure 3.4. Dynamical control of density. **(a)** About 50000 Hulk cells are made to morph from Einstein to Darwin by spatially and dynamically modulating the swimming speed with light. Cells appear in white in dark field microscopy. At time $t = 0$ we switched the illumination pattern from **(c1)** to **(c2)**. **(b)** Orange and blue circles represents normalized values of χ^2 relative to the target density in Figures **(c1)** and **(c2)** respectively. Data are well fitted by an exponential plus a baseline (solid lines). The time scale of this phenomenon is captured by the fitted characteristic times ($\tau_1 = 107.3 \pm 6.4$ s, $\tau_2 = 90.3 \pm 6.6$ s).

are $\tau_1 = 107.3 \pm 6.4$ s and $\tau_2 = 90.3 \pm 6.6$ s, respectively.

Not satisfied with this result, we decided to improve the quality of our portraits by introducing a real-time feedback loop regulating the light pattern. We were able to refine the details of the images in the areas in which they diverged from the desired result. This approach allowed us to avoid to build a complicated model that hat to take into account all the biological complexities (*e.g.* τ_{off}, stator disassembly [75] and aging of the sample) to optimize the illumination pattern for a ρ_{target}. The feedback loop we designed stands on the key idea that increasing the light power $I(\mathbf{x})$ on the area around $\mathbf{x}$ leads to a density decrease $\rho(\mathbf{x})$. We found the transformations connecting the DLP and the camera, such that one pixel of the DLP resulted in a 1.94 µm-side square once projected onto the sample. At each step of the loop we recorded a 2 s video to capture the system configuration and to calculate $\rho(\mathbf{x})$. We applied Gaussian filtering, with a standard deviation, of ≈ 1 µm to $\rho(\mathbf{x})$, thus reducing the roughness of the "painting" due to the discrete nature of the "ink" (the body of the bacterium). Then we proceeded updating the illumination pattern such that the pattern at the step $n+1$ is:

$$I_{n+1}(\mathbf{x}) = I_n(\mathbf{x}) + \alpha \Delta\rho(\mathbf{x})$$

where α is a parameter that can be used to speed up the updating process (set to 0.2). We then applied this feedback loop system trying to reproduce as ρ_{target} a portion of the Mona Lisa portrait by Leonardo Da Vinci. Figure 3.5 shows the results we obtained. We projected the negative pattern ($-\rho_{target}$) on the sample and we monitored the evolution of $\chi^2(t)$ during the reconfiguration of bacteria (Fig. 3.5e). When the χ^2 became stationary we turned on the feedback loop (shaded area) to study the improvement of the quality of the image we could obtain. Fitting the $\chi^2(t)$ as two decaying exponential connected in the point where the feedback loop was started, we could estimate a 25% reduction of χ^2. Figure 3.5a,b shows the recorded image before the beginning of the feedback loop and at its end, respectively. Figure 3.5c,d shows the patterns illuminating in the sample in the same intervals of Figure 3.5a,b. The improvement in the refinement of details (*e.g.* eyes, nose, mouth) can be clearly appreciated. Figures 3.5a,b,c,d are the averages over 7 steps of the feedback loop.

Furthermore we analyzed the frames collected before the beginning of the feedback loop to check if we could recover the classical Schnitzer relation (Eq. 3.3). The relation in Eq. 3.3 is valid for a population of bacteria, all moving with the same swimming speed. In the case of swimming speeds broad distributed Eq. 3.3 can be written as $\rho(x) \propto \overline{v^{-1}(\mathbf{x})}$ [92], where the bar stands for the value averaged over the population distribution $P(v)$. We have shown in Section 2.2 that the

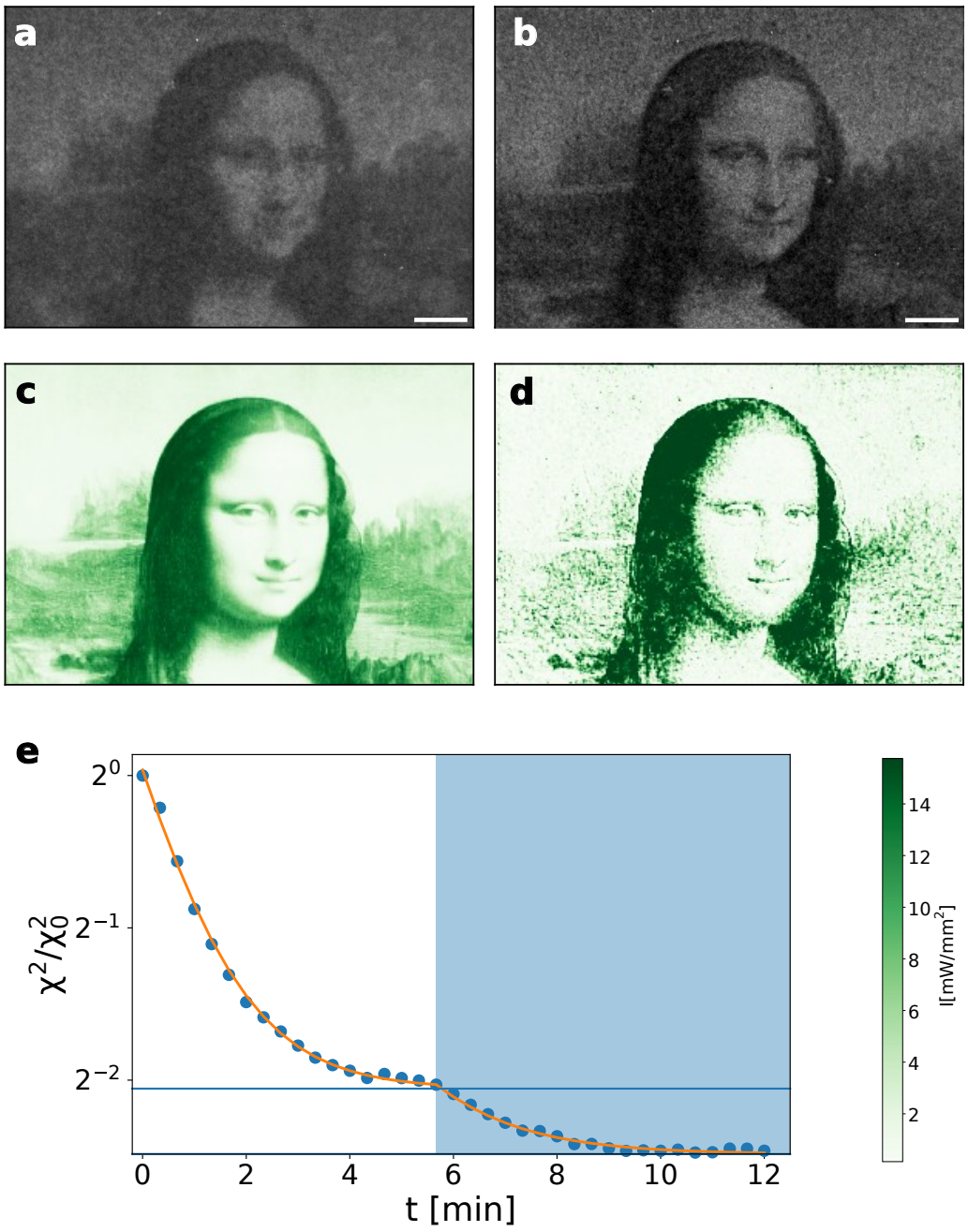

Figure 3.5. Real-time feedback loop improvement. **(a, b)** Average of the dark field images captured over the last 7 steps before the feedback loop is started and at the end, respectively. The scale bars are 200 µm. **(c, d)** patterns projected on the sample in the same intervals of **(a, b)**, respectively. **(e)** The evolution of the squared distance from the target $\chi^2(t)$ before and after (shaded area) the feedback loop is started. The feedback loop improves the χ^2 with a reduction of 25% with respect to the initial static pattern.

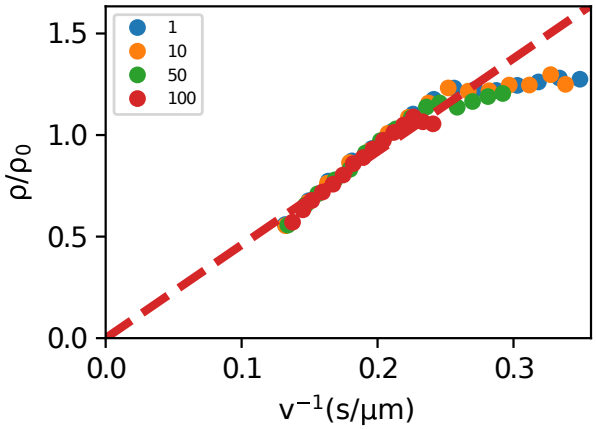

Figure 3.6. The theory is recovered for high speed. Circle are the bacterial density as function of the expected speed value in the same position. The PMF dynamics and the diffusion of particles modify this relation for low speeds. Different colors are used to that applying a Gaussian filter (at different amplitude) to the maps for $\rho(\mathbf{x})$ and $v(\mathbf{x})$ the relation seems satisfied. The Gaussian filter should reduce the contribute of particle diffusion and PMF dynamics.

speed distribution for different level of light depends by the single variable $vf(I)$, rather than v, I separately. Then we can consider the speed of a single particle j as function of I $v_j(I) = v_0^j f(I)$. From which follows that $\overline{v(I)} = \overline{v_0} f(I)$ and that $\overline{v^{-1}(I)} = \overline{v_0^{-1}} f^{-1}(I)$, since f(I) is common to all the population. This is translated in the relation:

$$\overline{v^{-1}(I)} \propto \overline{v(I)}^{-1}$$

This property let us to rewrite the relation $\rho(x) \propto \overline{v(\mathbf{x})}^{-1}$ and test the validity of this relation by using the average speed previously measured as function of intensity (Fig. 2.9). Figure 3.6 shows the relation between our estimation of ρ from the microscopy images and the reconstructed map of inverted speed. We applied a Gaussian filter to both the maps to test if non-local effect can be smoothed. Computer simulations show that this deviation can be explained phenomenologically by a model considering the diffusion of particles and the PMF dynamics rather than just its stationary state (data not shown)

Sample preparation and observation We injected bacteria in capillary glass tubes (Vitrocom) with near-squared edges and internal dimension of 4 mm×400µm. Images were collected on an self-built inverted microscope equipped with a 4x (NA = 0.13) objective and a high-sensitivity CMOS camera (Hamamatsu Orca flash 2.8). We set the focal plane 100 µm from the upper glass surface. We visualized the samples through filtered (Thorlabs - FD1R) dark-field illumination, to not excite the PR.

3.4 Discussion

We exploited engineered photokinetic *E. coli* to obtain a colloidal sample whose density can be arbitrarly shaped with light on the time scale of minutes. Furthermore we developed a method, based on a real-time feedback loop, that allows to increase the degree of control we have on this kind of active matter. Our results pave the way to obtain dynamical reconfigurable microfluidic devices, by driving and organizing engineered bacteria with light. Moreover the implementation of new engineered patterns in the cells could allow the irreversible assembly of region in the sample inducing the secretion of a polymer matrix like in biofilm formation [93]. This new 'feature' could be optogenetically controlled via the response to a different light wavelength [47].

We are now working on the possibility to exploit dynamical patterns to obtain net fluxes from photokinetic bacteria. Assuming a photokinetic bacterial system where the velocity pattern is a traveling square wave between two speed values v_0 and v_1 with $v_1 > v_0$ moving towards right. Setting the tumble rate to zero and the wave speed to v_1, then at the stationary state all the bacteria moving in the same direction of the pattern would swim with constant speed v_1, while the average speed of particles moving to the left would be $\frac{3v_0+v_1}{v_0+3v_1}v_1 < v_1$. This simple model results in a net flux, since the number of particles going to the left is equal to the number of particles going to the right. Additionally, preliminary simulations on run-and-tumble particles in 1D showed that, by reducing the wave speed to values lower than v_0, the direction of this flux can be reverted (data not shown).

Chapter 4

Light controlled 3D micromotors powered by bacteria

Dense suspensions of swimming bacteria display striking motion that look extremely vivid compared to the thermal agitation of colloidal particles of comparable size. This suspension are named active fluids and can be looked at as a special kind of fuel: a small droplet of an active fluid can be used to propel micromachines inside miniaturized chips, with no need of external driving fields or control. In these fluids energy is directly present in a mechanical form and the challenge is that of designing microstructures that are able to rectify the noisy and disordered motion of active particles into a reproducible and smooth directed movement. The first studies in this direction focused on the development of bacteria propelled microrobots [94, 95, 96, 97, 98] with potential applications for drug and cargo delivery. These bio-hybrid microrobots were based on microfabricated structures or microbeads with a biochemically functionalized surface. Swimming bacteria adhere to the surface and act as micropropellers, which can also be switched on and off by using chemical [94] or light signals [95]. Yet, the motion of these microrobots is random, so that directed motion can only be achieved by an external feedback action through optical stimuli [96] or magnetic fields [97]. Other studies focused on creating bacteria-propelled rotary micromotors. The first example was reported in [99], where gliding bacteria moving in narrow tracks were biochemically bound to a rotor that was pushed at rotational speeds of about 2 rpm. Still, the motion was intermittent, with continuous rotating phases lasting typically for a minute, and a consistent fraction (16%) of rotors were spinning in the opposite direction. Few years later a quite different approach was born based on the idea that, due to broken detailed balance

in active baths [92], unidirectional motion can also be achieved by spontaneous rectification effects induced by objects having asymmetric shapes [100, 101, 102, 103]. These bacterial ratchets do not require surface functionalization or external fields, they only rely on their morphology to induce self organization of bacteria into partially ordered configurations that apply a net force or torque on the object. These rotating flat structures roam unconstrained over an interface and this limits their usability in practical applications. Furthermore, the instantaneous arrangement of driving bacteria is highly stochastic resulting in temporal speed fluctuations that are comparable to the mean. For the same reason, a wide distribution of angular speeds is observed among different rotors.

We use two-photon polymerization (Section 5.1) to build composite 3D structures that autonomously capture bacteria into precise configurations exerting a stable and large torque on a rotor constrained to revolve around a fixed axis. We show that such structures can be fabricated in large arrays and that they independently rotate with a high and smooth angular speed. Additionally, using the photokinetic smooth-swimmers HCB437 PR^+ described in Chapter 2, we show that the speed of micromotors can be controlled through the intensity of illumination light. We can tune the speed of individual micromotors by independently adjusting their illumination levels with a spatial light modulator. Furthermore, through a real time feedback control loop, we command a set of micromotors to rotate in unison with a prescribed angular speed.

4.1 Results

4.1.1 3D micromotor design

Figure 4.1a shows the computer model of our micromotor design. The structure has three component parts. The rotating unit (appearing in green) has an external radius of 7.6 µm and a thickness of 3.7 µm. Its outer rim features 15 microchambers, each capable of accommodating one single cell body while leaving the entire flagellar bundle outside for maximal propulsion. The number of chambers a single rotor could carry is limited by the constraint that each chamber should be wide enough to fit one cell. Therefore the number of chambers is maximal when they are radially oriented but this configuration would also result in a zero torque. If we tilt the chambers by an angle θ the torque exerted by each cell will increase with $\sin\theta$ while the number of chambers will decrease as $\cos\theta$. As a result the total torque would go as $\sin\theta\cos\theta$ and have a maximum at $\theta = 45°$ which is the actual angle chosen in our design. In order to reduce fabrication time, the outer ring of the rotor is connected by four radial spokes to a central ring that is free to rotate around a vertical axis shown in

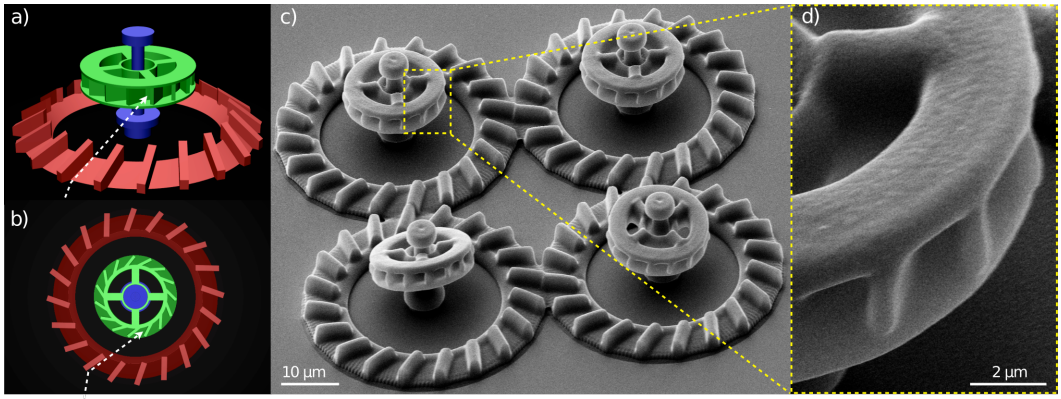

Figure 4.1. (a, b) 3D model of the micromotor structure. Colours highlight distinct component parts: ramp (red), axis (blue) and rotor (green). The dashed white line schematically depicts the trajectory of a cell guided by the ramp structure into a rotor microchamber. **(c,d)** Scanning electron microscope images of the 3D micromotors. **(c)** shows a bird's eye view on a set of four micromotors. **(d)** Shows a close view of microchambers.

blue. The top part of the axis has a wider cross-section to prevent rotor escape. A bottom platform on the axis keeps the rotor at a minimal height of ∼3 µm, thus reducing hydrodynamic friction with the solid substrate. Moreover, the elevated position keeps the rotor out of the high bacterial concentration layer that forms on the substrate surface [104, 105, 106]. There, random collisions with free swimming bacteria would disturb the rotor's operation making it slower and less stable. To facilitate the capture of bacteria by the rotor, we built a radial ramp structure (red component) that collects bacteria swimming on the bottom surface and directs their trajectories upwards to the rotor's microchambers. However, with a bare ramp only a fraction of bacteria would be sent along trajectories that reach the tilted microchambers with the correct orientation to enter it. To overcome this problem we placed a series of barriers on the ramp. Incoming bacteria will align and slide along the barrier leaving the ramp on a trajectory that is very likely to intercept the rotors edge with an angle matching the orientation of the microchambers (see dashed white line on Fig. 4.1a,b). All experiments were performed with non tumbling strains (smooth-swimmers) which can be stably trapped in an an empty hole by a constant flagellar thrust. Details of the actual structures, as seen by scanning electron microscopy (SEM), are shown in Fig. 4.1c) and 4.1d).

4.1.2 Self assembly of hybrid micromotors

We first immerse the structures in clean motility buffer (∼ 500 µl) and make sure that none of the rotors is stuck to the supporting axis. We then add ∼ 100 µL of a dense ($OD_{590} \approx 0.8$) cell supension resulting in typical surface densities of cells over

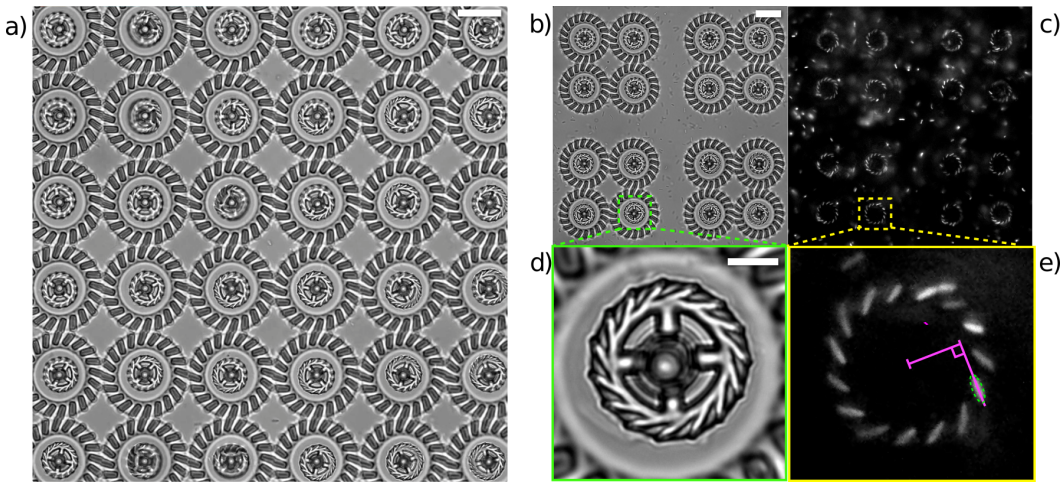

Figure 4.2. **(a)** Bright-field microscopy image of 36 rotating micromotors. The scale bar is 20 µm. **(b,c)** Array of 16 rotors used to characterize the rotational dynamics (Fig. 4). Cell bodies are clearly visible in fluorescence **(c)** showing the high occupancy fraction of microchambers. The scale bar is 20 µm for both **(b,c)**. **(d,e)** Zoomed view on one of the rotors in **(b,c)**. Cell bodies are fitted with an ellipsoidal shape shown as a dashed line in e. Solid lines illustrate the construction used to measure the lever arm ℓ. The scale bar is 5 µm for both **(d,e)**

the coverslip of about 0.015 cells/µm^2. Within few minutes after the addition of bacteria, the rotors start to capture cells and rotate. This self-assembly mechanism is very robust, practically every single rotor spins even in large and dense ensembles such as the array of 36 rotors shown in Fig. 4.2a. We transformed a plasmid codifying an RFP under an IPTG inducible promoter (BBa_J04450) in the smooth-swimmers strain HCB437. Expressing this protein we visualize the cell bodies captured inside the microchambers using epifluorescence microscopy (Fig. 4.2c,e). To characterize the dynamics of this self assembly process we recorded a sequence of bright-field clips (2 s) intercalated by short clips (0.1 s) in epifluorescence mode throughout the entire fill up process. Bright field clips are used to track rotational speeds of individual rotors while simultaneously keeping track of the corresponding number of trapped cells observed in fluorescence images. Fig. 4.3a shows the number of captured bacteria as a function of time. The average number of occupied microchambers (shown as red crosses) reaches the 90% of its maximal value (13.5) after only 2 minutes. The overall time behavior can be very well fitted by an exponential law with a time constant of 49 s and a saturation value of 14.4 (96%). We find that the rotational speed increases linearly with the number of captured cells (Fig. 4.3b) with each cell contributing a speed increment of 1.2 rpm.

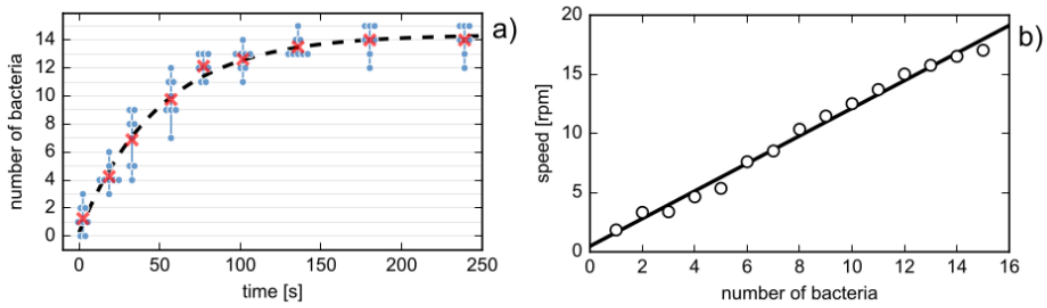

Figure 4.3. Self-assembly dynamics. (a) The number of captured bacteria as a function of time is plotted as blue disks for 8 micromotors. Groups of blue dots connected by vertical lines refer to the same time instant. The average over the 8 micromotor group is plotted with red crosses and fitted to the exponential law shown as dashed line ($\tau = 49$ s). **(b)** Rotational speed as a function of the number of captured bacteria (open circles). Linear fit (black line) gives a slope of 1.2 rpm per cell.

4.1.3 Characterization of rotational dynamics

Using a feature detection algorithm [107] we extract the orientation angle of rotors from image sequences acquired at 50 fps under bright-field illumination. Figure 4.4a shows the cumulative rotation angle for 16 rotors as a function of time. The average angular speeds of individual rotors are distributed in a narrow range around a mean value of 17.8 rpm (1.4 rpm standard deviation). The gray line in Fig. 4.4b shows the time trace of the instantaneous speed of a single rotor obtained from the angle difference between successive frames. The speed displays rapid fluctuations with a standard deviation amounting to 19% of the mean value. Fourier analysis (Fig. 4.4c) reveals a characteristic noise frequency of about 15 Hz which is compatible with the typical wobbling frequency of freely swimming bacteria [108]. If we apply a low pass filter with a cutoff at 10 Hz the remaining fluctuations are quite small (color curves in Fig. 4.4b) and only give rise to a 4.9% broadening of the rotational speed in individual rotors.

In our design we use an axis to constrain lateral motions of the rotor and minimize hydrodynamic coupling with the solid substrate. However, the presence of the axis itself might introduce an extra friction term due to the sheared fluid in the gap between the rotor and the axis. To quantify the magnitude of these effects we measure the rotational drag of the rotors by tracking their angular Brownian motion in the absence of bacteria. The measured value of 9.4 ± 0.2 pN µm rad^{-1} is close to the theoretical value [109] of 8.6 pN µm s rad^{-1} calculated for an oblate ellipsoid with equivalent aspect ratio and volume. This confirms that the rotor has a minimal rotational drag for its size, meaning that it is not affected significantly by the proximity of the coverglass surface or the axis. From the measured rotational drag we can evaluate that an external torque of 17.5 pN µm would be required to

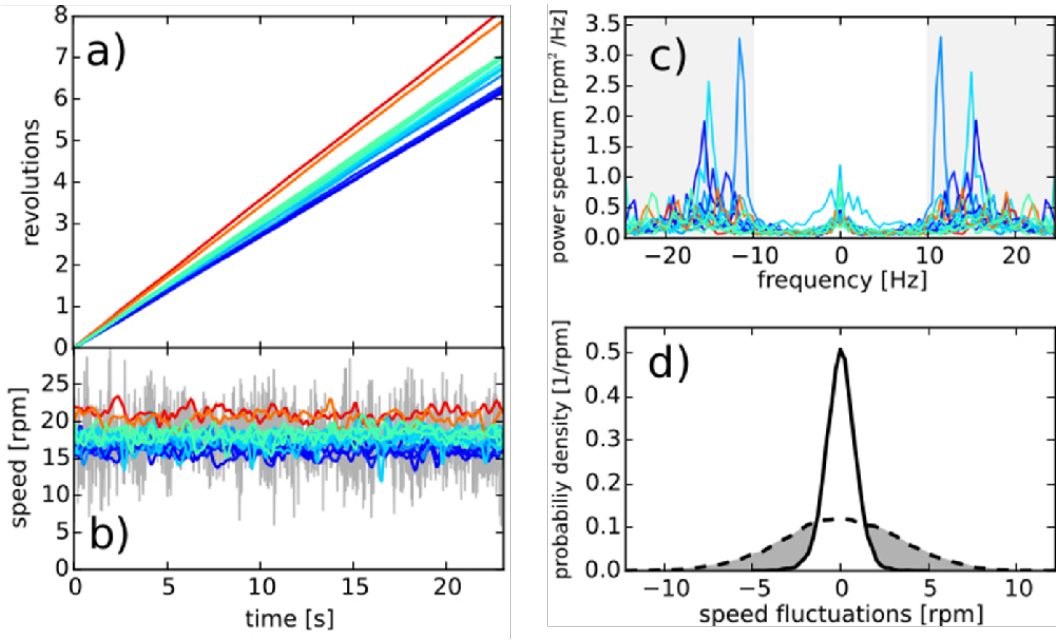

Figure 4.4. Characterization of rotational dynamics. **(a)** Cumulative angle as a function of time for the 16 micromotors shown in Fig. 2b, colour scale encodes the average rotational speed from low (blue) to high (red). **(b)** Instantaneous rotational speed of the 16 rotors before filtering (grey line, only shown for one rotor) and after the low pass (10 Hz) frequency filtering (coloured lines, shown for all rotors). **(c)** Power spectra of the speed fluctuations. High frequency regions (410 Hz) are marked with a grey background and filtered out. **(d)** Probability distribution of the fluctuations of the rotational speed before filtering (dashed line) and after filtering (full line).

spin an empty rotor at the same speed as that observed in the bacterial bath. Since a rotor holds 13.5 bacteria on average, we find that a single cell provides an effective torque of 1.3 pN µm. By analyzing the spatial arrangement of bacteria, as observed in fluorescence images like 4.2e), we extract the lever arm ℓ as the distance of the rotor center from the line passing through the cells major axis. We find an average value of $\ell = 6$ µm resulting in an effective pushing force per cell that is 0.2 pN. This value is about half of the typical flagellar thrust reported in the literature for *E. coli* cells [110, 111]. Although flagellar thrust can vary with strain, medium composition and other experimental conditions, a possible explanation for the low value obtained could be that flagellar bundles extending out of the structures will generate a counter rotating flow that could result in an effective rotational drag that is higher than what measured during free Brownian motion. Moreover, when the rotor is loaded, small asymmetries in bacteria configuration also result in an applied net force that maintains the rotor in close contact with the axis. This could also result in an increased rotational drag.

When comparing to previous 2D bacterial ratchet motors [100, 101] there are few quantitative considerations that are worth mentioning. We could easily achieve rotational speeds of 20 rpm corresponding to a linear speed of the outer rotor edge of 16 µm/s, which is very close to the speed of freely swimming bacteria ($\sim$ 20 µm/s) in our experiment. For 2D ratchet motors typical rotational speeds were 1 rpm with a corresponding edge speed of 2.5 µm/s. 2D motors display large speed fluctuations (100%) both in time and among rotors. We observed that practically every motor rotates with an average speed that only fluctuates by 8% (s.d.) among rotors, and with time fluctuations of only 5 % (when noise components faster than 10 Hz are filtered out). Finally 2D rotors required high bacterial concentrations (10^{10} cell/mL) limiting the durability of these micro-machines. In contrast 3D motors spin much faster in a much more diluted bacterial suspension (10^8 cell/mL).

4.1.4 Tuning global rotational speed with light

An important issue for bacteria driven micromotors is that the rotational speed is uncontrolled and can vary a lot depending on the motility characteristics of the actual bacterial bath. More importantly, bacterial motility drops down quite abruptly if the oxygen and the energy-yielding nutrients are depleted from the medium by the cells [7]. This limits the lifetime of bacteria powered micromotors in sealed samples that do not guarantee the constant supply of oxygen and nutrients required for cellular respiration. By using HCB437 PR^+ bacteria and a green light source, we are able to preserve cell motility even in a hermetically sealed sample and to externally tune the speed of micromotors, substaining cell motility using photon energy as fuel.

We obtain light controllable micromotors by preparing sealed samples of microstructures in a suspension of HCB437 PR+. We first characterize the rotational speed of self-assembled micromotors as a function of green light power. Fig. 4.5a shows the speeds of a set of micromotors as the light intensity was systematically lowered in discrete steps while allowing enough time for the motors to reach a stationary speed at each light level. The datapoints are well fitted by an hyperbola, in accordance to the model of proteorhodopsin-generated PMF described in Chapter 2. To characterize the dynamical response to light we then modulate the illumination intensity between 1.2 and 71 mW/mm^2 with a square wave having a period of 8 seconds. The resulting speed of a micromotor is plotted as a function of time in Fig. 4.5b and clearly shows the presence of a dynamical modulation. To better quantify the response raise and fall times we compute the average response over 10 periods (Fig. 4.5c). We fitted the average response with two exponentials. We obtain a rise time of 0.49 s which is significantly shorter than the fall time 0.73 s as could be expected since the rotors were previously illuminated for a while to let them fill and thus the accumulated ATP substain the cell motility.

4.1.5 Energy considerations

The mechanical power generated by each motor can be estimated by multiplying the measured rotational drag (9 pN µm s rad^{-1}) by the square of the typical angular speed 1.9 rad/s (18 rpm). The value we get for the output mechanical power is $\approx$ 30 aW per rotor. It is now interesting to compare this value with the rate of energy consumption. In the previously described experiments input energy is of two different kinds: chemical or optical. For chemically driven rotors, if we assume that glucose in the buffer is the primary energy source, we can estimate the rate of energy consumption by multiplying the glucose consumption rate per cell ($\approx$ 7 amol/min/cell [7]) by the energy yield of glucose oxidation ($3 \cdot 10^3$ kJ/mol) and by 15, the number of cells per rotor. The resulting consumption rate of chemical energy is about 5 pW. The conversion efficiency from chemical energy to mechanical work is therefore of order 10^{-5}. In light-driven rotors, when both glucose and oxygen are absent, the primary source of energy comes from photons which impinge on the structure with a typical energy flux of a few mW/mm^2 (Fig. 4.5a). The total optical power flowing through a single structure of radius 8 µm is then of order µW resulting in an efficiency of light-to-work conversion of order 10^{-11}. Although this is a very low efficiency, still it is much larger than what obtained when rotating microscopic objects through direct transfer of optical momentum [112].

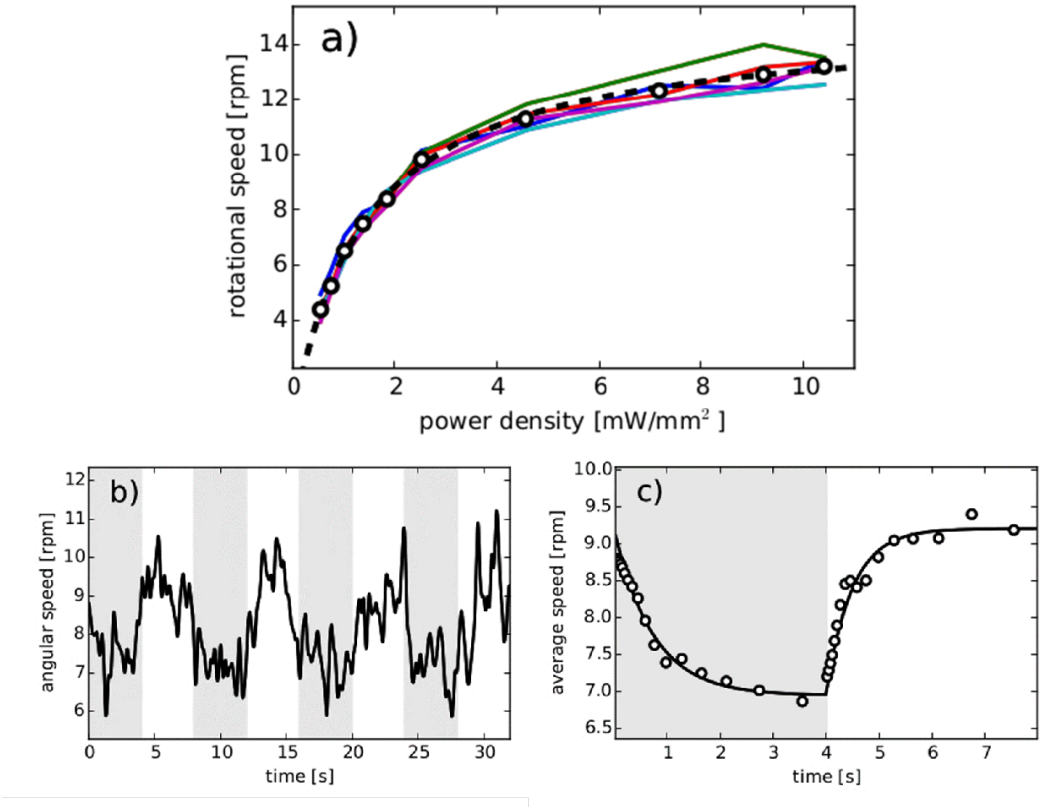

Figure 4.5. Light modulation of rotational speed. **(a)** Solid lines represent the rotational speed of 5 micromotors obtained by progressively lowering the illumination power. The power dependence of the 5 rotor average speed (open circles) is very well fitted by a hyperbola (dashed line). **(b)** Dynamic response of rotational speed (full line) to a square wave-modulated light intensity (8 s period). The half periods with low light are represented with a grey background. **(c)** Rotational speed averaged over 10 periods (points), the full line represent a fit with two exponentials.

4.1.6 Closed loop control of individual micromotor speeds

We have shown that light can be used to switch motors on and off and to tune their rotational speed. Using light as the control field has the enormous advantage that light can be shaped in time and space with a much higher precision than what is attainable with other possible control strategies such as by modulating the chemical environment [101]. This allows to rapidly and independently address individual rotors by projecting on each structure an illumination disk with variable intensity. We produce such structured illumination patterns by coupling a Digital Light Processor (DLP) to a custom built optical microscope as described in the previous Chapter. We start by illuminating 6 target structures with 6 illumination disks having the same light intensity. We then track the angular motion of the motors and consequently update the 6 light levels with a real-time feedback loop. The feedback algorithm is such that the illumination level of the i-th disk at iteration step $n+1$ is:

$$I^i_{n+1} = I^i_n \nu_0 / \nu^i_n \tag{4.1}$$

where ν_0 is a target rotation frequency while ν^i_n is the frequency of the i-th rotor at iteration step n. The algorithm clearly converges when all rotors spin with the same frequency ν_0. Before the loop switches on the rotors are uniformly illuminated and their rotational speeds range from 6.5 to 9.0 rpm. The feedback loop starts at $t = 0$ and executes one iteration every 10 s (vertical dashed lines in Fig. 4.6). After only 3 iterations, the standard deviation of the micromotor speeds is reduced from 1 rpm to 0.2 rpm that is from 13% to 2.7%, as can be seen in Fig. 4.6b). This small dispersion is maintained as long as the feedback loop is running and requires constant adjustments of the light levels (Fig. 4.6c).

4.2 Discussion

We show that fast, low noise and light controlled bio-synthetic micromotors can be obtained via the self-assembly of 3D microstructures and genetically engineered swimming bacteria. Using multifocal direct laser writing we produce large arrays of composite microstructures having submicron features that guide and arrange individual cells into ordered configurations. Trapped cells exert a stable and highly reproducible torque on the rotors. When propelling bacteria express the light-driven proton pump proteorhodopsin, the motors can be embedded in sealed environments where light provides the required energy supply. Using light patterns that are shaped in space and time with a DLP, we can control the speed of individual micromotors by addressing them with distinct light levels. We design a feedback control loop that automatically updates light levels based on the actual speeds of the rotors obtained

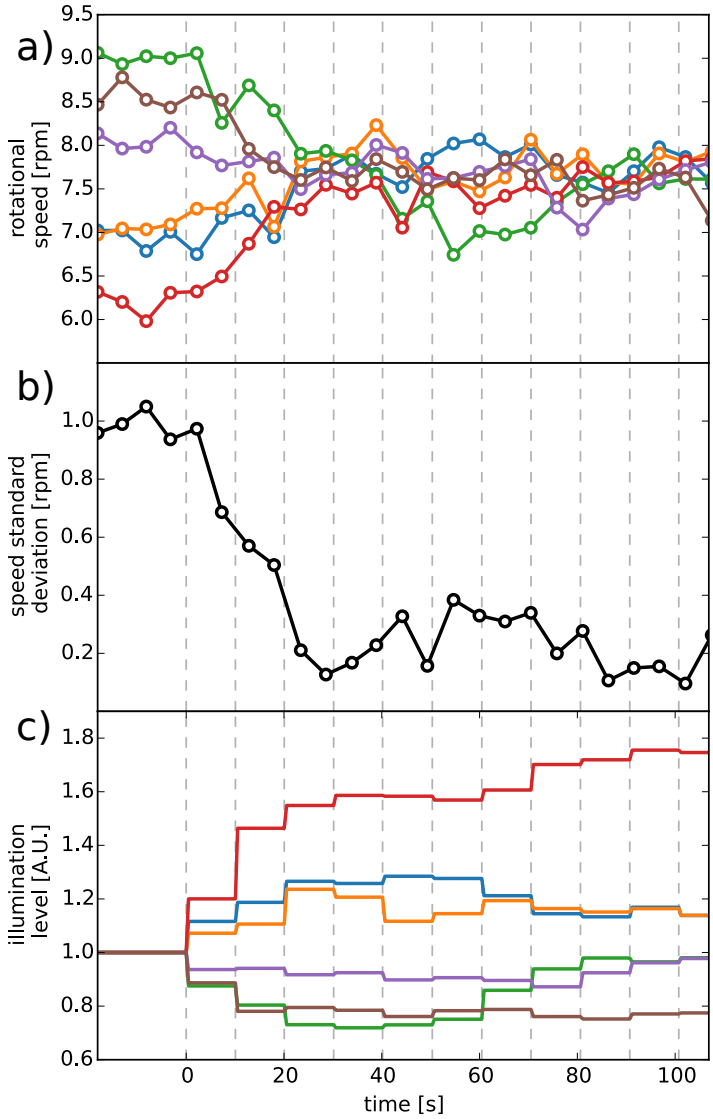

Figure 4.6. Closed loop control of individual micromotor speeds. **(a)** Rotational speeds of 6 micromotors driven by light powered bacteria. A feedback control loop is turned on at $t = 0$ and adjusts light levels on each rotor based on its current speed. The feedback loop operates with a 10 s time interval shown as vertical dashed lines. **(b)** The s.d. of the speed in the 6 rotor sample quickly drops when we switch on the feedback control ($t = 0$). **(c)** Solid lines represent the light levels over each micromotor (colour coding same as in **(a)**.

by real time video tracking. This allows to drive synchronously multiple micromotors and compensate for speed fluctuations in real time. Future studies may try to explore the role of hydrodynamic coupling between nearby rotating units. This could lead to higher speeds when using different rotor lattices with alternating rotational directions. Differently from previous work on synchronization of rotors [113], our micro-motors are torque free. Consequently hydrodynamic interactions will have a shorter range but also a different structure. Investigating hydrodynamic couplings in these self propelled systems could reveal novel synchronization effects that could be systematically studied by exploiting the independent light tunability of coupled rotors.

Part II

Methods

Chapter 5

Optics

5.1 Fabrication using two-photon polymerization

We used two-photon polymerization (TPP) to fabricate the microstructures for our experiments. TPP is a 3-dimensional microfabrication method capable of creating micron sized structures with submicron resolution [114].

TPP works with negative-tone photoresists, materials composed of monomers that polymerize or cross-link with each other upon UV excitation. Such photoresists are mostly used in 2D photolithography to create microelectronic circuits or microfluidic chips []. Tipically 2D photomasks shape light to expose geometric patterns into a layer of photoresist. The exposed parts of the layer will polymerize, forming the desired structure, while the unexposed areas are washed away by a solvent during the development of the sample. Stereolithography extends this fabrication process to 3D geometry by using a tightly focused laser beam to confine the photoresist polymerization into a small region around the focus, which is called "voxel" (volume-pixel). By moving this polymerizing spot, 3D microstructures can be fabricated. However this method is limited by the fact that the fabrication laser is not only absorbed in the focus but at every point of the beam proportionally to the local intensity $I(\mathbf{r})$. Thus the intesity of the beam focus decreases as it goes deeper in the photoresist layer. Furthermore the shape of the voxel is highly elongated along the beam axis limiting the axial resolution. This two problems can be overcome by exposing the photoresist through two-photon absorption [115]. Two photon-absorption is a third order non-linear process, in which the energy for a molecular electronic transition is provided by the energy of two photons. Since this process depends quadratically on light intensity, the photopolymerization can be localized to the most intense part of the fabrication focus. In practice a femto-second pulsed laser is used for TPP to achieve the necessary photon density required for two photon absorption.

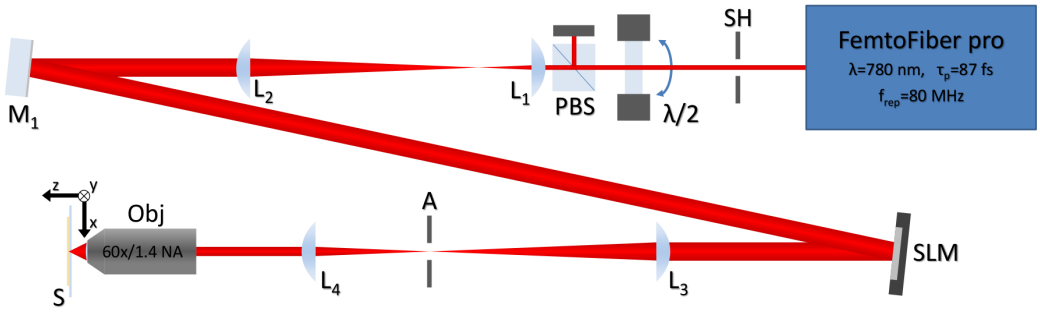

Figure 5.1. TPP setup. Schematic layout of our custom built two-photon polymerization setup.

The layout of our custom built two-photon polymerization setup is depicted in Figure 5.1. The setup is based on a near infra-red femtosecond fiber laser (FemtoFiber pro NIR, TOPTICA Photonics AG) with 780 nm wavelength, 87 fs pulse duration, 80 MHz repetition rate and 160 mW optical power. Exposure during fabrication is toggled by an optical shutter (SH). The fabrication laser power is set by a rotatable half-wave plate followed by a polarizing beam splitter cube (PBS). After expansion by lenses L_1 and L_2 the laser beam is reflected onto a holographic spatial light modulator (SLM) (X10468-02, Hamamatsu Photonics), which is in 4f conjugation to the back focal plane of a high numerical aperture oil immersion objective (Nikon Plan Apo Lambda 60x 1.4) by lenses L_3 and L_4. The SLM is used to generate multiple fabrication foci and to impose wavefront correction on the fabrication beam. The zero and the high diffraction orders can be blocked in the focal plane of L_3 by a thin wire and by an adjustable rectangular aperture (A). During fabrication the high NA focus of the laser is scanned inside a photoresist layer (S) carried on a microscope coverglass. Scanning is done by a 3-axis piezo translation stage (P563.3CD, Physik Instrumente (PI) GmbH & Co. KG) controlled through a NI-DAQ DA card.

For all the structures presented in this Thesis we used SU-8 2015 photoresist (MicroChem Corp). Strong adhesion of the structures to the carrier coverglass was ensured by a layer of Omnicoat adhesion promoter (MicroChem Corp). Scanning speeds and fabrication powers were in the range of 5-100 µms and 1.5-10 mW.

5.2 Tracking

In modern biological laboratories dealing with images analysis is ubiquituous. Technological advances brough to us optical technologies and instrumentation that can produce an enormous quantity of digital image [116]. This phenomenon caused an increased focus on the development of new methods to manage and process these data [117]. In this Section we present the software that we developed to characterize

the swimming behavior and response to light of *E. coli* cells from *in vivo* bright field, dark field and epifluorescence microscopy. The software is written in Python Programming Language[1] and takes advantage of OpenCV (Open Source Computer Vision Library)[2] for the image analysis part. Our procedure use an intesity-based detection technique combined with a pairing algorithm between detected objects from successive frames in a sequence. Moreover we propose a method to resew segmented trajectories. Since the final application of this software is to study the response of bacteria to light pattern well defined in a nearly 2D region, we focused our attention in following bacteria swimming on a solid surface (tipically glass) at the bottom of our samples. Furthermore to increase the efficacy of our tracking software we designed and microfabricated microstructures that collect swimming cells and confine them in a quasi-2D space. This geometry facilitates tracking eliminating out of focus and overlapped bacterial images.

5.2.1 Reconstruct trajectories

The reconstruction of a trajectory is based on heuristical algorithm costructed starting from experimental data. First of all we need to identify bacterial bodies in an environment where the background remains moderately constant and the target cell does not modify its appearance during microscopy videos recorded at constant frame rate. In order to estimate the static background, assuming that bacteria are homogeneously distributed, we can take the mean of all the frames present in the recording, averaging out the presence of motile bacteria. Subtracting this background to the original frames let us avoid to take into account the bacteria stack on the surface.
After that, each frame is thresholded and converted into a binary black and white image. In case of epifluorescence image where the light emitted can vary a lot among bacteria we apply a template matching algorithm to reduce this effect, using as template a gaussian with small σ to detect fluorophore particles inside the cells. In this way we are able to flattenized the bacterial intensity without modifying their contour profiles after the thresholding step. Using a Python function the binary image is used to identify connected cluster named contours from which the quantities of interest can be extracted:

- A_i: area
- $\mathbf{CM_i}(t)$: the center of mass the detected contour $(x_i(t), y_i(t))$

[1] https://www.python.org/
[2] https://opencv.org/

- l_i and w_i, the two major and minor axis of the ellipse fitting the body shape that we use as estimation of length and width of the bacterium
- $\psi_i(t)$ orientation of the cell body
- $F_i(t)$ fluorescence intensity.

Collision and overlapping of bacterial images can cause the wrong segmentation of their bodies, to avoid these mistakes we impose a threshold on the minimal area and one on the maximum of the fitted ellipse minor axis to select just contour obtained from isolated bacteria. From the list of **CM**s for every particle in every frame, the trajectories are reconstructed by considering two **CM**s in consecutive frames with index t and $t+1$ as being part of the same trajectory if no other **CM** in $t+1$ is closer to the one in t (up to a certain upper bound, above which the two particles are regarded as part of different trajectories). The main idea behind this approach is positing that in the small time interval between two frames, every particle has not moved much. This brute force approach consist in computing the distance matrix D_{ij}, each element of this matrix is the distance between the $\mathbf{CM}_i(t)$ and $\mathbf{CM}_j(t+1)$. This kind of operation scales quadratically with the average number of bacteria detected in a single frame. But using the NumPy Python library[3] and an array describing each **CM** as a complex number $[e^{x_i+iy_i}]$ we can just take the absolute value of the outer product of this array with himself to find D_{ij} to parallelize this computation. If no matches are found, the trajectory of such particle is considered complete and returned to the user. If a particle is not assigned to any **CM** detected in the previous frame a new trajectory is started. This approach works well in low density samples but it is not suggested for analysing images containing an high number of bacteria.

The obtained trajectories can be used to extract more information, like the displacement $\mathbf{d_t} = \mathbf{r_{t+1}} - \mathbf{r_t}$, from which we can evaluate the speeds $\mathbf{v_t}$ (Fig. 5.2). Plotting $\mathbf{v_t}$ as a function of time we can distinguish two regimes, the high speed regime puctuated by short periods of low speed respectively corresponding to running and tumbling phases [31]. Thus to detect tumbles we use an heuristic approach that identify tumbling events when the speed goes under a certain threshold [119]. We set the threshold as $0.75 \cdot \bar{v}$ where for a generic observable a $\bar{a}$ is the average along the trajectory segment. The tumble phases detected are then postprocessed to reduce the number of bad detection imposing a minimal tumble duration of 0.04 s and a minimal run duration of 0.1 s. This means that if a cell tumble twice in less than 0.1 s we consider those events as a single tumble.

[3] http://www.numpy.org/

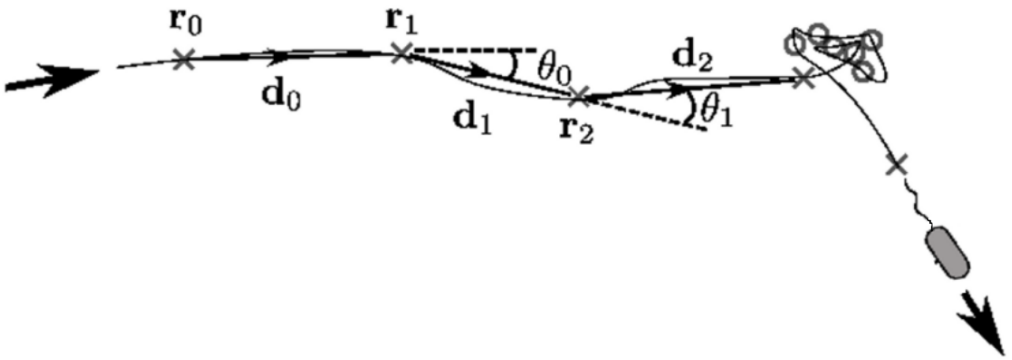

Figure 5.2. Reconstruction of the trajectory of an *E. coli* cell. The thin black line represents the continuous trajectory of a cell. Crosses and circles stand for running and tumbling phases, respectively and locate the registered positions for a cell along the trajectory. The dashed lines are the prosecution of the displacements $\mathbf{d}_t$ and help to visualize the turning angle θ_t. Modified from [118].

5.2.2 Resew segmented trajectories

Individual *E. coli* bacteria can become temporarily lost swimming freely in 3D space, or because of bacterial cells overlap or collide, trajectories may end abrubtly. Moreover this effect rise up when the density of bacteria increase, reducing the average length of a trajectory reconstructed with the algortithm described in the previous Section. But sometimes many short trajectories do not contain the same information of less long ones. If we are not just interested in population averages, but we want to know some single cell information or distinguish cells between motile and non-motile, to follow a bacteria for longer time is necessary. Thus a challenging issue that we want to tackle is resewing incomplete trajectories. Here we describe an approach for reconstruct the long trajectories using the informations extracted from the short ones. In our algorithm can happen that for the frames between t and $t + dt$ a bacterium is not detected, but at time $t + dt$ it appears again among the list of centroids. To resew these two trajectory segments we evaluate for each possible connection between the end E_i of a trajectory and the beginning of another B_j a cost function $C(E_i, B_j)$, where i is an index that run on the end of all trajectories while j on the beginning. We define $\langle a_{ij} \rangle = \frac{\omega_i \bar{a_i} + \omega_j \bar{a_j}}{(\omega_i + \omega_j)}$ as the weighted average with weight ω_i the square root of the number of points n_i composing the i-th trajectory. We use this weights as an error estimation of the variable $\bar{a_i}$. We can then write C_{ij} as the linear combination of three terms:

- $c_r(i,j) = \begin{cases} r_{ij}, & \text{if } 0 < \frac{r_{ij}}{dt_{ij}} < v_{\max} \\ \infty, & \text{otherwise} \end{cases}$

where $r_{ij} = \sqrt{(x_i - x_j) + (y_i - y_j)}$ is spatial distance, dt_{ij} is the temporal distance between the end of a trajectory and the beginning of another, and $v_{\max}$ set an experimental threshold to the maximum speed of bacteria

- $c_v(i,j) = \frac{|\bar{v_i} - \bar{v_j}|}{\langle v_{ij} \rangle}$, the relative variation of the bacterial speed measured in the two trajectories
- $c_\lambda(i,j) = \frac{|\bar{l_i} - \bar{l_j}|}{\langle l_{ij} \rangle}$, the relative variation of the bacterial length measured in the two trajectories

Since if we want to connect two short trajectories we cannot trust the estimation for the speed $\bar{v}$, while if dt_{ij} is a long interval it is more probable that another bacterium could be arrived where the final centroid of the i-th trajectory was and thus we the distance term $c_r(i,j)$ is less trustable. For these reasons we define three weights depending on the trajectories i-th and j-th to combine the three c terms:

- $\alpha_{ij} = \begin{cases} \frac{1}{3}\frac{2dt_{\max} - dt_{ij}}{2dt_{\max}} & , \text{ if } dt_{ij} < dt_{\max} \\ \infty & , \text{ otherwise} \end{cases}$
- $\beta_{ij} = \frac{1}{3}\frac{z}{z + \Delta n_{\max}}$,
  where $z = \frac{2n_i n_j}{n_i + n_j}$ and $\Delta n_{\max}$ is equal to number of frames corresponding to $dt_{\max}$. Longer are the trajectories, greater this the weight.
- $\gamma_{ij} = 1 - \alpha_{ij} - \beta_{ij}$

Finally we can write the cost function as:

$$C(i,j) = \alpha_{ij} c_r(i,j) + \beta_{ij} c_v(i,j) + \gamma_{ij} c_\lambda(i,j)$$

For each frame at time t we evaluate this function between the trajectories ended in t and those that started in the interval $(t, t + dt_{\max}]$. We find the couple (i,j) that minimize $C(i,j)$ assigning j-th trajectory as the prosecution of the i-th. Then we delete this two trajectories from the list of ended trajectories (E) and from the list of started trajectories (B). In this way we could reconstruct many of the segmented trajectories with a limited number of mistakes that we can later correct with a Python GUI that let to visualize the proposed couplings.

5.2.3 Method to distinguish motile and non-motile bacteria

Evaluation of the scaling law of the MSD at different time could be a good way to distinguish these two types of motion: ballistic, relative to "active" swimmers and a random one, relative to "passive" swimmers. Unfortunately when we have to manage experimental trajectories the estimation of the MSD is not always enough. The

trajectory has to contain at least some reorientation phases such that the mean is a good estimation for the MSD. Here we propose a method developed starting from an approach precedently proposed in [120] that use two parameters to separate this two cases. The first parameter $|\bar{\theta}|$, is related to reorientations and it is the mean of the absolute angle between two successive displacement (Fig. 5.2). This parameter would be $|\bar{\theta}| = 0$ for a perfectly straight trajectory, while for a purely Brownian particle it is $|\bar{\theta}| = \pi/2$. The second parameter, related to the minimal circle diameter L that include an entire trajectory of duration T, is $N_c = \frac{L}{T}\frac{1}{\bar{v}}$. N_c is close to 1 for straight trajectories while for diffusive motion it goes to zero increasing T. If we assign to each track a point in the (N_c,$|\bar{\theta}|$) parameter space we see a bimodal distribution for the bacterial trajectories. One for N_c close to 1 and small $|\bar{\theta}|$ representing "active" swimmers and one for low N_c and high $|\bar{\theta}|$ describing "passive" swimmers. This method seems a good way to distinguish between this two characteristic motion, but when we look at longer trajectories the swimming behavior of *E. coli* cells can be seen as a diffusive process with an enhanced diffusion coefficient $D_{active} = v^2\tau$ [121] and then some of the "swimmers" can be detected for small N_c creating ambiguity. To avoid this we divide the trajectory into segments of duration τ, we estimate N_c in each track segments and we take just the maximum value among these to characterize the trajectory.

5.3 Dynamic Image Correlation Spectroscopy (DICS)

Traditionally microscopy is a direct access to real space images, where trajectories of particles can be reconstructed using tracking procedures. But tracking is laborious, and the need for averaging over many data sets to achieve high accuracy restricts the scope for time-dependent measurements. Dynamic Image Correlation Spectroscopy (DICS), just like Differential Dynamics Microscopy (DDM) [122], is a method inherited by Dynamics Light Scattering (DLS) the traditional technique applied to study colloidal dynamics. All these technique are based on tools of Fourier optics, and on the measurement of the normalized intermediate scattering function (ISF). Assuming a model to describe the dynamics of the particle in the sample DICS can characterize an ensemble of particles looking at the local temporal fluctuations of a microscopy video over different length scale analysis. Fluctuation of an image is related to fluctuations in the density of the particles. This technique can be applied to statistically characterize dynamics of biological samples in conditions where images contain tens of thousands of particles and a tracking procedure is unfeasible [123, 78, 80, 124, 125]. Using this technique we can extract informations on the fraction of motile bacteria, average and standard deviation of their swimming

speed distribution and the thermal diffusion coefficient indicated as α, v, σ and D, respectively.

First of all to perform DICS we compute the image correlation function:

$$g(\mathbf{q}, t', t) = \langle \bar{I}(\mathbf{q}, t') I(\mathbf{q}, t' + t) \rangle$$

where $I^*(\mathbf{q}, t)$ is the spatial Fourier transform of the image $I(\mathbf{r}, t)$ at the wave-vector $\mathbf{q}$ and the bar stand for complex conjugate. Assuming that during the recording the sample can be considered in a stationary regime $g(\mathbf{q}, t', t)$ does not depend on the time origin t' and we can use just its average $g(\mathbf{q}, t) = \frac{1}{T} \int_0^T g(\mathbf{q}, t', t) dt'$. Moreover if there are no anisotropies in the bacterial movement we can average over all $\mathbf{q}$-vectors with the same magnitude ($|\mathbf{q}| = q$) so we can write $g(q, t) = \int_{-\infty}^{\infty} g(\mathbf{q}, t) \delta(|\mathbf{q}| - q) d\mathbf{q}$. In the regime where multiple-scattering from the particles can be neglected the $g(q, t)$ is connected to the ISF $F(q, t)$:

$$g(q, t) = A(q) F(q, t) + B(q)$$

where $A(q)$ and $B(q)$ are time-independent factors related, respectively, to the number and shape of bacteria, and to the background noise in the images. In the low dilution approximation, the particle trajectories are independent and we can write ISF as $F(q, t) = \frac{1}{N} \sum_{j=1}^{N} \langle exp[i\mathbf{q}(\mathbf{r}_j(t) - \mathbf{r}_j(0))] \rangle$, with $\mathbf{r}_j(0)$ as the position of the j-th cell at time t, and N cells appearing in the field of view.

Now we have to assume a model to describe the dynamical behavior of the cells. Different models have been developed to analytically describe the ISF [126] [127] [128]. To describe a sample of *E. coli* (both wild type and smooth swimmer strains) we assume that the system is composed of a mixture of two kind of isotropic particles, passive swimmers and active swimmers moving along straight trajectories [80] [124]. Then the ISF is:

$$F(q, t) = (1 - \alpha) e^{-q^2 D t} + \alpha e^{-q^2 D t} \int_0^{\infty} P(v) \frac{\sin(qvt)}{qvt} dv$$

However here the distribution of speeds among a the population $P(v)$ is not known. Previouos studies modeled swimming speed dispersion in bacterial motility as a Schultz distribution (or generalized exponential) [80, 129],

$$P(v) = \frac{v^Z}{Z!} \left(\frac{Z + 1}{\bar{v}}\right)^{Z+1} exp\left[-\frac{v}{\bar{v}}(Z + 1)\right]$$

where the relation $\sigma = \bar{v}(Z + 1)^{-1/2}$ connect Z to the variance σ^2 of the distribution.

Assuming the $P(v)$ in Eq. 5.3, we can compute the integral in Eq. 5.3 as in [130]:

$$\int_0^\infty P(v)\frac{\sin(qvt)}{qvt}dv = (\frac{Z+1}{Zq\bar{v}t})\frac{(\sin(Z\tan^{-1}\Lambda)}{(1+\Lambda^2)^{Z/2}}$$

where $\Lambda = q\bar{v}t/(Z+1)$. To extracting the data of swimming bacteria in 3D we have to choose at the q-range where the $F(q,t)$ capture their dynamics. The upper bound for the analysis is given by the amplitude of the wobble of a bacterium $\sim 2\mu m$. We do not want that this component contributes to the ISF thus we choose $q < \frac{2\pi}{2\mu m} \sim 3\ \mu m^{-1}$. While the lower bound can be assumed to be the the path length of a bacterium before a fluctuation in the orientation (*i.e.* tumbling or rotational diffusion) deviate it from a straight line $\sim 20\ \mu m$ [21]. This set $q > \frac{2\pi}{20\mu m} \sim 0.3\ \mu m^{-1}$. Compatibly with the constraints mentioned above in our analysis we restrict to $0.45\ \mu m^{-1} < q < 1.2\ \mu m^{-1}$.

The measured ISF can be fitted with the model described above thus extracting the parameters α, v, σ, D. Differently from previous works [80] [124] where the curves are fitted at each q separately at averaged at the end, we fit all the curves at different q with the same parameters thus one single value for α, v, σ, D is extracted. Since, all parameters obtained using the method in literature describe the same phenomenon, our method seems to us more reasonable than averaging those obtained at different q *a posteriori*. Figure 5.3 shows reconstructed ISF for an HLK sample. Data are well fitted by the described model. Furthermore the validity of the model is confirmed by the good collapse of the curves predicted by Eq. 5.3. Rescaling the time axis $t \to qt$ the curves collapse for small values (fast scale characterizing active motion), while rescaling $t \to q^2 t$ we can capture the diffusion process.

5.4 Microstructures

We used the software described above to study motility of cells in different shaped microstructured environment able to confine bacteria in pseudo-2D geometries helping the tracking procedure. This structures have been microfabricated using a two-photon polymerization technique described in Section 5.1. During my PhD we worked with three different structure designs to study different aspect of the *E. coli* swimming behavior (*i.e.* swimming behavior, collective motion, .

5.4.1 The swimming pool

The swimming pool has a design projected to confine *E. coli* in a quasi-2D space, and to collect swimming cells taking advantage of their peculiar interactions with bounding wall. It is composed of a hexagonal wall with six passages coupled to

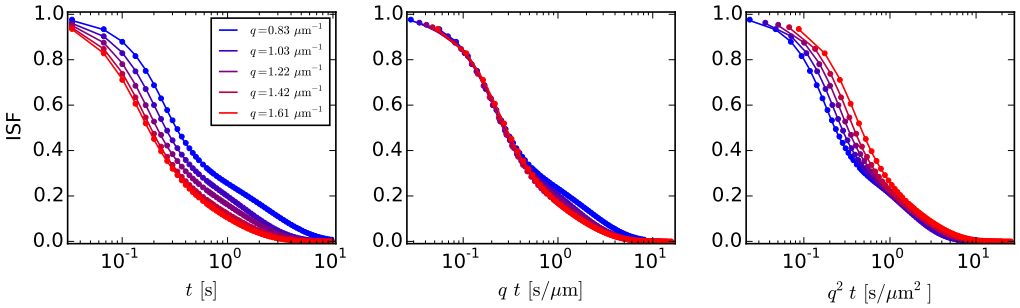

Figure 5.3. Intermediate Scattering Functions. (Left) Reconstructed ISFs of an HLK sample powered by light at different q. Circle represents the measured data at different q. The solid lines represent one global fit of data at all the q contemporary. Here we show that the ISF captures two regimes of the swimming behavior of *E. coli* cells. **(Center)** We see that rescaling $t \to qt$ the curves collapse in the left part of the graph characterized by the ballistic regime. **(Right)** The diffusive regime is captured at longer times where the curves collapse rescaling $t \to q^2 t$.

funnels and a thick roof of $\sim$ 6 µm above it (Fig. 5.4). To avoid the collapse of the roof on the structure we added some columns that fix the internal height at $\sim$ 1.4 µm.

E. coli swimming at solid surfaces is characterized by clockwise circular trajectories [131]. The hydrodynamic interactions of the cell body and flagella bundle rotating in opposite direction combined with the no slip condition surface generate a net torque on the bacterium inducing this effect [132]. But internally the height of chamber is less than two bacterial width. This tight geometry suppress this peculiar swimming pattern and thus we observe cell swimming straight in this chamber, such as in [91]. Moreover cells in this geometry cannot overlap and this introduce more frequent steric interactions between cells increasing reorientation of cell bodies caused by collision and allignment.

It was already demonstrated that wall geometries can be used to direct bacteria inside microfluidic devices [133, 9], we use two different components to collect motile bacteria inside the swimming pool. The outside funnels, together with the external curved walls, direct bacteria inside the structure. While the internal curved walls redirect the bacteria towards the center thus to reduce their probabilities of escaping. This design is really efficient in collecting bacteria (Fig. 5.5); slightly increasing the sample density and waiting for less than one hour we observe particle close packing inside this structure. As future project we look forward to use this structure to study high density 2D confined population. The collected population of bacteria will be imprisoned in the microstructure for long intervals with a persistent activity substained by the continuous flow of nutrients and oxygen from outside through the apertures. This microstructure let us to repeatedly study the individual light

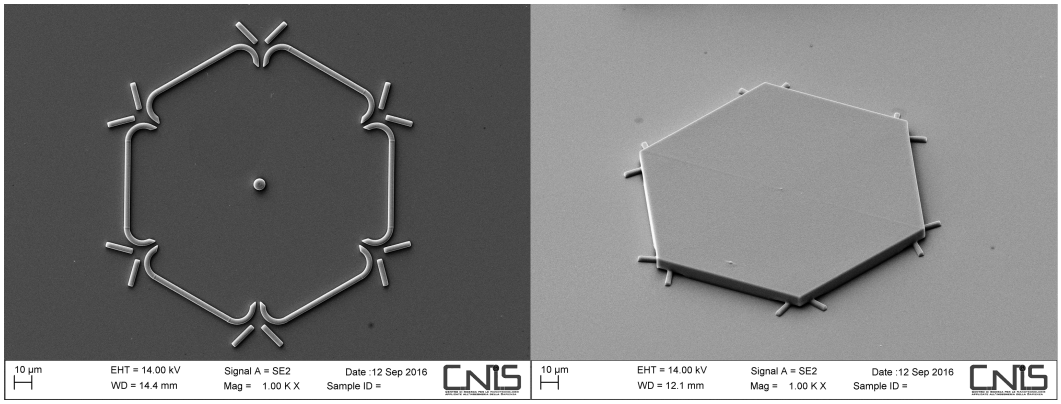

Figure 5.4. The swimming pool. Scanning electron microscopy (SEM) pictures of the "swimming pool" microstructure, a microfluidic device designed to accumulate motile bacteria exploiting their tendency to swim along walls and confine them in a pseudo-2D geometry. **(Left)** Bird's eye view of the structure taken the roof off. **(Right)** Side view of the entire microstructure to emphasize the small gap height between the glass and the roof (*sim* 1.4 µm).

responses of bacteria over several hours.
The roof, as well as a confinement in 2D, avoids the sedimentation of non-motile cells from above and the detection of cells outside the structure.

5.4.2 Microtunnels

The majority of motile bacteria propel themselves by a rotating helical flagellar bundle, typically with a speed of ten body lengths per second. Motility of such organisms is preserved even in confining micro-environments which constitute their typical habitat. The analysis of low Reynolds-number hydrodynamics shows that drag forces increase significantly in such geometries [19]. Quantitative experimental studies so far were limited to observe distinct suspensions of bacteria in 2D confinement [134, 135] or in large diameter microcapillaries.

We designed a microstructure that guide *E. coli* cells through a series of eight square-section microtunnels, with sides ranging from 1.4 to 3.8 µm. At the entrance of the structure there is a funnel to increase the probability of to have cells entering the structure (Fig. 5.6). Combining this device with the fluorescent smooth swimmer HCB437 mRFP1+ (Chapter 4), we studied, at the single cell level, the influence of strict confinement on the swimming parameter. We observed cells swimming in tight 1D confinement slightly modifying their speeds despite the big increase in the hydrodynamic drag on the cell. Thanks to our tracking software we reconstruct about 100 trajectories of cells swimming in each microchannel without being affected by the interaction with other cells. Along each trajectory we measured a series of properties, namely: swimming speed, cell-body size, wobbling amplitude and frequency, and

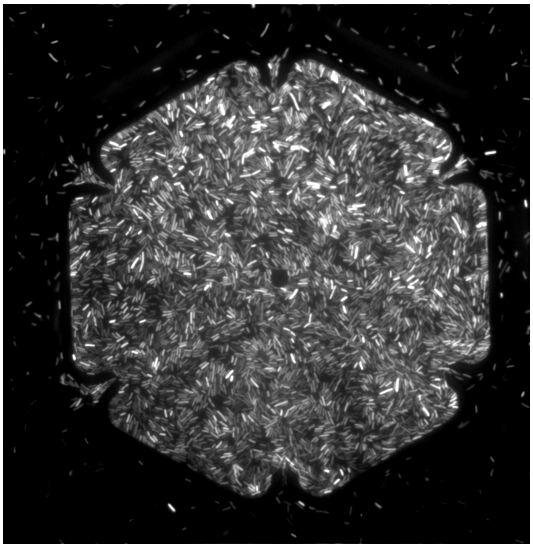

Figure 5.5. Bacteria in the swimming pool. Epifluorescence microscopy picture of a population of HCB437 expressing an mRFP. Bacteria are confined into "the swimming pool", a microfluidic device that let to obtain extremely dense suspension.

bulk swimming speed. We observed two interesting phenomena: (i) we observed that an optimal channel diameter for which the increases in flagellar thrust due to 1D confinement overcomes the increased drag on the cell body, resulting in swimming speeds that can be up to 15% with respect to the bulk speed (Fig. 5.7) (ii) Cells exiting a confined structure have their speed increased temporarily (Fig. 5.8).

5.4.3 Path invariance chamber

In 2003 Blanco and Fournier stated a theorem presenting a counterintuitive results about the mean length $\langle L \rangle$ of random walker's trajectories in a domain [136]: such mean value depend only on the ratio of the volume's domain over its surface. Not any property of the random walk influences $\langle L \rangle$, under the assumption that random walkers enter isotropically the domain. In biology random walks have been often used to model the movement of animals, bacteria and cells [137]. Simple stochastic rules can be used to estimate average properties of swimming *E. coli* cells [79]. We are exploring the possibility to verify the 2D-version of this random walk invariance property for swimming bacteria. The use of a phototactic *E. coli* to dynamical regulate the parameters of the random motion would be perfect. However we were not able to obtain a strain with this control. An alternative is to use a structured environment to tune the frequency of reorentation. Then, we designed and fabricated a series of microstructure presenting randomly distributed pillars, with $\sim$ *E. coli* size, covered by a roof. This structure constraints the bacteria to swim on a plane thus facilitating the tracking procedure. We observed fluorescent

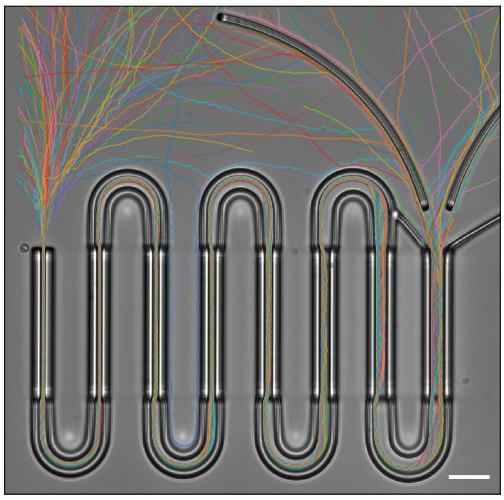

Figure 5.6. Microtunnels. Bright-field image of the microstructure guiding cells through eight different square-section channel ($1.4 - 3.8$ µm). The trajectories of 100 *E. coli* cells are superimposed on the image. The scale bar is 10 µm.

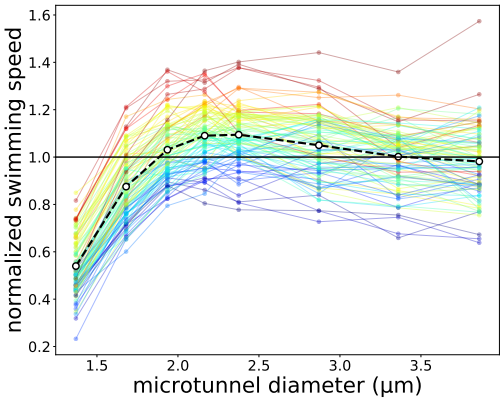

Figure 5.7. Faster in confinement. Swimming speed of cells in confining microtunnels of different section. The speeds are normalized respect to the bulk speeds. Black circles represent the averages over 100 tracks.

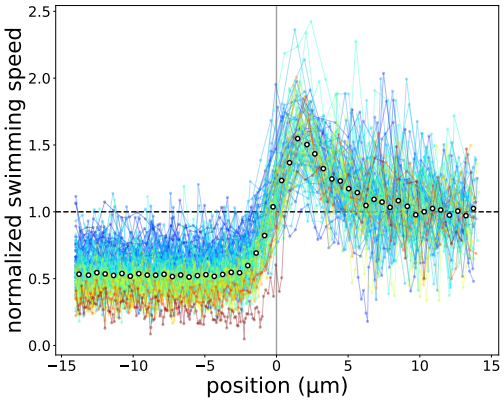

Figure 5.8. Flagella thrust increases in confinement. Instantaneous swimming speeds of cells exiting the smallest microtunnel normalized to the bulk speed. The gray vertical line marks the position where the center of a tracked cell body is exactly at the exit of the microtunnel. Cells exiting a narrow channel have their speed increased since the flagellum is still confined.

bacteria swimming among obstacles of different shapes (*i.e.* lines, circles, triangle) to study which geometrical form could maximize the reorentation range that we could obtain (Fig. 5.9) and we found that the line would be the optimal shape (data not shown). We are continuing to work experimenting different density of obstacles. The preliminary results on the theorem verification are promising.

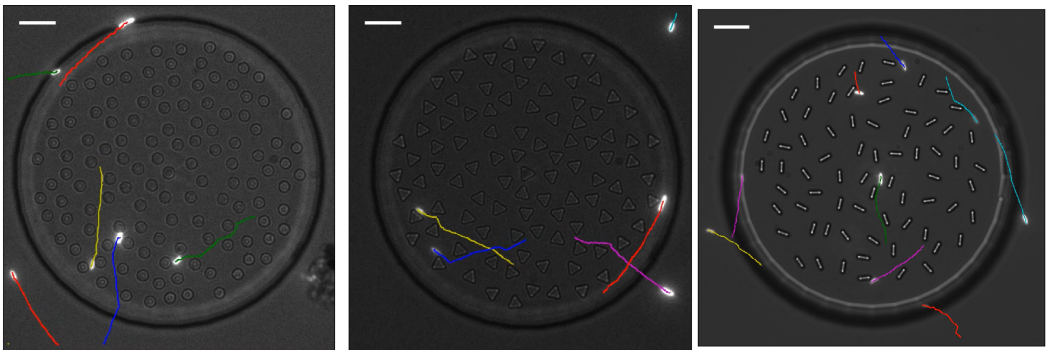

Figure 5.9. 2D confinement with obstacles. Fluorescent *E. coli* swims in the a structured environment defined with obstacles of different shape (circle, triangle, lines). The images are obtained superimposing bright field images of the structures, epi-fluorescent images of the bacteria and the trajectories followed by bacteria (last 2 s). The scale bar is 10 µm.

Chapter 6

Molecular Biology

6.1 Bacterial Growth

Bacteria are among the first life forms appeared on Earth and they developed the ability to grow in many different environments. *E. coli* bacterium too is able to live in a wide range of substrates such as food, water and gut. Since environmental growth conditions can strongly affect bacterial motility [138], different growth media or different temperature should be used for laboratory studies, depending on the desired output.

Bacterial growth in liquid medium is the most common way of culturing bacteria, given the sheer numbers and ease of harvesting. Typically this culture method begins from a single, well-isolated colony, picked from an agar plate, such to reduce bacterial culture variability. This colony is inoculated into a fresh medium. Looking at the growth rate dynamics in the culture, four different growth phases can be identified (Fig. 6.1):

1. **Lag phase:** a period during which cells do not grow but they produce all the molecular machineries needed to grow in their new environment.

2. **Log phase:** bacterial cell number increases exponentially, through the binary fission of each single cell, in a typical time range from 20 minutes to 1 hour depending on the growth conditions. This phase carries on until the decreasing energy yield of nutrients in the medium can no longer sustain the growth.

3. **Stationary phase:** the cell number remains constant, as a result from a situation in which growth rate and death rate are equal. However after some time this balance breaks.

4. **Death phase:** in the long term, in absence of nutrients, cells stop their duplication and the number of live cells decreases.

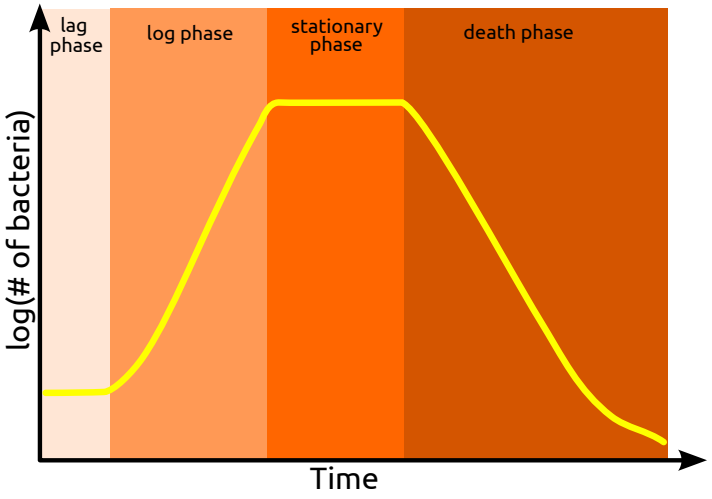

Figure 6.1. Bacterial growth curve. During bacterial growth in batch culture we can distinguish four different phases. See the main text for the description of individual phases

To reduce the chance of growing contaminants and unwanted mutants together with the desired strain, the growth medium must be always supplemented with antibiotics, to which the strain is resistant. Among the most used growth media for motility experiments, we recall: tryptone broth (TB), Luria-Bertani broth (LB) and M9 minimal medium (M9). The energy yield of nutrients of this different media can influence the growth rate and the reachable density at the stationary phase, which can be measure from the optical density (OD). Figure 6.2 shows the measured OD_{590} (where 590 stands for the wavelength (nm) of the spectrophotometer light) for HCB437 PR^+ bacteria grown in four different conditions. The optical density, in the low density regime, is proportional to the bacterial concentration in the medium. At higher density, multi-scattering breaks this linear relation, therefore the culture must be diluted to obtain a reliable estimate before the OD measurement.

Hereon we present a general protocol to prepare *E. coli* for motility experiments:

1. From the frozen stock (-80 °C), we strike a Petri dish with the strain bacterial strain

2. The dish is kept at 33 °C in the incubator for one night

3. A single colony, grown on the dish, is picked with a sterile metal loop and inoculated in 10 mL of liquid growth medium contained in a Falcon tube, than grown overnight at 33 °C. The dish is stored at 4 °Cfor later uses.

4. In the morning the culture has reached the saturation phase. A 1:100 dilution is prepared in a new fresh medium. This step should partially synchronize the cell cycle such to reduce the population variability. The diluted culture is grown at 33 °C in a shaking incubator ($\sim$ 100-200 rpm)

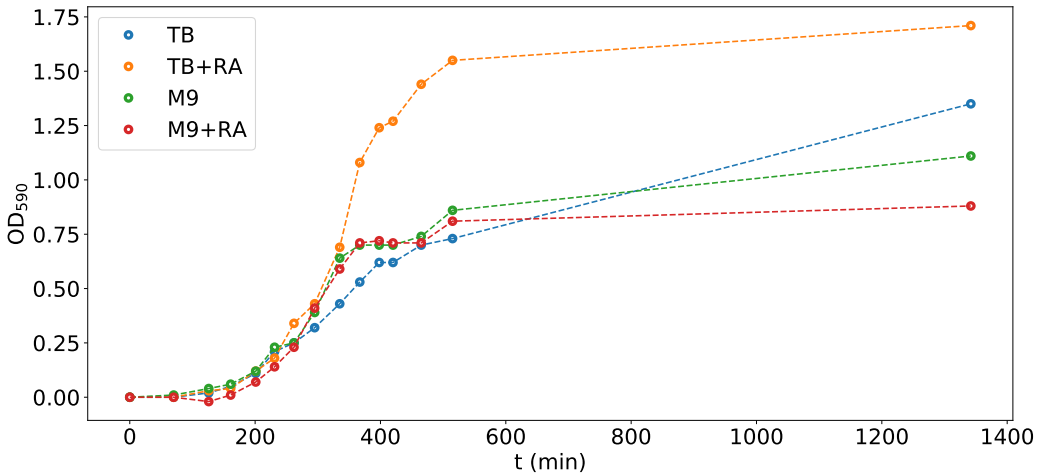

Figure 6.2. HCB437 PR$^+$ growth curve. This plot shows the ODs of a bacterial suspension of the strain HCB437 PR$^+$ in four different growth environments. TB, TB+RA, M9, M9+RA. The suffix +RA stands for the addition of 20 µM *all-trans*-retinal, the PR's chromophore, to the medium

5. The OD_{590} of the growing culture is measured to check the bacterial growth phase.

6. Once cells have reaches late-exponential phase, they are harvested. The growth medium is replaced with a motility buffer (10 mM potassium phosphate (pH 7.0), 0.1 mM EDTA (pH 7.0), and 0.2% Tween20) [138] through three centrifugations.

6.2 Plasmid Transformation

A plasmid is a circular double-stranded DNA molecule that is distinct from the chromosomal DNA and it is small compared to it. Plasmids are commonly found in bacteria and usually they carry genes that provide genetic advantages (e.g. antibiotic resistance). The chromosomal DNA is not the only one copied during bacterial duplication, but also at least one copy of each plasmids is inherited by the daughter cells. However if plasmids do not bring some genetic advantage, they can be either expelled or not replicated during duplication. Plasmids can be introduced into a bacterium through its membranes by way of a transformation process. Once inside the cell, plasmids can be exponentially replicated, codify for protein or be used to manipulate genes. However not all the bacteria can naturally accept exogenous DNA: only competent cells are indeed capable of this insertion. Competent cells can be prepared artificially using chemicals or electrical pulses. These processes alter the cell wall thus to make it permeable to DNA. We present below two different

protocols followed to obtain the transformation. These protocols are divided into two parts: first, there is an explanation on how to prepare competent cells; the second part contains how to transform the prepared cells with a plasmid. The first protocol allows for obtaining a more efficient transformation but requires a longer time. This kind of experiments results successful in the end if also just one single transformed colony growth on the agar plate.

Transformation: chemically competent cells

- **Preparation of chemically competent cells**

  1. Grow overnight 3 mL of cell culture in LB medium at 30 ℃ in a shaking incubator (200 rpm)
  2. In the morning, dilute this culture back (200x) into 100 mL of fresh medium:
     - 100 mL of LB
     - 1 mL of 1 M $MgCl_2$
     - 1 mL of 1 M $MgSO_4$
     - 500 µL of *E. coli*
  3. Grow the diluted culture for ≈ 3 h at 30 ℃, until the culture reaches $OD_{600} \approx 0.3$ - 0.4
  4. Incubate 10 mL of this culture in a centrifuge tube on ice for 10 minutes
  5. Put 4 Eppendorf tubes on ice, so that they are cold when cells are aliquoted into them later
  6. Centrifuge for 10 minutes at 2500 g and 4 ℃
  7. Remove supernatant. Re-suspend the pellet in 1 mL chilled Transformation Buffer solution (4 ℃)
     Transformation Buffer preparation (100 mL):
     - 10 mM PIPES
     - 15 mM $CaCl_2$
     - 250 mM KCl in 80 mL distilled water

     Set the pH at 6.7 using 5N KOH. Add 55 mM $MnCl_2$ in 10 mL solution and complete the solution to 100 mL with distilled water. After filter sterilization, store at 4 ℃
  8. Incubate on ice for 10 min
  9. Centrifuge for 10 minutes at 2500 g and 4 ℃
  10. Remove supernatant. Resuspend the pellet in 362.5 µL Transformation Buffer solution + 37.5 µL DMSO

11. Add 100 µL aliquots to your chilled Eppendorffs and store at -80 ℃

- **Heat shock transformation**

1. Let defrost the chemically competent cells in ice from -80 ℃
2. Add ≈1 ng of plasmid DNA diluted in 1 µL ddH_2O
3. Keep in ice for 10 min
4. Put for 2 min the cells at 42 ℃ or 3 min at 37 ℃ (heat shock)
5. Add 1 mL SOC to the Eppendorf
6. Incubate 37 ℃ for 40 min
7. Plate 100 µL of the transformation on selective plates
8. Centrifuge for 1 min at 13.000 rpm
9. Carefully remove the supernatant leaving 100 µL of it, in which the cells are resuspended
10. Plate the cells on selective plates
11. Let the colonies grow overnight 37 ℃

Colonies that grow on the selective plate are successfully transformed with the plasmid

Transformation: electro-competent cells

- **Electro-competent cell preparation**

1. Grow overnight 3 mL of cell culture in LB medium at 30 ℃ into a shaking incubator (200 rpm)
2. In the morning, make a dilution of the overnight culture in 50 mL of LB growth medium
3. Grow the diluted culture for ≈ 4 h at 30 ℃, until the culture reaches OD_{600} ≈ 0.3 - 0.4
4. Centrifuge the grown culture at 4000 rpm for 10 min. Discard the supernatant and re-suspend in the same amount of filter glycerol 10
5. Repeat 3 times the previous step reducing by half the amount of glycerol added (25 mL, 15 mL, 5 mL)
6. Centrifuge and re-suspend in 180 µL of glycerol and rest in ice for 10 min

- **Electroporation**

1. Add at least 1 ng of DNA to 90 µL of cells and use the rest as negative control (without DNA)

2. Rest in ice for 10 min
3. Add the competent cells to a pre-cooled electroporation cuvette 0.1 mm
4. Electroporate using this parameters: 2.5V, 200 ohm, 25 µF
5. After electroporation immediately add 1 mL of SOC growth medium to the cuvette. And place everything in a 2 mL eppendorf.
6. Place 2 minutes in ice.
7. Incubate at 37 ℃ for one hour
8. Plate 100 µL of transformed cell on a Petri dish
9. Let the colonies growth overnight at 37 ℃

6.3 PCR

Polymerase chain reaction (PCR) is a technique used in molecular biology to amplify a segment of DNA across several orders of magnitude, generating thousands to millions of copies of a particular DNA sequence. PCR methods rely on thermal cycling, which involves exposing the reactants to cycles of repeated heating and cooling, permitting different temperature-dependent reactions-specifically, DNA melting and enzyme-driven DNA replication—to quickly proceed many times in sequence. Primers (short DNA fragments) containing sequences complementary to the target region, along with a DNA polymerase, after which the method is named, enable selective and repeated amplification. As PCR progresses, the DNA generated is itself used as a template for replication, setting in motion a chain reaction in which the original DNA template is exponentially amplified.

PCR applications employ a heat-stable DNA polymerase, such as Taq polymerase, an enzyme originally isolated from the thermophilic bacterium *Thermus aquaticus*. This DNA polymerase enzymatically assembles a new DNA strand from free nucleotides, the building blocks of DNA, by using single-stranded DNA as a template and DNA oligonucleotides (the primers mentioned above) to initiate DNA synthesis.

In the first step, the two strands of the DNA double helix are physically separated at a high temperature in a process called DNA melting. In the second step, the temperature is lowered and the two separated DNA strands become templates for DNA polymerase to selectively amplify the target DNA. The selectivity of PCR results from the use of primers (*i.e.* short single strand nucleotide sequences) that are complementary to the extremes of the DNA region targeted for amplification under specific thermal cycling conditions.

Protocol:

1. PCR Buffer preparation: We used different PCR kits to obtain the PCR Buffer. Each kit depends upon a specific protocol but each requires:
   - DNA template
   - the two primers
   - deoxynucleoside triphosphates (dNTP)
   - Taq polymerase
   - reaction buffer
2. Thermocycler:
   (a) Initialization: 98 °C for 1 min
   (b) Central Loop of the PCR that must repeated between 25-35 depending of the quantity of DNA requested:
      - Denaturation: 98 °C for 1 min
      - Annealing: 56 °C for 1 min
      - Extension/Elongation:72 °C for the time needed to the Taq to complete the trascription of the desired segment of DNA (the time and temperature of this step depend on which Taq is used and the length of the DNA segment you want to copy)
   (c) Final Elongation: To be sure that all the Taq that have already started the trascription complete their template copying: 72 °C for 2 min
   (d) Final hold: The final step cools the reaction chamber to 4-15 °C for an indefinite time, and may be employed for short-term storage of the PCR products.
3. PCR product purification using a specific kit
4. Control using electrophoresis on an agar gel to check if the double strand DNA obtained results of the length expected

6.4 Gene editing

This method is used to delete/inactivate *E. coli* chromosomal genes and it is adapted from Datsenko & Wanner [139]. The knocked-out gene is replaced with an antibiotic resistance gene.

The protocol for this method include the use of two plasmids:

- **pKD46:** pKD46 carries the λ red recombinase genes behind the araBAD promoter and it is temperature sensitive (grow at $\leq$ 32 ℃ to maintain the plasmid, while at higher temperature is not replicated). It contains an ampicillin resistance.

- **pKD4:** kanamycin resistance cassette. The resistance cassette is flanked by FRT sites, which allow the removal of the cassettes once inserted in the bacterial chromosome with a FLP helper plasmid. This plasmid will be only used during PCR together with specifically designed primers that will amplify this cassette. The aim is to obtain many copies of a KAN cassette that will be then used to replace the gene we want to delete.

Procedure:

- Recombinase expression in the desired strain

  1. pkD46 amplification and purification: Miniprep
  2. pkD46 transformed into the desired strain (ref. 6.2)

- Resistance Cassette preparation

  1. Primer Design containing in the sequence a DNA segment of pkD4 and a DNA segment neighboring the targeted gene
  2. pkD4 amplification: Miniprep using a standard kit
  3. pKD4 + homology sequence: PCR (ref. 6.3)

- Recombination of the resistance cassette in the desired strain

  1. Grow overnight the desired strain + pkD46 in LB medium
  2. In the morning, make a dilution 1/100 of the overnight culture in 50 mL of LB growth medium with antibiotics and arabinose as inductor 0.2% (to express the λ-red recombinase system), till an OD_{600} of 0.4-0.6
  3. Prepare electro-competent cells (ref. 6.2) and transform them with the amplified resistance cassette
  4. Growth: Grow the mutated strain in SOC medium in an oscillating incubator at 37 ℃ to be sure that the thermo-sensitive plasmid pkD46 is expelled

- Phenotypic control: If possible, as in the case of a mutation that affects motility of the bacteria, you can look at them under the microscope to verify if the predicted result has been obtained

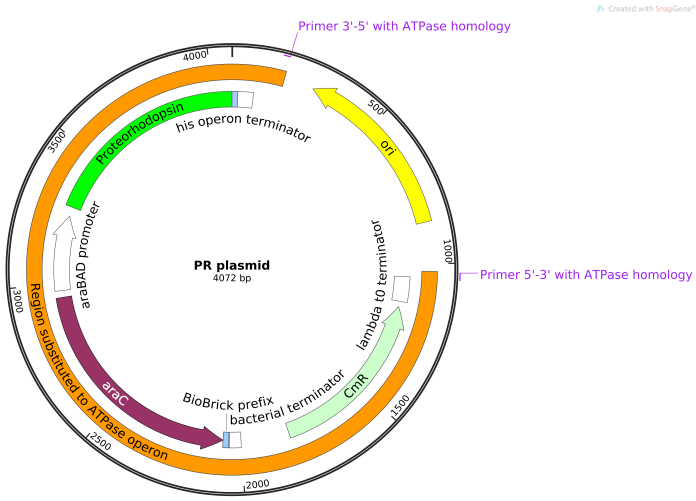

Figure 6.3. Map of the plasmid codifying the proteorhodopsin. The orange region represents the segment of DNA that we substitued to the ATPase operon. At the extrema of this region, the segments where the primers attach to the DNA, thus to initiate the duplication.

- PCR product verification: To be sure that the cassette insertion happened in the right position, design two primer at the extrema of a region that should contain the inserted cassette. Run a PCR with these primers on the chromosomal DNA extracted from the mutated strain. Using electrophoresis, compare the length of the DNA segments amplified with PCR with the expected length.

To obtain the strain HLK (HCB437 PR+ Δatp), we substitute a set of genes with a new one, rather than just delete it. We do not use the classical pkD4 with the KAN, we use instead the plasmid containining the PR (Fig. 6.3) and a CAM cassette to copy the region of DNA to insert. In this way we obtain a deletion and an insertion in one single step. Both the designed primers are optimized for our purpose of assembling together a segment of the DNA found at one extreme of the ATPase operon and a segment of the plasmid template containing the PR. Many rules have to be taken into account in this procedure like that DNA replication can proceed just in one direction on the DNA molecule (5'$\rightarrow$ 3'). At this url it is possible to find a summary of them. The primer sequences obtained are given in Table 6.1.

Name	Nucleotide sequence
ATPsynthKO FW	5'-ATG GCG ATC GCT TTG GCC AGT TCC GCA GAC GCC TGA GCG TAA TCT ACG TCG CCA CAG CTC GAG GCT TGG ATT C-3'
ATPsynthKO RV	5'-TGA CGG CAT ACC TCG AAG GGA GCA GGA GTG AAA AAC GTG ATG TCT GTG TCG CTA TTA CCG CCT TTG AGT GAG C-3'
ATPsynthKO-check FW	5'-CCA TCG TCA CGC CTT TTG TC-3'
ATPsynthKO-check RV	5'-GGG TTA GCA GAA AAG TCG CA-3'

Table 6.1. Nucleotide sequences of the primers used to obtain the HLK strain from HCB437 and the plasmid composed of the backbone pSB1C3 (the standard cloning vector for iGEM parts), and the part BBa_K1604010 codifying the proteorhodopsin under an arabinose inducible promoter.

Bibliography

[1] Zachary D Blount. The unexhausted potential of E. coli. *Elife*, 4:1–12, 2015. v

[2] Erika Check Hayden. Synthetic-biology firms shift focus. *Nature*, 505(7485):598–598, jan 2014. v

[3] Ahmad S Khalil and James J Collins. Synthetic biology: applications come of age. *Nat. Rev. Genet.*, 11(5):367–379, may 2010. v

[4] Daniel G Gibson, John I Glass, Carole Lartigue, Vladimir N Noskov, R.-Y. Chuang, Mikkel A Algire, Gwynedd A Benders, Michael G Montague, Li Ma, Monzia M Moodie, Chuck Merryman, Sanjay Vashee, Radha Krishnakumar, Nacyra Assad-Garcia, Cynthia Andrews-Pfannkoch, Evgeniya A Denisova, Lei Young, Z.-Q. Qi, Thomas H Segall-Shapiro, Christopher H Calvey, Prashanth P Parmar, Clyde A Hutchison, Hamilton O Smith, and J Craig Venter. Creation of a Bacterial Cell Controlled by a Chemically Synthesized Genome. *Science (80-.).*, 329(5987):52–56, jul 2010. v

[5] Stephen J. Ebbens and Jonathan R. Howse. In pursuit of propulsion at the nanoscale. *Soft Matter*, 6(4):726, feb 2010. v

[6] W C K Poon. From Clarkia to Escherichia and Janus: the physics of natural and synthetic active colloids. pages 317–386, 2013. v

[7] Jana Schwarz-Linek, Jochen Arlt, Alys Jepson, Angela Dawson, Teun Vissers, Dario Miroli, Teuta Pilizota, Vincent A. Martinez, and Wilson C K Poon. Escherichia coli as a model active colloid: A practical introduction. *Colloids Surfaces B Biointerfaces*, 137:2–16, 2016. v, 15, 43, 44

[8] Sriram Ramaswamy. The Mechanics and Statistics of Active Matter. *Annu. Rev. Condens. Matter Phys.*, 1(1):323–345, aug 2010. v

[9] Peter Galajda, Juan Keymer, Paul Chaikin, and Robert Austin. A wall of funnels concentrates swimming bacteria. *J. Bacteriol.*, 189(23):8704–8707, 2007. v, 60

[10] N Koumakis, A Lepore, C Maggi, and R Di Leonardo. Targeted delivery of colloids by swimming bacteria. *Nat. Commun.*, 4:2588, jan 2013. v

[11] Héctor Matías López, Jérémie Gachelin, Carine Douarche, Harold Auradou, and Eric Clément. Turning Bacteria Suspensions into Superfluids. *Phys. Rev. Lett.*, 115(2), 2015. v

[12] M. C. Marchetti, J. F. Joanny, S. Ramaswamy, T. B. Liverpool, J. Prost, Madan Rao, and R. Aditi Simha. Hydrodynamics of soft active matter. *Rev. Mod. Phys.*, 85(3):1143–1189, 2013. v

[13] Claudio Maggi, Juliane Simmchen, Filippo Saglimbeni, Jaideep Katuri, Michele Dipalo, Francesco De Angelis, Samuel Sanchez, and Roberto Di Leonardo. Self-Assembly of Micromachining Systems Powered by Janus Micromotors. *Small*, 12(4):446–451, jan 2016. vi

[14] Jing Yan, Ming Han, Jie Zhang, Cong Xu, Erik Luijten, and Steve Granick. Reconfiguring active particles by electrostatic imbalance. *Nat. Mater.*, 15(10):1095–1099, jul 2016. vi

[15] J. Palacci, S. Sacanna, A. P. Steinberg, D. J. Pine, and P. M. Chaikin. Living Crystals of Light-Activated Colloidal Surfers. *Science (80-.).*, 339(6122):936–940, 2013. vi, 7

[16] David G Grier. A revolution in optical manipulation. *Nature*, 424(6950):810–6, 2003. vi

[17] Sebastianus a. Goorden, Jacopo Bertolotti, and Allard P. Mosk. Superpixel-based spatial amplitude and phase modulation using a digital micromirror device. *Opt. Express*, 22(15):17999, 2014. vi

[18] E M Purcell. Life at low Reynolds number. *Am. J. Phys.*, 45(19):4–11, 1977. 3

[19] John. Happel and Howard. Brenner. *Low Reynolds number Hydrodynamcis with special applications to particulate media*, volume 1. Springer Netherlands, 1983. 3, 61

[20] Eric Lauga and Thomas R. Powers. The hydrodynamics of swimming microorganisms. 72, 2008. 3

[21] Howard C. Berg. *\emph{E. coli} in motion*. Springer, 2000. 4, 59

[22] Frederick C. (Frederick Carl) Neidhardt, John L. Ingraham, and Moselio. Schaechter. *Physiology of the bacterial cell : a molecular approach*. Sinauer Associates, 1990. 4

[23] Jessica C. Wilks and Joan L. Slonczewski. pH of the cytoplasm and periplasm of Escherichia coli: Rapid measurement by green fluorescent protein fluorimetry. *J. Bacteriol.*, 189(15):5601–5607, 2007. 4

[24] J R Knowles. Enzyme-Catalyzed Phosphoryl Transfer Reactions. *Annu. Rev. Biochem.*, 49(1):877–919, jun 1980. 4

[25] Ruidong Xue, Qi Ma, Matthew a. B. Baker, and Fan Bai. A Delicate Nanoscale Motor Made by Nature-The Bacterial Flagellar Motor. *Adv. Sci.*, 2015. 5

[26] H C Berg and D a Brown. Chemotaxis in Escherichia coli analysed by three-dimensional tracking. *Nature*, 239(5374):500–504, 1972. 5, 10

[27] H C Berg and E M Purcell. Physics of chemoreception. *Biophys. J.*, 20(2):193–219, 1977. 5

[28] P.-G. de Gennes. Chemotaxis: the role of internal delays. *Eur. Biophys. J.*, 33(8):691–693, 2004. 5, 10

[29] Damon a Clark and Lars C Grant. The bacterial chemotactic response reflects. *Pnas*, 102(12), 2005. 5, 10

[30] A. Celani and M. Vergassola. Bacterial strategies for chemotaxis response. *Proc. Natl. Acad. Sci.*, 107(4):1391–1396, 2010. 5

[31] Uri Alon, Laura Camarena, Michael G. Surette, Blaise Aguera Y Arcas, Yi Liu, Stanislas Leibler, and Jeffry B. Stock. Response regulator output in bacterial chemotaxis. *EMBO J.*, 17(15):4238–4248, 1998. 5, 54

[32] Alan J Wolfe, M Patricia Conley, Tina J Kramer, and Howard C Berg. Reconstitution of Signaling in Bacterial Chemotaxis. *J. Bacteriol.*, 169(5):1878–1885, 1987. 6, 15

[33] R. V. S. Uday Bhaskar, Richa Karmakar, Deepti Deepika, Mahesh S. Tirumkudulu, and K. V. Venkatesh. Variation of swimming speed enhances the chemotactic migration of Escherichia coli. *Syst. Synth. Biol.*, 9(3):85–95, 2015. 6

[34] Richa Karmakar, Farha Naaz, Mahesh S. Tirumkudulu, and K. V. Venkatesh. Escherichia coli modulates its motor speed on sensing an attractant. *Arch. Microbiol.*, 198(8):827–833, oct 2016. 6

[35] Richa Karmakar, R. V S Uday Bhaskar, Rajesh E. Jesudasan, Mahesh S. Tirumkudulu, and K. V. Venkatesh. Enhancement of swimming speed leads to

a more-efficient chemotactic response to repellent. *Appl. Environ. Microbiol.*, 82(4):1205–1214, 2016. 6

[36] Mahmut Demir and Hanna Salman. Bacterial thermotaxis by speed modulation. *Biophys. J.*, 103(8):1683–1690, oct 2012. 6, 23

[37] Tomoya Baba, Takeshi Ara, Miki Hasegawa, Yuki Takai, Yoshiko Okumura, Miki Baba, Kirill A Datsenko, Masaru Tomita, Barry L Wanner, and Hirotada Mori. Construction of Escherichia coli K-12 in-frame, single-gene knockout mutants: the Keio collection. *Mol. Syst. Biol.*, 2:2006.0008, feb 2006. 6

[38] Baohu Dai, Jizhuang Wang, Ze Xiong, Xiaojun Zhan, Wei Dai, Chien-Cheng Li, Shien-Ping Feng, and Jinyao Tang. Programmable artificial phototactic microswimmer. *Nat. Nanotechnol.*, (October), 2016. 7

[39] Wei Li, Xiaoran Wu, Hong Qin, Zhongqiang Zhao, and Hewen Liu. Light-Driven and Light-Guided Microswimmers. *Adv. Funct. Mater.*, 26(18):3164–3171, may 2016. 7

[40] Gaszton Vizsnyiczai, Giacomo Frangipane, Claudio Maggi, Filippo Saglimbeni, Silvio Bianchi, and Roberto Di Leonardo. Light controlled 3D micromotors powered by bacteria. *Nat. Commun.*, 8(May):1–7, 2017. 7

[41] Celia Lozano, Borge ten Hagen, Hartmut Löwen, and Clemens Bechinger. Phototaxis of synthetic microswimmers in optical landscapes. *Nat. Commun.*, 12828(7):1–10, 2016. 7

[42] Ayusman Sen, Michael Ibele, Yiying Hong, and Darrell Velegol. Chemo and phototactic nano/microbots. *Faraday Discuss.*, 143(0):15, sep 2009. 7

[43] Michael A. van der Horst, Jason Key, and Klaas J. Hellingwerf. Photosensing in chemotrophic, non-phototrophic bacteria: let there be light sensing too. *Trends Microbiol.*, 15(12):554–562, 2007. 7

[44] Michael A. Van Der Horst and Klaas J Hellingwerf. Photoreceptor Proteins, "Star Actors of Modern Times": A Review of the Functional Dynamics in the Structure of Representative Members of Six Different Photoreceptor Families. *Acc. Chem. Res.*, 37(1):13–20, 2004. 7, 8

[45] Wouter D. Hoff, Michael A. van der Horst, Clara B. Nudel, and Klaas J. Hellingwerf. *Prokaryotic Phototaxis*, volume 571. Humana Press, 2009. 7, 8

[46] A Levskaya, AA Chevalier, JJ Tabor, ZB Simpson, LA Lavery, M Levy, EA Davidson, A Scouras, AD Ellington, EM Marcotte, and CA Voigt. Synthetic biology: engineering Escherichia coli to see light. *Nature*, 438:441, nov 2005. 8

[47] Jesus Fernandez-Rodriguez, Felix Moser, Miryoung Song, and Christopher A Voigt. Engineering RGB color vision into Escherichia coli. *Nat. Chem. Biol.*, AOP(may):1–5, 2017. 8, 35

[48] Stuart Wright, Bharat Walia, John S Parkinson, and Shahid Khan. Differential activation of Escherichia coli chemoreceptors by blue-light stimuli. *J. Bacteriol.*, 188(11):3962–71, jun 2006. 10

[49] Christina Pesavento, Gisela Becker, Nicole Sommerfeldt, Alexandra Possling, Natalia Tschowri, Anika Mehlis, and Regine Hengge. Inverse regulatory coordination of motility and curli-mediated adhesion in Escherichia coli. *Genes Dev.*, 22(17):2434–2446, 2008. 10

[50] H Yang, H Inokuchi, and J Adler. Phototaxis away from blue light by an Escherichia coli mutant accumulating protoporphyrin IX. *Proc. Natl. Acad. Sci. U. S. A.*, 92(16):7332–7336, 1995. 10

[51] H Yang, a Sasarman, H Inokuchi, and J Adler. Non-iron porphyrins cause tumbling to blue light by an Escherichia coli mutant defective in hemG. *Proc. Natl. Acad. Sci. U. S. A.*, 93(6):2459–2463, 1996. 10

[52] T W Grebe and J Stock. Bacterial chemotaxis: the five sensors of a bacterium. *Curr. Biol.*, 8(5):R154–R157, feb 1998. 10

[53] Steven M Block, Jeffrey E Segall, and Howard C Berg. Impulse responses in bacterial chemotaxis. *Cell*, 31(1):215–226, 1982. 10

[54] J E Segall, S M Block, and H C Berg. Temporal comparisons in bacterial chemotaxis. *Proc. Natl. Acad. Sci. U. S. A.*, 83(23):8987–8991, 1986. 10

[55] Yariv Kafri and Rava Azeredo da Silveira. Steady-State Chemotaxis in Escherichia Coli. *Phys. Rev. Lett.*, 100(23):238101, 2008. 10

[56] J S Parkinson. Complementation analysis and deletion mapping of Escherichia coli mutants defective in chemotaxis. *J. Bacteriol.*, 135(1):45–53, jul 1978. 12

[57] Kwang Hwan Jung, Elena N. Spudich, Vishwa D. Trivedi, and John L. Spudich. An archaeal photosignal-transducing module mediates phototaxis in Escherichia coli. *J. Bacteriol.*, 183(21):6365–6371, 2001. 12

[58] John S Parkinson, Peter Ames, and Claudia A Studdert. Collaborative signaling by bacterial chemoreceptors, 2005. 13

[59] Victor Sourjik. Receptor clustering and signal processing in E. coli chemotaxis. *Trends Microbiol.*, 12(12):569–576, 2004. 13

[60] D P Häder. Photosensory behavior in procaryotes. *Microbiol. Rev.*, 51(1):1–21, 1987. 13

[61] Oded Béjà, L. Aravind, V. Koonin, Marcelino T Suzuki, Andrew Hadd, Linh P. Nguyen, Steven B. Jovanovich, Christina M. Gates, Robert A. Feldman, John L. Spudich, Elena N. Spudich, and Edward F. DeLong. Bacterial Rhodopsin: Evidence for a New Type of Phototrophy in the Sea. *Science (80-.).*, 289(5486):1902–1906, 2000. 13

[62] Jed a Fuhrman, Michael S Schwalbach, and Ulrich Stingl. Proteorhodopsins: an array of physiological roles? *Nat. Rev. Microbiol.*, 6(6):488–494, 2008. 13

[63] Robert M. Morris, Michael S. Rappé, Stephanie A. Connon, Kevin L. Vergin, William A. Siebold, Craig A. Carlson, and Stephen J. Giovannoni. SAR11 clade dominates ocean surface bacterioplankton communities. *Nature*, 420(6917):806–810, dec 2002. 13

[64] Oded Béjà, Elena N. Spudich, John L. Spudich, Marion Leclerc, and Edward F. DeLong. Proteorhodopsin phototrophy in the ocean. *Nature*, 411(6839):786–789, 2001. 13

[65] So Young Kim, Stephen A. Waschuk, Leonid S. Brown, and Kwang Hwan Jung. Screening and characterization of proteorhodopsin color-tuning mutations in Escherichia coli with endogenous retinal synthesis. *Biochim. Biophys. Acta - Bioenerg.*, 1777(6):504–513, 2008. 13

[66] Jaoon Yh Kim, Byung Hoon Jo, Younghwa Jo, and Hyung Joon Cha. Improved production of biohydrogen in light-powered Escherichia coli by co-expression of proteorhodopsin and heterologous hydrogenase. *Microb. Cell Fact.*, 11(1):2, 2012. 13

[67] Jessica M Walter, Derek Greenfield, Carlos Bustamante, and Jan Liphardt. Light-powering Escherichia coli with proteorhodopsin. *Proc. Natl. Acad. Sci. U. S. A.*, 104(7):2408–2412, 2007. 13, 14, 15, 18, 21

[68] D C Fung and H C Berg. Powering the flagellar motor of Escherichia coli with an external voltage source, 1995. 13

[69] Christopher V Gabel and Howard C Berg. The speed of the flagellar rotary motor of Escherichia coli varies linearly with protonmotive force. *Proc. Natl. Acad. Sci. U. S. A.*, 100:8748–8751, 2003. 13

[70] Stephen J. Giovannoni, Lisa Bibbs, Jang-Cheon Cho, Martha D. Stapels, Russell Desiderio, Kevin L. Vergin, Michael S. Rappé, Samuel Laney, Lawrence J.

Wilhelm, H. James Tripp, Eric J. Mathur, and Douglas F. Barofsky. Proteorhodopsin in the ubiquitous marine bacterium SAR11. *Nature*, 438(7064):82–85, nov 2005. 13

[71] Ying Wang, Yan Li, Tuan Xu, Zhenyu Shi, and Qiong Wu. Experimental evidence for growth advantage and metabolic shift stimulated by photophosphorylation of proteorhodopsin expressed in Escherichia coli at anaerobic condition. *Biotechnol. Bioeng.*, 112(5):947–956, 2015. 13

[72] P C Maloney. Membrane H+ conductance of Streptococcus lactis. *J. Bacteriol.*, 140(1):197–205, oct 1979. 14

[73] Bart J. Van Rotterdam, Wim Crielaard, Ivo H.M. Van Stokkum, Klaas J Hellingwerf, and Hans V Westerhoff. Simplicity in complexity: The photosynthetic reaction center performs as a simple 0.2 V battery. *FEBS Lett.*, 510(1-2):105–107, jan 2002. 14

[74] C. Douarche, A. Buguin, H. Salman, and A. Libchaber. E. Coli and Oxygen: A motility transition. *Phys. Rev. Lett.*, 102(19):2–5, 2009. 14

[75] Murray J. Tipping, Bradley C. Steel, Nicolas J. Delalez, Richard M. Berry, and Judith P. Armitage. Quantification of flagellar motor stator dynamics through in vivo proton-motive force control. *Mol. Microbiol.*, 87(2):338–347, 2013. 15, 32

[76] D F Blair and H C Berg. Restoration of torque in defective flagellar motors. *Science (80-.).*, 242(4886):1678–1681, dec 1988. 15

[77] A Martinez, A S Bradley, J R Waldbauer, R E Summons, and E F DeLong. Proteorhodopsin photosystem gene expression enables photophosphorylation in a heterologous host. *Proc. Natl. Acad. Sci. U S A*, 104(13):5590–5595, 2007. 18, 22

[78] Claudio Maggi, Alessia Lepore, Jacopo Solari, Alessandro Rizzo, and R Di Leonardo. Motility fractionation of bacteria by centrifugation. *Soft Matter*, 9(45):10885, 2013. 18, 57

[79] Mark J. Schnitzer. Theory of continuum random walks and application to chemotaxis. *Phys. Rev. E*, 48(4):2553–2568, 1993. 19, 23, 62

[80] L. G. Wilson, V. A. Martinez, J. Schwarz-Linek, J. Tailleur, G. Bryant, P. N. Pusey, and W. C K Poon. Differential dynamic microscopy of bacterial motility. *Phys. Rev. Lett.*, 106(1):7–10, 2011. 19, 57, 58, 59

[81] D. T.N. Chen, A. W.C. Lau, L. A. Hough, M. F. Islam, M. Goulian, T. C. Lubensky, and A. G. Yodh. Fluctuations and rheology in active bacterial suspensions. *Phys. Rev. Lett.*, 99(14):148302, oct 2007. 19

[82] Gazalah Sabehi, Alexander Loy, Kwang Hwan Jung, Ranga Partha, John L Spudich, Tal Isaacson, Joseph Hirschberg, Michael Wagner, and Oded Béjà. New insights into metabolic properties of marine bacteria encoding proteorhodopsins. *PLoS Biol.*, 3(8):e273, jul 2005. 22

[83] Vitaly Shevchenko, Thomas Mager, Kirill Kovalev, Vitaly Polovinkin, Alexey Alekseev, Josephine Juettner, Igor Chizhov, Christian Bamann, Charlotte Vavourakis, Rohit Ghai, Ivan Gushchin, Valentin Borshchevskiy, Andrey Rogachev, Igor Melnikov, Alexander Popov, Taras Balandin, Francisco Rodriguez-Valera, Dietmar J Manstein, Georg Bueldt, Ernst Bamberg, and Valentin Gordeliy. Inward H + pump xenorhodopsin: Mechanism and alternative optogenetic approach. *Sci. Adv.*, 3(SEPTEMBER):1–11, 2017. 22

[84] Wander W. Sprenger, Wouter D. Hoff, Judith P. Armitage, and Klass J. Hellingwerf. The Eubacterium Ectothiorhodospira halophila Is Negatively Phototactic, with a Wavelength Dependence That Fits the Absorption-Spectrum of the Photoactive Yellow Protein. *J. Bacteriol.*, 175(10):3096–3104, 1993. 23

[85] Xabel Garcia, Salima Rafa??, and Philippe Peyla. Light control of the flow of phototactic microswimmer suspensions. *Phys. Rev. Lett.*, 110(13):1–5, 2013. 23

[86] Peter Hanggi and Peter Jung. Colored noise in dynamical systems. *Adv. Chem. Phys.*, 89:239–326, 1995. 24

[87] Michael E Cates and Julien Tailleur. Motility-Induced Phase Separation. *Annu. Rev. Condens. Matter Phys.*, 6(1):219–244, 2015. 25

[88] Andrey Sokolov, Igor S. Aranson, John O. Kessler, and Raymond E. Goldstein. Concentration dependence of the collective dynamics of swimming bacteria. *Phys. Rev. Lett.*, 98(15):1–4, 2007. 25

[89] J. Stenhammar, R. Wittkowski, D. Marenduzzo, and M. E. Cates. Light-induced self-assembly of active rectification devices. *Sci. Adv.*, 2(4):e1501850–e1501850, 2016. 25

[90] Martin P. Magiera and Lothar Brendel. Trapping of interacting propelled colloidal particles in inhomogeneous media. *Phys. Rev. E*, 92(1):012304, 2015. 25

[91] Jean-Marie Swiecicki, Olesksii Sliusarenko, and Douglas B Weibel. From swimming to swarming: \emph{Escherichia coli} cell motility in two-dimensions. *Integr. Biol. (Camb).*, 5(12):1490–4, 2013. 25, 60

[92] M. E. Cates. Diffusive transport without detailed balance in motile bacteria: does microbiology need statistical physics? *Rep. Prog. Phys.*, 75(4):042601, apr 2012. 32, 38

[93] Thomas K. Wood, Seok Hoon Hong, and Qun Ma. Engineering biofilm formation and dispersal, feb 2011. 35

[94] Bahareh Behkam and Metin Sitti. Bacterial flagella-based propulsion and on/off motion control of microscale objects. *Appl. Phys. Lett.*, 90(2), 2007. 37

[95] Edward Steager, Chang Beom Kim, Jigarkumar Patel, Socheth Bith, Chandan Naik, Lindsay Reber, and Min Jun Kim. Control of microfabricated structures powered by flagellated bacteria using phototaxis. *Appl. Phys. Lett.*, 90(26), 2007. 37

[96] Edward B Steager, Mahmut Selman Sakar, Dal Hyung Kim, Vijay Kumar, George J Pappas, and Min Jun Kim. Electrokinetic and optical control of bacterial microrobots. *J. Micromechanics Microengineering*, 21(3):035001, 2011. 37

[97] Rika Wright Carlsen, Matthew R. Edwards, Jiang Zhuang, Cecile Pacoret, and Metin Sitti. Magnetic steering control of multi-cellular bio-hybrid microswimmers. *Lab Chip*, 14(19):3850–3859, aug 2014. 37

[98] Morgan M. Stanton, Juliane Simmchen, Xing Ma, Albert Miguel-López, and Samuel Sánchez. Biohybrid Janus Motors Driven by Escherichia coli. *Adv. Mater. Interfaces*, 3(2):1–8, 2016. 37

[99] Yuichi Hiratsuka, Makoto Miyata, Tetsuya Tada, and Taro Q P Uyeda. A microrotary motor powered by bacteria. *Proc. Natl. Acad. Sci.*, 103(37):13618–13623, sep 2006. 37

[100] R Di Leonardo, L Angelani, D Dell'arciprete, G Ruocco, V Iebba, S Schippa, M P Conte, F Mecarini, F De Angelis, and E Di Fabrizio. Bacterial ratchet motors. *Proc. Natl. Acad. Sci. U. S. A.*, 107(21):9541–5, may 2010. 38, 43

[101] Andrey Sokolov, Mario M Apodaca, Bartosz a Grzybowski, and Igor S Aranson. Swimming bacteria power microscopic gears. *Proc. Natl. Acad. Sci. U. S. A.*, 107(3):969–974, 2010. 38, 43, 46

[102] Luca Angelani and Roberto Di Leonardo. Geometrically biased random walks in bacteria-driven micro-shuttles. *New J. Phys.*, 12, 2010. 38

[103] Andreas Kaiser, Anton Peshkov, Andrey Sokolov, Borge Ten Hagen, Hartmut Löwen, and Igor S. Aranson. Transport powered by bacterial turbulence. *Phys. Rev. Lett.*, 112(15):1–5, 2014. 38

[104] P D Frymier, R M Ford, H C Berg, and P T Cummings. Three-dimensional tracking of motile bacteria near a solid planar surface. *Proc. Natl. Acad. Sci. U. S. A.*, 92(June):6195–6199, 1995. 39

[105] Margot A S Vigeant and Roseanne M. Ford. Interactions between motile Escherichia coli and glass in media with various ionic strengths, as observed with a three-dimensional-tracking microscope. *Appl. Environ. Microbiol.*, 63(9):3474–3479, 1997. 39

[106] O. Sipos, K. Nagy, R. Di Leonardo, and P. Galajda. Hydrodynamic Trapping of Swimming Bacteria by Convex Walls. *Phys. Rev. Lett.*, 114(25):1–5, 2015. 39

[107] Herbert Bay, Andreas Ess, Tinne Tuytelaars, and Luc Van Gool. Speeded-Up Robust Features (SURF). *Comput. Vis. Image Underst.*, 110(3):346–359, 2008. 41

[108] S. Bianchi, F. Saglimbeni, A. Lepore, and R. Di Leonardo. Polar features in the flagellar propulsion of E. coli bacteria. *Phys. Rev. E - Stat. Nonlinear, Soft Matter Phys.*, 91(6):1–5, 2015. 41

[109] Santage Kim and Seppo J. Karilla. *Microhydrodynamics : Principles and Selected Applications*. Dover Publications, 1991. 41

[110] Suddhashil Chattopadhyay, Radu Moldovan, Chuck Yeung, and X L Wu. Swimming efficiency of bacterium Escherichia coli. *Proc. Natl. Acad. Sci.*, 103(37):13712–13717, sep 2006. 43

[111] Knut Drescher, Jörn Dunkel, Luis H Cisneros, Sujoy Ganguly, and Raymond E Goldstein. Fluid dynamics and noise in bacterial cell-cell and cell-surface scattering. *Proc. Natl. Acad. Sci. U. S. A.*, 108(27):10940–5, jul 2011. 43

[112] Claudio Maggi, Filippo Saglimbeni, Michele Dipalo, Francesco De Angelis, and Roberto Di Leonardo. Micromotors with asymmetric shape that efficiently convert light into work by thermocapillary effects. *Nat. Commun.*, 6:7855, jul 2015. 44

[113] R. Di Leonardo, A. Búzás, L. Kelemen, G. Vizsnyiczai, L. Oroszi, and P. Ormos. Hydrodynamic synchronization of light driven microrotors. *Phys. Rev. Lett.*, 109(3):034104, jul 2012. 48

[114] Hong Bo Sun and Satoshi Kawata. Two-photon photopolymerization and 3D lithographic microfabrication. *Adv. Polym. Sci.*, 170:169–273, 2004. 51

[115] Shoji Maruo and Satoshi Kawata. Two-Photon-Absorbed Near-Infrared Photopolymerization for Three-Dimensional Microfabrication. *J. Microelectromechanical Syst.*, 7(4):411–415, 1998. 51

[116] Kevin W Eliceiri, Michael R Berthold, Ilya G Goldberg, L Ibanez, B S Manjunath, Maryann E Martone, Robert F Murphy, Hanchuan Peng, Anne L Plant, Badrinath Roysam, N Stuurman, Jason R Swedlow, Pavel Tomancak, Anne E Carpenter, Luis Ibáñez, B S Manjunath, Maryann E Martone, Robert F Murphy, Hanchuan Peng, Anne L Plant, Badrinath Roysam, Nico Stuurmann, Jason R Swedlow, Pavel Tomancak, and Anne E Carpenter. Biological imaging software tools. *Nat Methods*, 9(7):697–710, 2012. 52

[117] Hanchuan Peng. Bioimage informatics: A new area of engineering biology, 2008. 52

[118] Gabriel Rosser, Alexander G. Fletcher, David a. Wilkinson, Jennifer a. de Beyer, Christian a. Yates, Judith P. Armitage, Philip K. Maini, and Ruth E. Baker. Novel Methods for Analysing Bacterial Tracks Reveal Persistence in Rhodobacter sphaeroides. *PLoS Comput. Biol.*, 9(10), 2013. 55

[119] B. Taboada, S. Poggio, L. Camarena, and G. Corkidi. Automatic tracking and analysis system for free-swimming bacteria. *Proc. 25th Annu. Int. Conf. IEEE Eng. Med. Biol. Soc. (IEEE Cat. No.03CH37439)*, 1:906–909, 2003. 54

[120] Gastón Miño, Thomas E Mallouk, Thierry Darnige, Mauricio Hoyos, Jeremi Dauchet, Jocelyn Dunstan, Rodrigo Soto, Yang Wang, Annie Rousselet, and Eric Clement. Enhanced diffusion due to active swimmers at a solid surface. *Phys. Rev. Lett.*, 106(4):1–4, 2011. 57

[121] J. Tailleur and M. E. Cates. Statistical mechanics of interacting run-and-tumble bacteria. *Phys. Rev. Lett.*, 100(21):3–6, 2008. 57

[122] Roberto Cerbino and Veronique Trappe. Differential dynamic microscopy: Probing wave vector dependent dynamics with a microscope. *Phys. Rev. Lett.*, 100(18):1–4, 2008. 57

[123] Michael Prummer, Dorothee Kling, Vanessa Trefzer, Thilo Enderle, Sannah Zoffmann, and Marco Prunotto. A random motility assay based on image correlation spectroscopy. *Biophys. J.*, 104(11):2362–2372, jun 2013. 57

[124] Vincent A. Martinez, Rut Besseling, Ottavio A. Croze, Julien Tailleur, Mathias Reufer, Jana Schwarz-Linek, Laurence G. Wilson, Martin A. Bees, and Wilson C K Poon. Differential dynamic microscopy: A high-throughput method for characterizing the motility of microorganisms. *Biophys. J.*, 103(8):1637–1647, 2012. 57, 58, 59

[125] Luigi Feriani, Maya Juenet, Cedar J. Fowler, Nicolas Bruot, Maurizio Chioccioli, Steven M. Holland, Clare E. Bryant, and Pietro Cicuta. Assessing the Collective Dynamics of Motile Cilia in Cultures of Human Airway Cells by Multiscale DDM. *Biophys. J.*, 113(1):109–119, jul 2017. 57

[126] B.J. Berne and Robert Pecora. Dynamic light scattering: with applications to chemistry, biology, and physics, 2000. 58

[127] Christina Kurzthaler, Sebastian Leitmann, and Thomas Franosch. Intermediate scattering function of an anisotropic active Brownian particle. *Sci. Rep.*, 6(1):36702, 2016. 58

[128] Christina Kurzthaler and Thomas Franosch. Intermediate scattering function of an anisotropic Brownian circle swimmer. *Soft Matter*, 2017. 58

[129] P. N. Pusey and W. van Megen. Detection of small polydispersities by photon correlation spectroscopy. *J. Chem. Phys.*, 80(8):3513, apr 1984. 58

[130] R. Nossal, S. H. Chen, and C. C. Lai. Use of laser scattering for quantitative determinations of bacterial motility. *Opt. Commun.*, 4(1):35–39, sep 1971. 59

[131] H C Berg and L Turner. Chemotaxis of bacteria in glass capillary arrays. Escherichia coli, motility, microchannel plate, and light scattering. *Biophys. J.*, 58(4):919–930, 1990. 60

[132] Eric Lauga, Willow R DiLuzio, George M Whitesides, and Howard a Stone. Swimming in circles: motion of bacteria near solid boundaries. *Biophys. J.*, 90(2):400–412, 2006. 60

[133] Willow R. DiLuzio, Linda Turner, Michael Mayer, Piotr Garstecki, Douglas B Weibel, Howard C Berg, and George M Whitesides. Escherichia coli swim on the right-hand side. *Nature*, 435(7046):1271–1274, 2005. 60

[134] Sherri A. Biondi, John A. Quinn, and Howard Goldfine. Random motility of swimming bacteria in restricted geometries. *AIChE J.*, 44(8):1923–1929, 1998. 61

[135] J. Mannik, Rosalie Driessen, Peter Galajda, Juan E Keymer, and Cees Dekker. Bacterial growth and motility in sub-micron constrictions. *Proc. Natl. Acad. Sci.*, 106(35):14861–14866, sep 2009. 61

[136] S Blanco and R Fournier. An invariance property of diffusive random walks. *Eur. Lett*, 61(2):168–173, 2003. 62

[137] E. A Codling, M. J Plank, and S. Benhamou. Random walk models in biology. *J. R. Soc. Interface*, 5(25):813–834, 2008. 62

[138] J. Adler and B. Templeton. The Effect of Environmental Conditions on the Motility of Escherichia coli. *J. Gen. Microbiol.*, 46:175–184, 1967. 65, 67

[139] K A Datsenko and B L Wanner. One-step inactivation of chromosomal genes in Escherichia coli K-12 using PCR products. *Proc. Natl. Acad. Sci. U. S. A.*, 97(12):6640–5, 2000. 71